

Fall 11-2019

## Large Deformable Soft Actuators Using Dielectric Elastomer and Origami Inspired Structures

JangHo Park  
*Embry-Riddle Aeronautical University*

Follow this and additional works at: <https://commons.erau.edu/edt>



Part of the [Mechanical Engineering Commons](#)

---

### Scholarly Commons Citation

Park, JangHo, "Large Deformable Soft Actuators Using Dielectric Elastomer and Origami Inspired Structures" (2019). *Doctoral Dissertations and Master's Theses*. 498.  
<https://commons.erau.edu/edt/498>

This Dissertation - Open Access is brought to you for free and open access by Scholarly Commons. It has been accepted for inclusion in Doctoral Dissertations and Master's Theses by an authorized administrator of Scholarly Commons. For more information, please contact [commons@erau.edu](mailto:commons@erau.edu).

**LARGE DEFORMABLE SOFT ACTUATORS USING DIELECTRIC  
ELASTOMER AND ORIGAMI INSPIRED STRUCTURES**

**by**

**JangHo Park**

**A Thesis Submitted to the College of Engineering Department of Mechanical  
Engineering in Partial Fulfillment of the Requirements for the Degree of Philosophy  
in Mechanical Engineering**

**Embry-Riddle Aeronautical University  
Dayton Beach, Florida  
November 2019**

**LARGE DEFORMABLE SOFT ACTUATORS USING DIELECTRIC  
ELASTOMERS AND ORIGAMI-INSPIRED STRUCTURES**

by

**JangHo Park**

This thesis was prepared under the direction of the candidate's Thesis Committee Chair, Dr. Eduardo A. Divo, Professor, Daytona Beach Campus, and Co-Chair, Dr. Daewon Kim, Associate Professor, Daytona Beach Campus, and Thesis Committee Members Dr. Jean-Michel Dhainaut, Professor, Daytona Beach Campus, and Dr. Heidi Steinhauer, Professor, Daytona Beach Campus, and Dr. Victor Huayamave, Assistant Professor, Daytona Beach Campus, and has been approved by the Thesis Committee. It was submitted to the Department of Mechanical Engineering in partial fulfillment of the requirements for the degree of Philosophy in Mechanical Engineering.

Thesis Review Committee



**Eduardo Divo, Ph.D.**  
Committee Chair

JEAN MICHEL DHAINAUT

**Jean-Michel Dhainaut, Ph.D.**  
Committee Member



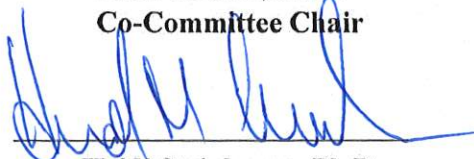
**Victor Huayamave, Ph.D.**  
Committee Member



**Maj Mirmirani, Ph.D.**  
Dean, College of Engineering



**Daewon Kim, Ph.D.**  
Co-Committee Chair



**Heidi Steinhauer, Ph.D.**  
Committee Member



**Eric Coyle, Ph.D.**  
Ph.D. Program Coordinator



**Lon Moeller, J.D.**  
Senior Vice President for Academic  
Affairs and Provost

12/17/19  
Date

## **Acknowledgement**

I would like to express thanks to my advisors, Dr. Eduardo Divo and Dr. Daewon Kim, for their guidance, encouragement, and support throughout my dissertation. I would like to appreciate their expertise in their motivation and encouragement throughout every stage of my dissertation.

I would also like to thank my dissertation committee members, Dr. Jean-Michel Dhainaut, Dr. Heidi Steinhauer, and Dr. Victor Huayamave, for providing me guidance and information to improve my dissertation work.

I would like to thank Dr. Federico Carpi from University of Florence for providing information and guidance related to dissertation and answering questions regarding the subject of dissertation work.

I would like to thank my colleagues, Stanislav Sikulskyi, Ricardo Martinez, and Abdullah El Atrache for research support throughout my dissertation.

I would like to thank my family, especially my wife for helping me go through the entire duration of dissertation.

## **Abstract**

**Researcher: JangHo Park**

**Title: LARGE DEFORMABLE SOFT ACTUATORS USING DIELECTRIC ELASTOMER AND ORIGAMI INSPIRED STRUCTURES**

**Institution: Embry-Riddle Aeronautical University**

**Year: 2019**

There have been significant developments in the field of robotics. Significant development consists of new configurations, control mechanisms, and actuators based upon its applications. Despite significant improvements in modern robotics, the biologically inspired robots has taken the center stage. Inspired by nature, biologically inspired robots are called 'soft robots'. Within these robots lies a secret ingredient: the actuator. Soft robotic development has been driven by the idea of developing actuators that are like human muscle and are known as 'artificial muscle'. Among different materials suitable for the development of artificial muscle, the dielectric elastomer actuator (DEA) is capable of large deformation by applying an electric field. Theoretical formulation for DEA was performed based upon the constitutive hyperelastic models and was validated by using finite element method (FEM) using ABAQUS. For FEM, multi-step analysis was performed to apply pre-stretch to the membrane before applying actuation voltage. Based on the validation of DEA, different configurations of DEA were investigated. Helical dielectric elastomer actuator and origami dielectric elastomer actuator were investigated using theoretical modeling. Comparisons were made with FEM to validate the model. This study focus on the theoretical and FEM analysis of strain within the different configuration of DEA and how the actuation strain of the dielectric elastomer can be translated into contraction and/or bending of the actuator.

## Table of Contents

<b>Acknowledgement</b> .....	<b>3</b>
<b>Abstract</b> .....	<b>4</b>
<b>Table of Contents</b> .....	<b>5</b>
<b>List of Figures</b> .....	<b>7</b>
<b>List of Tables</b> .....	<b>10</b>
<b>Chapter 1. Introduction</b> .....	<b>11</b>
1.1 Inspiration behind Research and Overview .....	11
1.2 Problem Statement and Objective .....	14
<b>Chapter 2. Literature Review</b> .....	<b>17</b>
2.1 Different Types of Muscle and Artificial Muscle .....	17
2.1.1 Mammalian Muscle .....	17
2.1.2 Muscular Hydrostats and Hydrostatic Skeletal System .....	18
2.1.3 Artificial Muscle .....	19
2.2 Types of Soft Actuators.....	21
2.2.1 Pneumatic Actuators (Fluidic Elastomer Actuator).....	21
2.2.2 Hydraulic Actuators.....	22
2.2.3 NiTiNol Artificial Muscle Actuator .....	23
2.2.4 Electro-Active Polymers (EAPs).....	24
2.2.5 Actuator Comparison and Selection .....	25
Table 2.1 Strain of different actuator types [59, 60] .....	25
Table 2.2 Comparison of mammalian muscle to dielectric elastomers [5, 59].....	26
2.2.6 Dielectric Electro-Active Polymer (DEAP) .....	27
2.3 Different Types of Geometrical Structure.....	28
2.3.1 Helical Dielectric Elastomer Actuator .....	28
2.3.2 Spiral Box Pleat Origami Dielectric Elastomer Actuator (DEA) .....	29
<b>Chapter 3. Validation of dielectric elastomers (DE) with ABAQUS</b> .....	<b>31</b>
3.1 Formulation of Maxwell stress.....	31
3.2 Analytical formulation based on assumptions .....	32
3.4 Numerical validation with ABAQUS using neo-Hookean model by applying pre-stretch using multi-step analysis.....	39
3.5 Mesh Refinement .....	43

3.6	Conclusion.....	45
<b>Chapter 4.</b>	<b>Helical Dielectric Elastomer Actuator .....</b>	<b>46</b>
4.1	Introduction - Hyperelastic Material .....	46
4.2	Helical Dielectric Elastomer Actuator (HDEA).....	48
4.3	Numerical Analysis of HDEA .....	49
4.3.1	Research Objective .....	49
4.3.2	Validation Process – Disk Validation and Single Layer.....	49
4.3.3	Results.....	52
4.4	Optimization of Geometrical Parameters of HDEA .....	57
4.4.1	Electromechanical Modeling .....	60
4.4.2	Hyperelastic Material.....	61
4.4.3	Design Envelope .....	66
4.4.4	Optimization Method – Genetic Algorithm.....	66
4.4.5	Results.....	70
4.5	Feasibility to 3D print HDEA and alternative methods .....	72
<b>Chapter 5.</b>	<b>Origami Dielectric Elastomer Actuator .....</b>	<b>74</b>
5.1	Origin of Origami.....	74
5.2	Kresling Pattern Origami Spiral Box Pleat Actuator .....	75
5.2.1	Establishing Geometrical Relationship of Spiral Pleat Box .....	78
5.2.2	Stacked Dielectric Elastomer Actuators for Folding .....	82
5.3	Results .....	86
5.4	Validation of Dielectric Elastomer for Origami Spiral Box Pleat Actuator .....	93
5.4.1	Hyperelastic Modeling.....	93
5.4.2	Ideal Dielectric Elastomer.....	95
5.4.3	Geometrical Modeling of Kresling Pattern.....	100
5.4.4	Analytical Modeling without Fixed End.....	103
5.5	Numerical Analysis of Kresling Pattern.....	104
5.6	Results .....	115
<b>Chapter 6.</b>	<b>Conclusion and Future Work .....</b>	<b>118</b>
<b>Chapter 7.</b>	<b>References.....</b>	<b>120</b>

## List of Figures

Figure 1.1 Movement of earthworm represents how soft actuators work. [62].....	11
Figure 1.2. MER bot from MIT. Electro-Active Polymers was used as a method for actuation. [6] .....	14
Figure 2.1 Skeletal mammalian muscle and muscle fiber. [61].....	17
Figure 2.2 Hydrostatic muscle of an earthworm. [62] .....	18
Figure 2.3 Different types of artificial muscles are being developed using different methods and materials. [10, 63, 64, 65] .....	19
Figure 2.4 Fluidic actuator utilizes different chambers for actuation. [22] .....	21
Figure 2.5 Conventional hydraulic actuator. [67].....	22
Figure 2.6 NiTiNol wire used for actuation of a model hand. [66] .....	23
Figure 2.7 Hexapod made from Electro-Active Polymers (EAPs). [6] .....	24
Figure 2.8 (a) Method Dielectric Elastomer Actuator (DEA) operates. (b) Area increases as thickness reduces. [25] .....	27
Figure 2.9 (a) Stacked DEA and (b) Configuration of Helical Dielectric Elastomer (HDEA). [25] .....	28
Figure 2.10 Spiral Box Pleat made using Kresling pattern. [52].....	29
Figure 3.1 (a) Initial state, (b) pre-stretch state, and (c) actuated state of elastomer membrane with dimension notations. The picture is an exaggerated form to aid description.....	36
Figure 3.2 (a) Boundary conditions for numerical analysis for pre-stretch with multi-step and (b) boundary condition for numerical analysis involving Maxwell stress with multi-step. ....	40
Figure 3.3 Pre-stretch state of numerical analysis .....	41
Figure 3.4 Actuated state of numerical analysis .....	42
Figure 3.5 Voltage vs. strain relationship for neo-Hookean element unit based upon analytical solution. The values were validated using numerical analysis using ABAQUS. ....	43
Figure 3.6 Mesh refinement comparison between mesh size (a) 0.05 and (b) 0.1 for stress .....	44
Figure 4.1 (a) Configuration of Disk Dielectric Elastomer based upon Kovac et al. (b) Numerical validation was performed to validate FEA modeling method. [4, 9].....	50
Figure 4.2 (a) Voltage vs. contraction strain (%) and (b) voltage vs. deformation data acquired from Kovacs’s paper. ....	51
Figure 4.3 (a) Voltage vs. contraction strain (%) and (b) voltage vs. deformation validation data from ABAQUS DDEA Model. ....	51
Figure 4.4 Axial deformation for single layer HDEA. ....	53
Figure 4.5 Comparison of analytical <sup>13</sup> and numerical solution.....	53
Figure 4.6 (a) Configuration of 2 layers of HDEA and (b) 10 layers of HDEA and the geometrical dimensions. ....	54
Figure 4.7 (a) Voltage vs. height and (b) voltage vs. contraction strain (%) deformation of 10 layers HDEA.....	55



Figure 4.8 Electrode placement and geometrical parameters of HDEA. The bending of HDEA was measured. ....	56
Figure 4.9 Voltage vs. contraction and voltage vs. bending angle for 2 layers of HDEA. ....	57
Figure 4.10 (a) Explanation of lead angle to explain the pitch angle used in helical structures and (b) other parameters that are involved in helicoid geometric calculation using parametric equations. ....	58
Figure 4.11 (a) Orientation of x, y, z direction shown as 1, 2, 3 and the (b) corresponding Cauchy stress. ....	62
Figure 4.12 The Pareto Front for the multi-objective function. Objective 1 is voltage while objective 2 is the inverse of strain. ....	70
Figure 4.13 Optimized HDEA before (a) and after (b) actuation. The bottom electrode was fixed and the pressure was applied on the electrode section based on the positive and negative charge direction to implement compression of the elastomer layers. ....	72
Figure 5.1 (a) Crease pattern of spiral box pleat, (b) fully folded configuration, (c) fully deployed configuration. ....	77
Figure 5.2 (a) Strain displacement graph, (b) angle displacement graph, and (c) force displacement graph ....	81
Figure 5.3 Structure of the stacked folding DEA along the folding region. (a) PETG thick and thin layer are used as inactive layer to maximize the folding motion and (b) voltage is applied and folding happens in the thin inactive layer regions. ....	84
Figure 5.4 Single cell Kresling pattern model in (a) non-deformed and (b) deformed states. ....	85
Figure 5.5 Actuation force profiles of the single cell Kresling pattern. ....	86
Figure 5.6 Stacked dielectric elastomer hinge (a) before deformation (0 kV) and (b) after deformation (4 kV); Isometric view of deformation along the length of the stacked DEA hinge. ....	87
Figure 5.7 Angle $\gamma$ based on (a) before actuation and (b) after actuation voltage has been applied. ....	88
Figure 5.8 (a) The elastomer hinge and the (b) direction of DEAs expansion along the hinge with (c) block force. ....	90
Figure 5.9 (a) Deformation of height, (b) change in angle, and (c) block force of the stack dielectric elastomer on the Kresling spiral box pleat. ....	91
Figure 5.10 Deformation of the dielectric elastomer hinge with actuation voltage of (a) $V = 0$ kV, (b) $V = 2$ kV, (c) $V = 4$ kV. ....	92
Figure 5.11 (a) Initial state of dielectric elastomer before actuation and (b, c) after actuation with deformed dimension. (b) is when $W$ is constrained and (c) is when $H$ is constrained. ....	96
Figure 5.12 Theoretical curves when no pre-stretch was applied. ....	100
Figure 5.13 (a) FEA model of spiral box pleat and (b) folded model of spiral box pleat using paper. The FEA model show thickness and smooth folding whereas the paper fold neglect to thickness and the smooth fold due to the thickness of paper being negligible. A single cell of the spiral box pleat was evaluated for the numerical analysis below for single layer as well as three combined layers. [27] ....	101

Figure 5.14 Geometry of smooth fold and the four points that determines the boundary of the smooth fold for Kresling pattern. ....	102
Figure 5.15 (a) Theoretical curves for $\lambda_1 = 2.125$ are represented in both plot along with the data points acquired from numerical analysis. The circular, square and diamond dots represent the numerical results without the stiffener. (b) Numerical results with the stiffener were obtained and are demonstrated as circular, square and diamond dots. Theoretical curves without the stiffener were plotted for reference. ....	105
Figure 5.16 (a) Theoretical curves for $\lambda_1 = 2.75$ are represented in solid lines. The circular, square and diamond dots represent the numerical results without the stiffener. (b) Numerical results with the stiffener were obtained and are demonstrated as circular, square and diamond dots. Theoretical curves without the stiffener were plotted for reference. ....	107
Figure 5.17 (a) Theoretical curves for $\lambda_1 = 3.5$ are represented in solid lines. The circular, square and diamond dots represent the numerical results without the stiffener. (b) Numerical results with the stiffener were obtained and are demonstrated as circular, square and diamond dots. Theoretical curves without the stiffener were plotted for reference. ....	109
Figure 5.18 (a) FEA result without stiffeners when subjected to 12 kV along the thickness direction and the planar direction for stretch ratio along the vertical direction. (b) Approximately 10% strain was obtained. ....	110
Figure 5.19 $\lambda_1 = 2.125$ Deformation vs. Voltage without stiffener. ....	111
Figure 5.20 $\lambda_1 = 2.75$ Deformation vs. Voltage without stiffener. The legend can be seen in Figure 5.19. ....	111
Figure 5.21 $\lambda_1 = 2.125$ Deformation vs. Voltage with stiffener. The legend can be seen in Figure 5.19. ....	112
Figure 5.22 $\lambda_1 = 2.75$ Deformation vs. Voltage with stiffener. The legend can be seen in Figure 5.19. ....	113
Figure 5.23 $\lambda_1 = 3.5$ Deformation vs. Voltage without stiffener. The legend can be seen in Figure 5.19. ....	113
Figure 5.24 $\lambda_1 = 3.5$ Deformation vs. Voltage with stiffener. The legend can be seen in Figure 5.19. ....	114
Figure 5.25 (a) Location of the 4 points of stiffener based on the analytical solution of geometrical modeling of the stiffeners for the smooth folding surface. (b) The stiffener required more voltage for actuation however, the bending of the DEA occurred along the stiffeners. ....	115
Figure 5.26 (a) The bending angle of the origami DEA. The neutral axis is pointed by the extruded line. The bending angles were measured based on change in each element. ....	116
Figure 5.27 Bending angle vs. voltage vs. tip displacement. The higher voltage, the more bending was observed. ....	116

## List of Tables

Table 2.1 Strain of different actuator types [59, 60].....	25
Table 2.2 Comparison of mammalian muscle to dielectric elastomers [5, 59].....	26
Table 4.1 Design Envelope .....	66
Table 4.2 Optimal combination of parameters in HDEA. ....	71
Table 5.1 Parameters for static analysis.....	81
Table 5.2 DEA material parameters for VHB 4910 (Neo-Hookean) .....	88
Table 5.3 Deformation, angle and block force to the corresponding voltage.....	90
Table 5.4 Hyperelastic model equations for the 4 different models .....	97
Table 5.5 Material properties and geometrical parameters used for modeling.....	99

## Chapter 1. Introduction

### 1.1 Inspiration behind Research and Overview

Robotics has grown exponentially over the past couple of decades. Despite the advance in robotics, the majority of the theories and techniques for control and fabrication are based on the conventional definition of robots: kinematic chain of rigid underlying structures that can perform specialized tasks [1, 2, 3, 7]. These robots often encounter limitations to interacting with the environment and operate under unstructured and refined environments. Evolution of biological life has done a great job at making things perfectly equipped and interactive with our world. And now, robotics is starting to follow suit in the emerging field called soft robotics.

People have been referring back to nature for inspirations as well as for solutions to problems. Biological evolution has occurred over millions of years. When you look at animals, which are debatably the best examples we have for adapting to new environments, they are pretty much all soft. Humans ourselves are mainly fluid. This concept is called

biomimetic or biomimicry. Muscular hydrostats are a biological structure found in animals such as octopus tentacles or the trunk of elephant. This particular muscle group consists mainly of muscles with no skeletal support. A muscular hydrostat is composed mainly of muscle tissue, which itself is mainly made of water that makes it

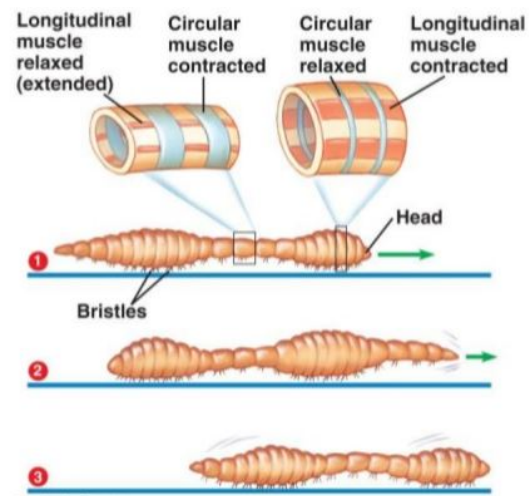


Figure 1.1 Movement of earthworm represents how soft actuators work. [62]

incompressible like the hydrostatic skeletons. Hydrostatic skeleton is also a biological structure that is common among primitive invertebrate organisms such as the earthworm and hydra. Unlike muscular hydrostats, which are covered by muscle groups, hydrostatic skeleton is a flexible skeleton supported by the pressure from fluid-filled cavity.

However, both share the same muscular anatomy of antagonist muscle where one group relaxes and elongates, while the other group generates force by contracting. Force transmission in muscular hydrostat is generated by exploiting the near incompressibility of muscle at physiological pressure and arranging the muscle structure [4,5]. Force transmission in hydro skeleton is provided by the pressure in the enclosed fluid. The principle behind motion of hydro skeleton can be shown in Figure 1.1. The muscle fibers are oriented in three different directions: parallel to the long axis, perpendicular to the long axis and wrapped around the long axis. Muscle fibers that are parallel to the long axis are arranged in longitudinal bundles where the muscle fibers that are perpendicular to the long axis are arranged in the radial or transverse pattern. Muscle fibers that are wrapped along the long axis are usually helical or oblique and wrap around the center core.

The most important biomechanical principle that allows the muscle groups to elongate, bend and twist is based on incompressibility [1, 2, 4, 5]. Having a constant volume, decrement in one dimension will cause a compensatory increment in the other dimension which allows constancy in volume to enable shape changes due to the absence of skeletal structures. Based on incompressibility, a cylindrical muscular hydrostat can experience 80% elongation while the diameter of the cylinder decreases by 20%.

Elongation in muscular hydrostats and hydro skeletons occurs by the contraction of transverse or helical muscular arrangements. Bending occurs under unilateral contraction and contraction of transverse or radial muscles based on the antagonistic behavior. Twisting, also known as torsion, can occur under helical muscular structures creating moments based on the muscle fiber angle. When the following movements are performed, the stiffness of the muscular structure rises, which allows the muscle to bear loads.

The wall structure of invertebrates with hydro skeletons is reinforced with connective tissue fibers in continuous parallel sheets of fiber that wrap the animal in helical arrays with opposite chirality. Such cross-fiber helical connective tissue arrays are capable of providing reinforcement to the wall and allow contraction, bending and twisting motions.

Based on muscular hydrostats and its principles, researchers are inspired by nature to develop soft actuators to implement on soft robotics. Recent advances in smart and soft materials have permitted large interests in soft robotics. Soft robots have become more popular worldwide due to redundant degrees of freedom, operation under refined spaces and capability to perform delicate tasks. This represents new solutions, applications and paradigms that can overcome the definition of conventional robots and open new perspectives to modern robotics. Different types of actuators based on soft materials are being implemented on the state of the art in soft robotics. Materials with favorable properties are studied to mimic the muscle of living organism in order to build actuators that are capable of performing muscle movements. In this study, soft actuators are

investigated in the literature review and a specific group of soft actuator was selected to mimic the characteristics of the muscle [3, 4, 5].

## 1.2 Problem Statement and Objective

Biologically-inspired design has taken the center stage in the development of innovative solutions in various fields of engineering and science. For instance, in robotic engineering, the limited degrees of freedom and bulkiness of traditional “hard robots” impose obstacles in advancing the technology while bio-inspired “soft robots” can provide numerous advantages, such as high flexibility and theoretically infinite degrees of freedom. Soft robots are capable of performing sophisticated tasks that traditional robots with hard rigid bodies find troublesome. Soft robots are capable of handling delicate objects, able to reach objects that rigid robots cannot, and mimic the behavior of human muscles and behave as ideal actuator [1, 4, 5, 6].

Different types of soft actuators are studied based upon its advantages and disadvantages. Among different groups of soft actuators, Electro-Active Polymers



(EAPs) display favorable characteristics including low weight, high fracture tolerance, pliability, reversibility and large strain for a soft actuator. The EAPs can be classified into electronic EAPs and ionic EAPs. The ionic EAPs require constant hydration and produce low stress which makes it

Figure 1.2. MER bot from MIT. Electro-Active Polymers was used as a method for actuation. [6]

less favorable compared to electronic EAPs, which provide large strains, rapid response, and relatively high efficiency with a downfall of high voltage requirement for actuation. Literature studies concluded that the characteristics of dielectric elastomer actuators are the closest to animal muscles based on criteria of strain, actuation pressure, density, efficiency and response time. This will be further discussed in the literature studies.

There have been many applications using dielectric elastomer actuator (DEA) technology to develop soft actuators and soft robots such as the MER-bots and earthworms for locomotion [2, 3, 4, 6].

Despite the fact ionic actuators are not as favorable as electronic actuators, some actuators were developed using conducting polymers. Ionic conducting polymer film was put to use for developing underwater turtle/frog robots and fish robots [2, 3, 6]. By using low voltage and being surrounded by fluid to its advantage, the micro-muscle actuation device was developed based on conjugated polymers to actuate underwater robots.

Ionic polymers are another group of popular materials used in soft robotic actuators. The most widely used actuators are ionic polymer metal composites (IPMC) actuators as they are susceptible to dehydration and degrading. However, controlling IPMC remains a challenge due to the lack of understanding of materials [2].

Several limitations that the EAPs inherit make their extensive use in robotic actuators difficult. While most ionic EAPs can work only in aqueous media, conjugated polymers and ionic polymer metal composites have short life cycles.

Electronic EAPs' capability to mimic human muscle has led to the emerging interest in the development of artificial muscle. Electronic EAPs are polymers that change shape and size when stimulated by electric field. Among electronic EAPs,



dielectric elastomer actuator (DEA) is one of the most advantageous EAPs and has been widely used for application areas including grippers, robotics, pumps, and artificial muscles. Due to the capability of large strain, fast response time, and high elastic energy density, DEA was investigated throughout this research. As mentioned above, for robotic applications, there are various types of actuators being created for different types of applications [1, 5, 7]. All actuators have their unique advantages of large strain, fast response, high energy density, and force output but there is no perfect actuator without its own limitations. As a result, they compromise certain functions to maximize other advantages. Therefore, there is a need for smart material actuators which can perform all the functions of generic actuator and aid in many other capabilities by combining advantages of different actuators.

As a result, the objective of this research is to develop a soft actuator that is pliable, lightweight, and capable of large strain that functions like an artificial muscle. The actuator needs to perform in the same manner as a generic actuator while it is capable of large strain and increase in strength to withstand weight. In order to determine the material properties, as well as geometrical properties where large strain and strength can coexist, optimization of the geometrical parameters of smart materials was conducted to mitigate the disadvantages while increasing its performance of the actuator. In addition, unique geometry and novel structures were investigated to maximize the strain while increasing its strength to bear loads.

## Chapter 2. Literature Review

### 2.1 Different Types of Muscle and Artificial Muscle

#### 2.1.1 Mammalian Muscle

Mammalian muscle is a group of heterogeneous tissue composed with different groups and sizes of fibers. These groups of fibers provide versatility and function as antagonistic

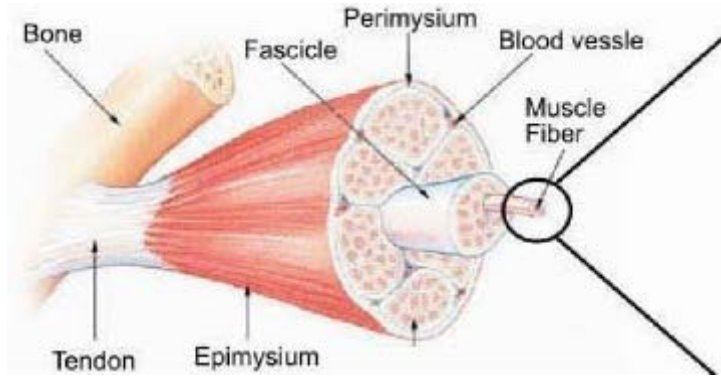


Figure 2.1 Skeletal mammalian muscle and muscle fiber. [61]

muscle group. Antagonistic muscle group are made from flexors and extensors where the muscle contracts in one end and extends in the other to create a bending movement of a human arm [59].

The muscle groups are formed around the skeletal structure aiding its shape and providing support and strength to withstand loads or exert a large amount of force. The skeletal structure supports the muscle structures while the muscle fibers work together providing synergy to a certain movement performed. Mammalian muscle fibers are made in a long cylindrical shape which are bundled together. The mammalian muscle have a large advantage of providing strength and bearing loads, but have limited degrees of freedom. Numerous actuators have been derived from mimicking the characteristics of mammalian muscle due to its capability of being implemented to skeletal structures.

### 2.1.2 Muscular Hydrostats and Hydrostatic Skeletal System

The fundamental principle of this actuator comes from biomimicry of muscular hydrostat and hydrostatic skeleton. Muscular hydrostats are a biological structure that is found in animals. This particular muscle group consists of muscles with no skeletal support. The hydrostatic skeleton is also a biological structure that is common among primitive invertebrate organisms. The difference between muscular hydrostats and hydrostatic skeletons is that hydrostatic skeletons are flexible skeletons surrounded by chambers of fluid whereas muscular hydrostats are composed of muscle tissues that are filled with water which makes it incompressible.

However, both share the same muscle anatomy of antagonist muscle where one group of muscle relaxes while the other group of muscle contracts. The hydrostatic skeleton transmits force by the pressure that is enclosed within the

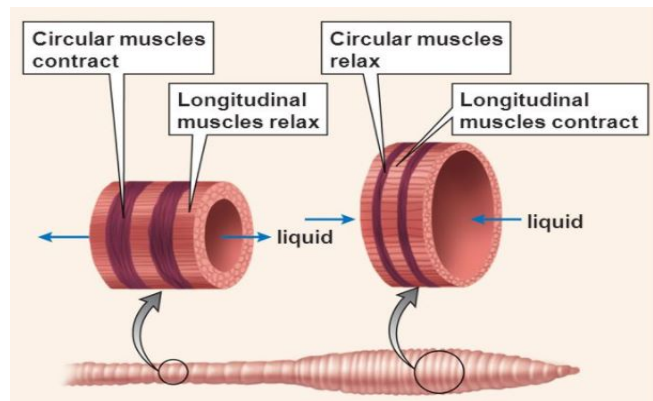


Figure 2.2 Hydrostatic muscle of an earthworm. [62]

fluid whereas, muscular hydrostat transmits the force generated by the near incompressibility of muscle tissue at physiological pressure and thus arranging muscle structure. The important biomechanical principle behind this mechanism is incompressibility. Having constant volume, a decrease in one dimension will cause a compensatory increase in the other dimension which allows constancy in volume, to enabling shape changes due to the absence of skeletal structures [43, 50, 59].

The idea of this actuator can be well represented by cephalopod, also known as a squid or octopus. Support and movement in cephalopod depends on a form of hydrostatic skeletal support, referred to as a muscular hydrostat, in which the musculature serves both for force generation and as the support for movements. Because the muscle and other tissues of the arms and tentacles resist volume change, any decrease in one dimension must result in an increase to another. Since muscle fibers are oriented in three different dimensions, active control of all dimensions can be achieved. This allows for a great diversity and complexity of movements, including elongation, shortening, bending and stiffening based on torsion. However, due to lack of skeletal support, the hydrostatic muscle cannot exert and withstand large loads compared to mammalian muscle.

### 2.1.3 Artificial Muscle

Artificial muscle development started with the idea of combining the benefits of the mammalian muscle and hydrostatic muscle. Artificial muscles are actuators that

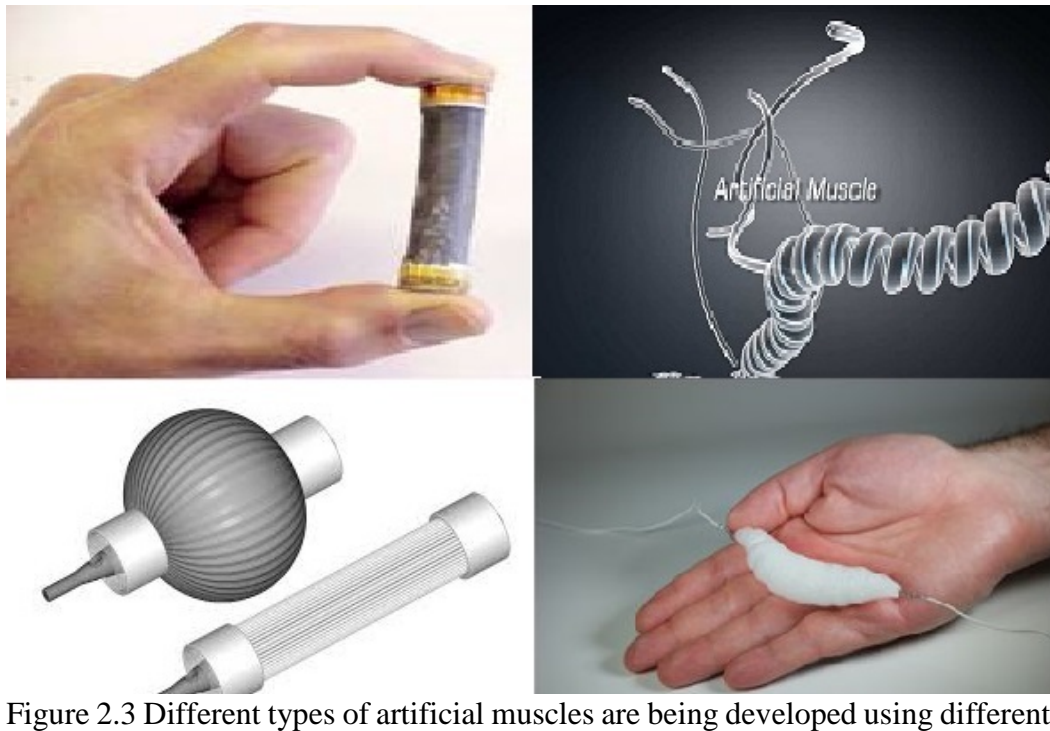


Figure 2.3 Different types of artificial muscles are being developed using different methods and materials. [10, 63, 64, 65]

mimic natural muscles and can perform three basic actuations; contract, expand, and rotate with the capacity to reverse when an external stimulus is applied.

While developing artificial muscles, there are certain key criteria that need to be met based on the applications of the artificial muscle. The criteria includes stress, strain, life cycle, elastic modulus, response speed, energy density, force, and efficiency [1, 3, 7, 47, 59].

There are various means of actuation based on the criteria mentioned above. There are electric field, pneumatic, thermal, hydraulic and light responsive actuators that are suitable based on different applications. As a result, different materials are utilized based upon its application as well.

Shape memory alloys and polymers and meta-materials are widely used materials that are being investigated as a candidates for artificial muscle. These materials are used to make soft actuators based on different actuation methods.

Soft actuators fall under the category of artificial muscle and in their own ways, have their advantages and disadvantages. While pneumatic actuators are inherently compliant, have a high force to bear loads, decent strain, they require fluid or air to perform actuation by distributing the fluid in different chambers. This requires a chamber for fluids and, as it requires more than one component to perform actuation, it makes the fluid/pneumatic actuators not qualify for the category of artificial muscle.

Shape memory alloys and polymers react based upon heating and cooling thus the response speed is slow. It is only compliant in certain phases and has low force and low strain which is not a desirable actuator for artificial muscles that require high force and large strain.

There is also a group of actuators that falls under the family of Electro-Active Polymers (EAPs). The EAPs have ionic and electronic EAPs. Among the group of electronic EAPs, dielectric elastomer shows favorable characteristics. It is compliant, can be stiffened, lightweight, and has large strain with a very fast response. Different types of soft actuators and developments are discussed below [1, 2, 18, 59, 60].

## 2.2 Types of Soft Actuators

### 2.2.1 Pneumatic Actuators (Fluidic Elastomer Actuator)

Pneumatic actuators consist a thin, flexible tubular membrane that is braided and netted by fiber reinforcements. Pneumatic systems are designed like those of a hydrostatic skeleton which is filled with air or pressurized gas. The primary source of

pneumatic actuator is air, therefore it is cost effective and easy to replenish the source. It is also relatively safe, easy to operate, and maintain.

The maximum contraction strain of pneumatic actuators is approximately 57% while

average pneumatic actuators have elongation strain. Upon operation, pneumatic actuators can display a significant amount of block force due to the braided fibers that are present

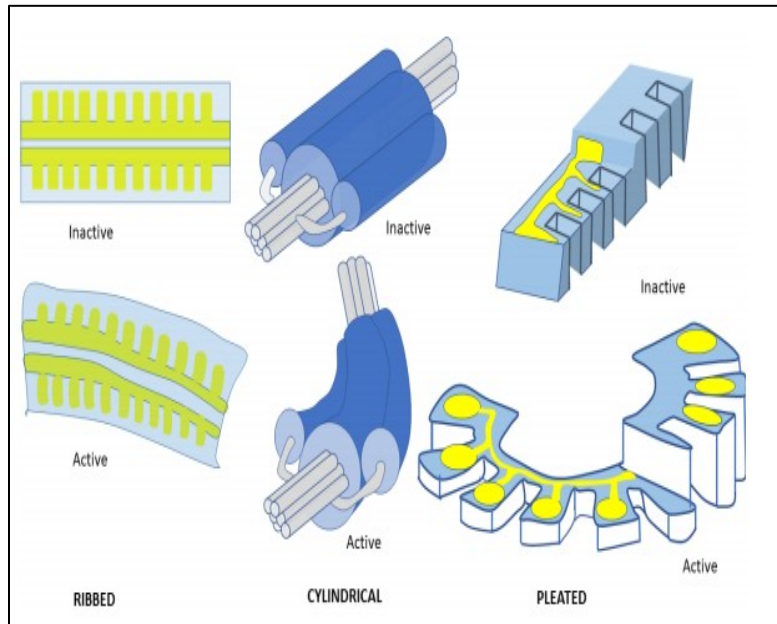


Figure 2.4 Fluidic actuator utilizes different chambers for actuation. [22]

for reinforcements. However, the pneumatic actuators have several limitations for the robotics and the actuator industry. They are prone to buckling under compressional axial loading. Controlling the system and speed to the desired result remains a challenge while bulky air compressors are required for continuous operations restricting the mobility and making miniaturization more difficult. The advantage over EAPs is that pneumatic actuators are chemically more stable and easier to work with. In order to overcome its disadvantages, the scaling down of pneumatics actuator is currently under progress while other methods such as origami and different fiber reinforcements are being developed to enhance the performance of the pneumatic actuators. There have been numerous applications based on pneumatic actuators mimicking the movements of the animals that have hydrostatic skeletons such as elephant trunks, Oct-Arm, tentacle-structured robots, and pneumatic air muscles.

### 2.2.2 Hydraulic Actuators

Similar to pneumatic actuators, hydraulic actuators are used for high force applications. They can produce forces greater than pneumatic actuators of equal size and can operate in a higher pressure range. However, similar to that of pneumatic actuators requiring a constant source of pressurized gas,

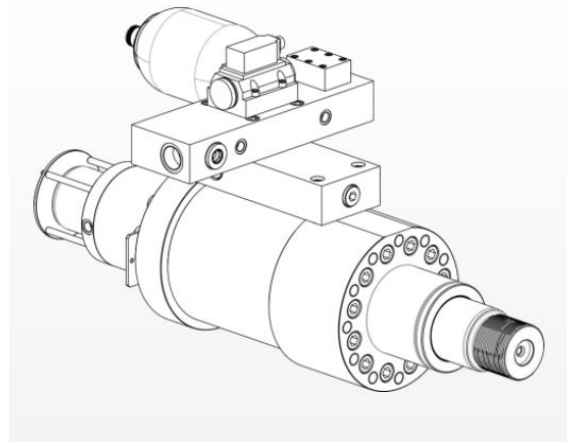


Figure 2.5 Conventional hydraulic actuator. [67]

hydraulic actuators require a constant source of fluid. This requires additional parts such

as a fluid reservoir, pumps, release valves, and noise reduction equipment which is bulky and requires structural space. Hydraulic and pneumatic actuators are used in similar applications where hydraulics are preferred when high force is needed.

### 2.2.3 NiTiinol Artificial Muscle Actuator

Nickel Titanium shape memory alloy is one of soft actuators that has a unique martensite transformation that makes it inherently flexible with high energy density.

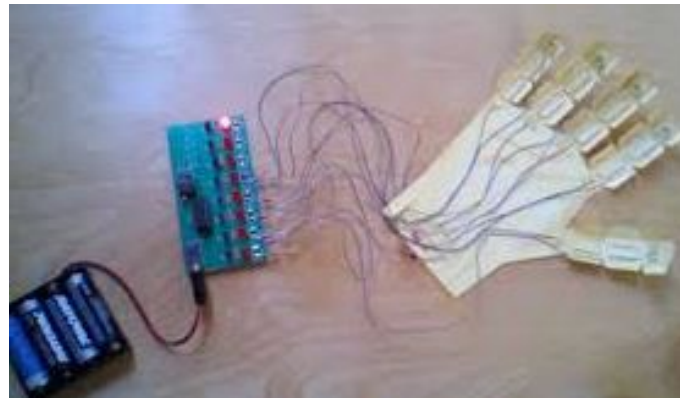


Figure 2.6 NiTiinol wire used for actuation of a model hand. [66]

By constructing the NiTi wire in a coil spring structure, large strokes are available despite the small lattice structure. NiTi coil springs are created from straight wire wound into a coil shape and annealed at a high temperature to reset the memorized shape. The actuation speed of the NiTi wires depends on the electric current to heat the memorized coil and change its shape. The NiTi coil exhibits similar disadvantages as other soft actuators. Since NiTi springs are unipolar actuators for repeatable motion, in order to perform as an antagonist actuator, it requires a second coil. In addition, unlike other soft actuators where energy is stored elastically in the off-state, NiTi requires work to be done to return to the martensite state.



#### 2.2.4 Electro-Active Polymers (EAPs)

Electro-Active Polymers (EAPs) are often compared with electro-active ceramics, shape memory alloys, and other soft actuators. Comparisons are drawn since EAPs potentially have similar applications.

EAPs display favorable characteristics including low weight, high fracture tolerance, pliability, reversibility and large strain for a soft actuator. The EAPs can be classified into electronic EAPs and ionic EAPs. The ionic EAPs require constant hydration and produce low stress. This makes ionic EAPs less favorable compared to electronic EAPs which provide large strains, rapid response, and relatively high efficiency with a downfall of a higher voltage requirement for actuation [1, 2, 5, 7, 47, 59].

In most cases, ionic actuators aren't as favorable as electronic actuators. However, some actuators were developed using conducting polymers. By using ionic conducting polymer film, underwater turtle/frog robots and fish robots have been developed. The using of low voltage and the surrounding fluid to its advantage, micro-muscle actuation devices were developed. Ionic gels, polymers, metal composites, conductive rubbers and carbon nanotubes are examples of ionic EAPs.



Figure 2.7 Hexapod made from Electro-Active Polymers (EAPs). [6]

As mentioned above, EAPs can outperform existing technologies such as shape memory alloy (SMA), pneumatic actuators, and electro-active ceramics. The most attractive characteristic of EAPs is their ability to emulate the operation of biological muscle in high fracture toughness and in large actuation strain.

The electronic EAPs, unlike the ionic EAPs, requires large actuation voltage. Among the family of EAPs, dielectric elastomer actuator (DEA) shows promising properties as well as identical properties of human muscle.

### 2.2.5 Actuator Comparison and Selection

Despite the listed actuators above, there are other types of actuators used for developing artificial muscle. They all have unique material properties and provide different benefits. Discussed in the objectives, one of the properties that is considered for actuator development is large strains. The below table shows a comparison of the strain of different actuators.

Table 2.1 Strain of different actuator types [59, 60]

Actuator Type	Max Strain (%)
Shape Memory Alloy	8
Dielectric Elastomer (acrylic)	500
Dielectric Elastomer (silicone)	63
Ferroelectric Polymer	7
Piezoelectric (PZT)	0.2
Brushless Motor	0~1000

As seen, acrylic dielectric elastomer shows an exceedingly high number as a soft actuator where a traditional brushless motor can vary its strain depending on the structure. This makes acrylic DEA a favorable material for artificial muscle development. Therefore, a direct comparison of acrylic dielectric elastomer to human muscle was made.

Table 2.2 Comparison of mammalian muscle to dielectric elastomers [5, 59]

Property	Mammalian Muscle	Dielectric Elastomers
Strain (%)	20-40	10-100
Stress (MPa)	0.1-0.35	0.1-2
Work Density ( $\text{kJ}/\text{m}^3$ )	8-40	10-150
Density ( $\text{kg}/\text{m}^3$ )	1037	<1000
Continuous Power (W/kg)	50-280	<500
Voltage (V)	<1	>1000
Modulus (MPa)	10-60	0.1-3

The table demonstrates that dielectric elastomer exhibits better material properties in the majority of areas when compared to a mammalian muscle. This shows a clear indication that dielectric elastomer has the potential to be a suitable material for artificial muscle development.

## 2.2.6 Dielectric Electro-Active Polymer (DEAP)

Dielectric Electro-Active Polymer (DEAP) is one of the most advantageous electronic EAPs and has been widely used for the development of smart actuators. Application areas include grippers, robotics, pumps, vehicles (land, aerial and marine), as well as artificial muscles. DEAP can work and operate in different types of systems and have the ability to actively or passively deform due

to large strain capabilities. Depending on the material and the manufacturing techniques used, DEAP can be implemented for various applications to obtain the desired strains.

DEAP consists of an elastomer sandwiched between two thin layers of electrodes, which are connected to positive and negative terminals from a high voltage source, typically by the means of wires. When an electric field is applied to DEAP, electrical charges form dipoles and align the electrical charges in the direction of electric field. This creates internal stress in the structure called Maxwell stress, which results in the reduction of thickness along the direction of the applied electric field and elongation in the perpendicular direction [1, 2, 3, 5, 7, 9].

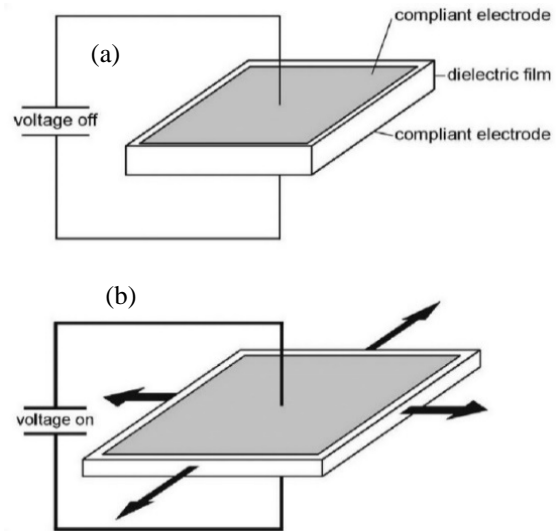


Figure 2.8 (a) Method Dielectric Elastomer Actuator (DEA) operates. (b) Area increases as thickness reduces. [25]

## 2.3 Different Types of Geometrical Structure

### 2.3.1 Helical Dielectric Elastomer Actuator

Helical DEA (HDEA) is one type of electronic EAPs first proposed by Carpi *et al.* [10, 12, 14] in 2005. An HDEA with its unique configuration does not only provide the contractile and extendable capabilities, but can aid in attaining results for bending and torsion.

HDEA can also produce larger strains and improve efficiency for the actuator performance. There is a need of new efficient technologies, which can improve performance by making HDEA less complicated and more reliable.

Hence, while applying the voltage across this structure, HDEA would not only contract axially or expand radially, but also can be partly squeezed enabling bending within the structure, as it is less rigid comparatively. The actuation voltage and the thickness of the electrode and elastomeric layers determine the strain that the specimen is going to produce. The attributes of the material used to build the structure play a vital role in the behavior [10, 13, 25, 50].

The continuity of the geometry was taken into consideration when HDEA came across a new geometry called spiral pleat. Spiral pleat is a method used in origami to fold helical structures. As a result, more studies on geometrical structures were conducted to enhance the criteria listed for the artificial muscle system [5, 7].

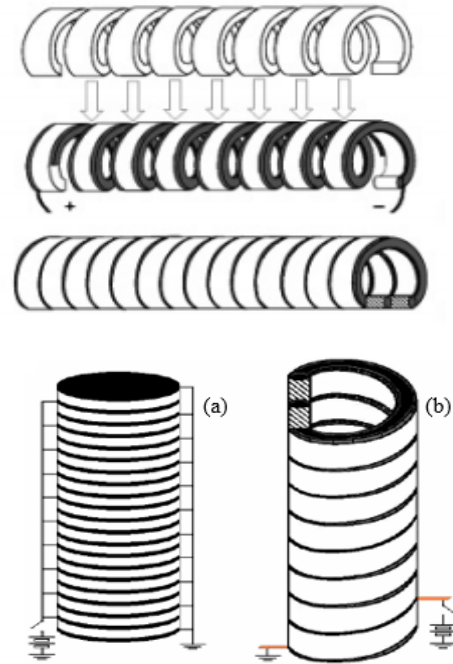


Figure 2.9 (a) Stacked DEA and (b) Configuration of Helical Dielectric Elastomer (HDEA). [25]

### 2.3.2 Spiral Box Pleat Origami Dielectric Elastomer Actuator (DEA)

Folding sheet materials into cylindrical structures using an origami-based approach allows the sheet materials to be densely packed within a confined space and to be deployed when needed. Kresling pattern, which is a cylindrical origami pattern consisting of identical triangular

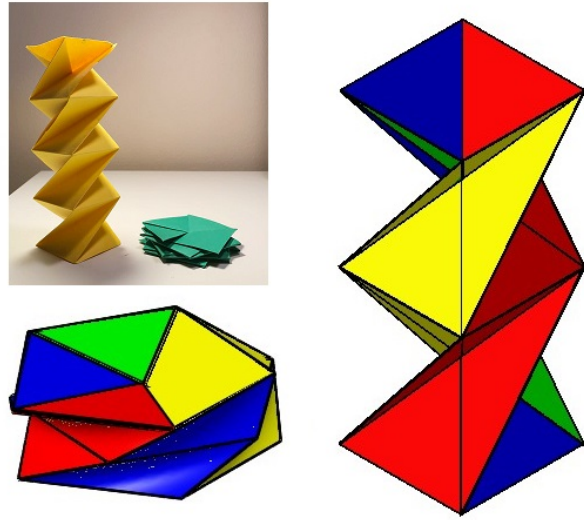


Figure 2.10 Spiral Box Pleat made using Kresling pattern. [52]

panels with cyclic symmetry, functions as spontaneous buckling of a thin cylindrical shell under torsional loading. The incorporation of smart materials, such as electro-active polymers, in origami structures allows them to actively fold using electrical stimuli [50, 52].

The Kresling pattern, named after Biruta Kresling, describes a specific buckled pattern under torsional load. Biruta Kresling proposed that the essence of buckling is not a failure of material but a model from nature that can be understood and designed for engineering applications. A pleat is one of the most common, versatile and easy to use folding techniques. There are multiple types of pleats; accordion, knife, incremental, box and spiral pleat. Combining the spiral pleat with the Kresling pattern can result in box spirals. The pattern can be drawn in one continuous zigzag line, where the strips of trapeziums are divided by equally spaced mountain folds then sloping parallel valley folds placed diagonally between the mountain folds to connect them. The Kresling

pattern is used to form a box spiral. The box spiral creates overlaps of plane, which visually resembles an hourglass. The angle of the sloping valley fold is crucial in determining the shape of the box spiral. By making the angle large, the box will be tall; if the angle is small, the box will be flat. Despite the operation angle being small, it allows the structure to fully collapse and expand obtaining over 700% strain [50, 52, 56].

## Chapter 3. Validation of dielectric elastomers (DE) with ABAQUS

### 3.1 Formulation of Maxwell stress

Among the different groups of soft active polymers, dielectric elastomers are favorable for applications that require large strain. The operation principle of dielectric elastomers are identical to a transducer. When a transducer is subjected to applied voltage, electric charges transmits through the electrode. The opposite charges on the two electrodes cause the elastomer membrane to deform. A membrane of dielectric elastomer is sandwiched between the two compliant electrodes. To experience large deformation, the electrodes need to be compliant and have lower mechanical stiffness than that of the elastomer membrane. Commonly used materials for the electrodes are carbon powder and carbon grease. This behavior allows dielectric elastomers to strain over 100% like rubbers. Large voltage-induced strains, lightweight, silent operation, and fast response speed are desirable traits of dielectric elastomer actuators.

The dielectric elastomer operates like a parallel plate capacitor where the plate capacitor is separated by a thin layer of vacuum as to a thin layer of elastomer for the dielectric elastomer. The separation between the two electrodes may vary but the area of either electrode remains fixed. The charge within the two electrodes are linear with applied voltage. The constitutive equation of state of parallel plate capacitors is shown below.

$$V = \frac{tQ}{\epsilon_0 A} \quad (1)$$

where  $t$  is the distance between the two electrodes,  $Q$  is charge,  $A$  represents the area of the plate capacitor, and  $\epsilon_0$  represents permittivity of vacuum.



$$F(t, Q) = \frac{tQ^2}{2\varepsilon_0 A} \quad (2)$$

$$F = \frac{Q^2}{2\varepsilon_0 A} \quad (3)$$

The applied voltage transmit charges to electrodes with different charges.

Equation 1 relates the applied voltage to the charge. Based on Coulomb's law, the opposite charges attract each other. To maintain equilibrium, a force need to be applied to each electrode. Equation 3 shows the applied force to the charge.

The electric field id defined as  $E = V/t$  and the stress as  $\sigma = F/A$ . This can be written as the following.

$$\sigma = \frac{1}{2} \varepsilon_0 E^2 \quad (4)$$

Equation 4 gives the stress to counteract the electrostatic attraction which is also known as Maxwell stress.

### 3.2 Analytical formulation based on assumptions

Assumptions were made that a body is a sum of many small pieces and the field in each small piece is homogeneous. This assumption allows us to define equalities per unit element. We also assume that the material is incompressible, and ideal dielectric elastomer selected from different types of constitutive hyperelastic models based upon the theory of rubber elasticity.

The equation of state can be determined based upon the nominal density of Helmholtz free energy  $W$ . Helmholtz energy  $W = F/(L_1 L_2 L_3)$ . The three principal stretches can be defined as  $\lambda_i = \frac{l_i}{L_i}$  where  $i = 1, 2, 3$  and nominal stresses by  $S_1 =$

$P_1/(L_2L_3)$ ,  $S_1 = P_2/(L_1L_3)$ , and  $S_3 = P_3/(L_1L_2)$ . The nominal electric field is defined as  $E = V/L_3$ , and nominal displacement as  $D = Q/L_1L_2$ .

The nominal density of Helmholtz free energy can be defined by four independent variables; the three principal stretches  $\lambda_i$  where  $i = 1,2,3$  and the nominal displacement  $D$ . we can find the equation of state that provides the values of the forces and voltage needed to equilibrate with the dielectric in the state for a material model.

$$S_i = \frac{\partial W(\lambda_1, \lambda_2, \lambda_3, D)}{\partial \lambda_i} \text{ for } i = 1,2,3$$

$$E = \frac{\partial W(\lambda_1, \lambda_2, \lambda_3, D)}{\partial D} \text{ for } i = 1,2,3$$
(5)

These sets of equations define stresses as applied forces divided by the area. In absence of the applied force, the stresses become zero even when the voltages cause the dielectric to deform. The applied voltage to the electrodes causes thinning of the elastomer membrane which results in deformation only.

Mentioned above, we replace a parallel capacitor with a thin layer of vacuum with an elastic dielectric elastomer with vanishing stiffness. Recall that electric field and electric displacement can be described as  $E = D/\epsilon_0$ . We can obtain the same equation that leads to the Maxwell stress equation.

The change in shape caused by the electrodes to the elastomer is typically much larger than change in volume. However, the elastomer is regarded as incompressible, meaning that the volume of the material remains unchanged during the deformation so that  $\lambda_1\lambda_2\lambda_3 = 1$ . This assumption places constraints on the three principal stretches making  $\lambda_1$  and  $\lambda_2$  as independent variables whereas  $\lambda_3 = 1/\lambda_1\lambda_2$  expressing  $\lambda_3$  in terms

of  $\lambda_1$  and  $\lambda_2$ . Thus we can rewrite the state of equilibrium based upon incompressibility using three independent variables  $\lambda_1$ ,  $\lambda_2$ , and nominal displacement,  $D$ .

$$\begin{aligned} \left( \frac{\partial W}{\partial \lambda_1} - \frac{\sigma_1 - \sigma_3 + DE}{\lambda_1} \right) \delta \lambda_1 + \left( \frac{\partial W}{\partial \lambda_2} - \frac{\sigma_2 - \sigma_3 + DE}{\lambda_2} \right) \delta \lambda_2 \\ + \left( \frac{\partial W}{\partial D} - E \right) \delta D = 0 \end{aligned} \quad (6)$$

From the equation 6 above, we can constitute the equation of state as following.

$$\sigma_1 - \sigma_3 = \lambda_1 \frac{\partial W(\lambda_1, \lambda_2, D)}{\partial \lambda_1} - ED \quad (7)$$

$$\sigma_2 - \sigma_3 = \lambda_2 \frac{\partial W(\lambda_1, \lambda_2, D)}{\partial \lambda_2} - ED \quad (8)$$

$$E = \frac{\partial W(\lambda_1, \lambda_2, D)}{\partial D} \quad (9)$$

For ideal dielectric elastomer, we assume that the true electric field relates to true electric displacement  $E = D/\varepsilon$ . By integrating the equation with respect to  $D$  while holding the stretches fixed, we can obtain the following equation.

$$W(\lambda_1, \lambda_2, D) = W_s(\lambda_1, \lambda_2) + \frac{D^2}{2\varepsilon} \quad (10)$$

Where  $W_s(\lambda_1, \lambda_2)$  is Helmholtz free energy based upon the stretch and  $\frac{D^2}{2\varepsilon}$  is based upon polarization which contributes to the free energy independently from the principal stretches. Therefore, the electromechanical coupling of an ideal dielectric elastomer is based on geometric effect. For an ideal dielectric elastomer that is incompressible, and homogenous that is treated as a parallel capacitor can be described as below provided the material dielectric constant, and the free energy function for  $W_s$  due to the stretching of the elastomer.

$$\sigma_1 - \sigma_3 = \lambda_1 \frac{\partial W_s(\lambda_1, \lambda_2)}{\partial \lambda_1} - \varepsilon_r \varepsilon_o E^2 \quad (11)$$

$$\sigma_2 - \sigma_3 = \lambda_2 \frac{\partial W_s(\lambda_1, \lambda_2)}{\partial \lambda_2} - \varepsilon_r \varepsilon_o E^2 \quad (12)$$

There are multiple free energy function due to stretching of the elastomers and can be defined by the theory of rubber elasticity. The constitutional hyperelastic models are neo-Hookean, Ogden, Yeoh, Gent, Mooney-Rivlin and Arruda and Boyce models and many more.

For validation between analytical and numerical solutions, the neo-Hookean model was selected to make a comparison between analytical modeling to numerical modeling. Neo-Hookean model can be used to demonstrate strain value up to 50%. The neo-Hookean model uses the free energy function shown below.

$$W_s(\lambda_1, \lambda_2) = \frac{\mu}{2} (\lambda_1^2 + \lambda_2^2 + \lambda_3^2 - 3) \quad (13)$$

The derivative of the equation was taken to find  $\partial W_s(\lambda_1, \lambda_2)$  in different stretch direction.

$$\frac{\partial W_s(\lambda_1, \lambda_2)}{\partial \lambda_1} = \mu(\lambda_1 + \lambda_1^{-2} \lambda_2^{-2}) \quad (14)$$

$$\frac{\partial W_s(\lambda_1, \lambda_2)}{\partial \lambda_2} = \mu(\lambda_2 + \lambda_1^{-2} \lambda_2^{-2}) \quad (15)$$

### 3.3 Analytical validation based on the neo-Hookean model

For the equi-biaxial condition where the stretch are equal, the equation reduced to the following.

$$\frac{\partial W_s(\lambda_1 = \lambda_2)}{\partial \lambda} = \mu(\lambda^2 - \lambda^{-4}) \quad (16)$$

For testing the analytical and numerical solution, the equi-biaxial case will be solved for a stretch of 2. For testing 3 different states will be discussed; the initial state, the pre-stretched state, and the actuated state. A figure with description for each state is added below.

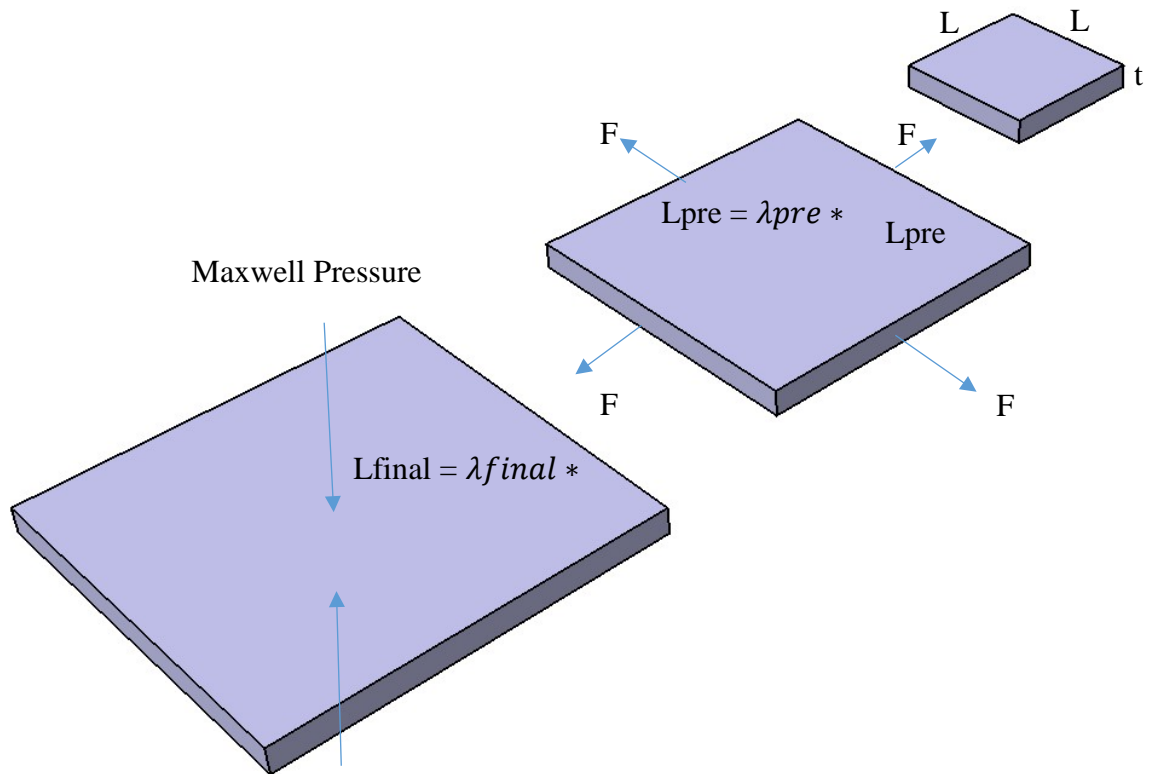


Figure 3.1 (a) Initial state, (b) pre-stretch state, and (c) actuated state of elastomer membrane with dimension notations. The picture is an exaggerated form to aid description.

In the initial state, a square membrane with dimension  $L \times L \times t$ , where the  $L$  is the length of both sides and  $t$  is the thickness when subjected to no force and no voltage.

When subject to force,  $F$  for equi-biaxial stretch, the membrane goes through a change in dimensions where the initial length  $L$  changes to length  $L_{pre}$  which can be described as  $\lambda L$ . The force,  $F$  will be measured through ABAQUS using reaction force along the stretch directions.

For actuated state, the elastomer membrane is subjected to force and Maxwell stress also known as voltage. The membranes have final stretch which is represented as  $\lambda_{final}$  and the stress for stretches as  $\sigma = \lambda \left( \frac{F}{A} \right) = \lambda P$ .

The equation of state reduced to a single equation.

$$\lambda P + (\epsilon_r \epsilon_o) \left( \lambda^2 \frac{V}{t} \right)^2 = \mu(\lambda^2 - \lambda^{-4}) \quad (17)$$

This equation solves for the stretch of the membrane subjected to force F from pre-stretch and voltage from Maxwell stress. For a fixed F from pre-stretch, as voltage varies, the membrane deforms in a succession of state of equilibrium, thus, allowing stretch vs. voltage diagram. By knowing the stretch ratio, the force from reaction force, and shear modulus for a given final stretch, actuation voltage can be found and converted to pressure using Maxwell stress. For the numerical solution, pressure obtained from numerical solution was applied to find the same amount of final stretch.

The analytical solution of dielectric elastomer was done based upon an element cube. The most common material for dielectric elastomer is 3M VHB 4905/4910 tapes. The VHB 4905 has a thickness of 0.5mm and VHB4910 has a thickness of 1mm. The initial element cube for analytical testing will have a dimension of 0.1x 0.1 x 0.1 in mm. The shear modulus of the VHB4910 is 50 kPa with a dielectric constant of 2.86. The cube will be stretched equally for a stretch ratio of 2. After the stretch is applied to the membranes, pressure was applied to the membranes to determine the final stretch, also known as deformation along the planar direction. The free energy function of the neo-Hookean model will be used for bi-axial analysis. The reaction force was measured from ABAQUS to determine how much force is required to stretch the membrane for a given area. The pressure for the pre-stretching was determined and the final deformation also

known as final stretch is pre-determined to be 2.5. This allows us to calculate the voltage also known as the Maxwell stress.

$$\lambda P + (\epsilon_r \epsilon_o) \left( \lambda^2 \frac{V}{t} \right)^2 = \mu (\lambda^2 - \lambda^{-4})$$

$$\lambda 1550 \left( \frac{N}{m^2} \right) + (2.86 * 8.85e^{-12}) \left( \frac{F}{m} \right) \left( \lambda^2 \frac{V}{0.0001} \right)^2 = 50000 \left( \frac{N}{m^2} \right) ((\lambda^2 - \lambda^{-4})) \quad (18)$$

$$\therefore V = 1763 V \cong P = 7867 \left( \frac{N}{m^2} \right) = 7867 Pa$$

Now that we found pressure applied perpendicular, by applying the same pressure to the equation, we can solve for the final stretch. This pressure can be altered to any voltage to find the final stretch of the actuated state. By altering the voltage, stretch vs. voltage plots can be found. For this study, we used the same Maxwell stress value that was identified for comparison. Upon solving for final stretch, we can find multiple solutions. -2.544, -1.019, 1.04294 and 2.499. The value of 2.499 was chosen since the values represent negative stretch which is not adequate since the planar expansion occurs along the element cube thus the value cannot be negative. Besides, 1.04294 is not valid since, before actuation, a pre-stretch of 2 was applied to the membrane. Therefore value 2.499 was chosen as the value for the final stretch.

### **3.4 Numerical validation with ABAQUS using neo-Hookean model by applying pre-stretch using multi-step analysis**

For numerical validation, we validate the unit element cube of the constitutive hyperelastic model based upon neo-Hookean rubber theory. Since the Maxwell stress is determined from analytical testing, the pressure will be applied directly on the membrane. Before solving the analytical model, pre-stretch was applied through ABAQUS using a multi-step function. Through multi-step analysis, reaction force was found and later converted to pressure for analysis.

For modeling, the element cube, 3D deformable isotropic, homogeneous, solid, incompressible, 8 node brick, and the hybrid formulation were used (C3D8H). First step was created for pre-stretching of the elastomer membrane from a stretch ratio of 1 to stretch ratio of 2. During this step, the reaction force was measured to perform the pre-stretch. The second step was created to create a secondary displacement stretch of 2.5 to find the equivalent pressure by using reaction force.

The boundary condition is shown below. Due to multi-step analysis, the initial state restrained the element cube to be idle. For the first step, the displacement of stretch ratio of 2, which is 0.2 mm is applied. During this step, analysis to obtain the reaction force was performed. Once the reaction force was obtained, the analytical solution is solvable. For the second step, displacement of 2.5 was applied as a final stretch and reaction force was measured. This value was compared with an analytical solution later. By solving this using an analytical solution, Maxwell stress was obtained.



To cross-validate, the second step was modified by applying pressure that was solved based upon the analytical solution. The results showed excellent agreement between the two solutions.

The boundary conditions for the two multi-step analysis is shown below.

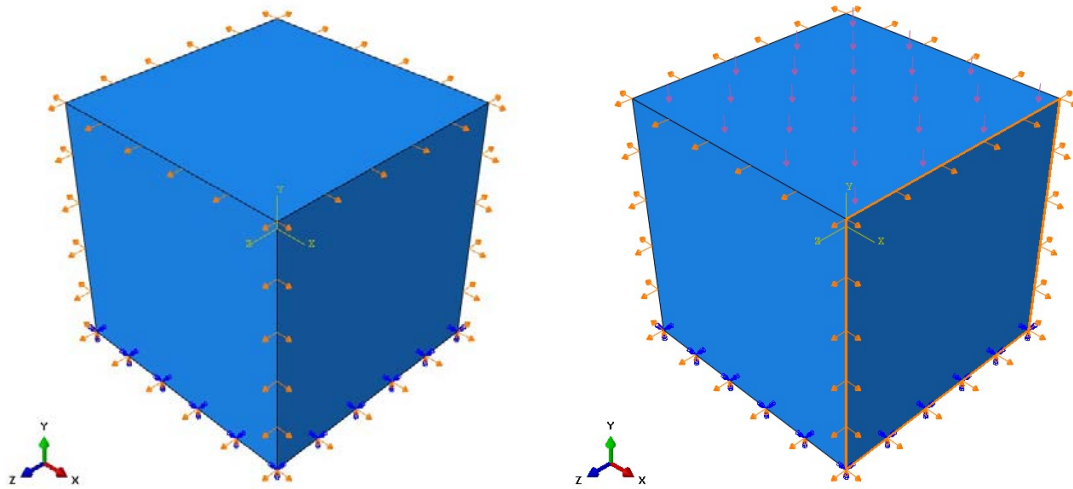


Figure 3.2 (a) Boundary conditions for numerical analysis for pre-stretch with multi-step and (b) boundary condition for numerical analysis involving Maxwell stress with multi-step.

The state of the pre-stretch and actuated state is shown below.

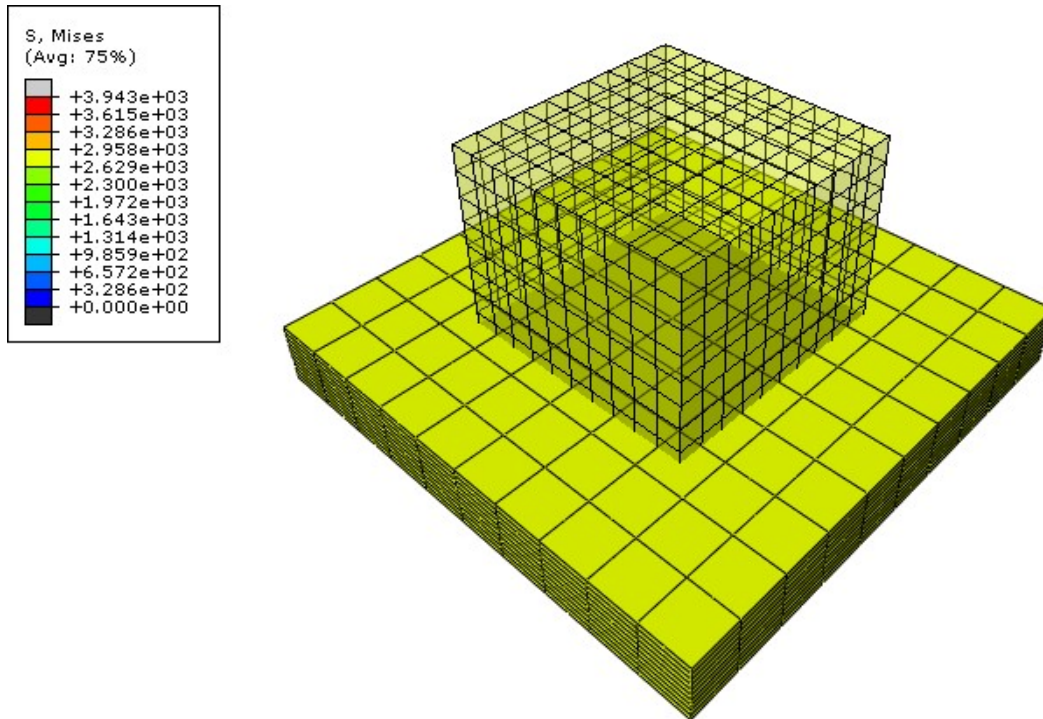


Figure 3.3 Pre-stretch state of numerical analysis

The pre-stretch state is shown in comparison to the initial state. The cube was stretched in the equi-biaxial stretch of 2. As pre-stretched was applied, the element cube experienced thinning in the thickness direction while expansion in the planar direction to stretch of 0.2 mm. The reaction forces were measured for each node to determine the force required to stretch the unit element to stretch of 2. The reaction forces measured for each node were summed up and the average was taken to determine the required force for pre-stretch.

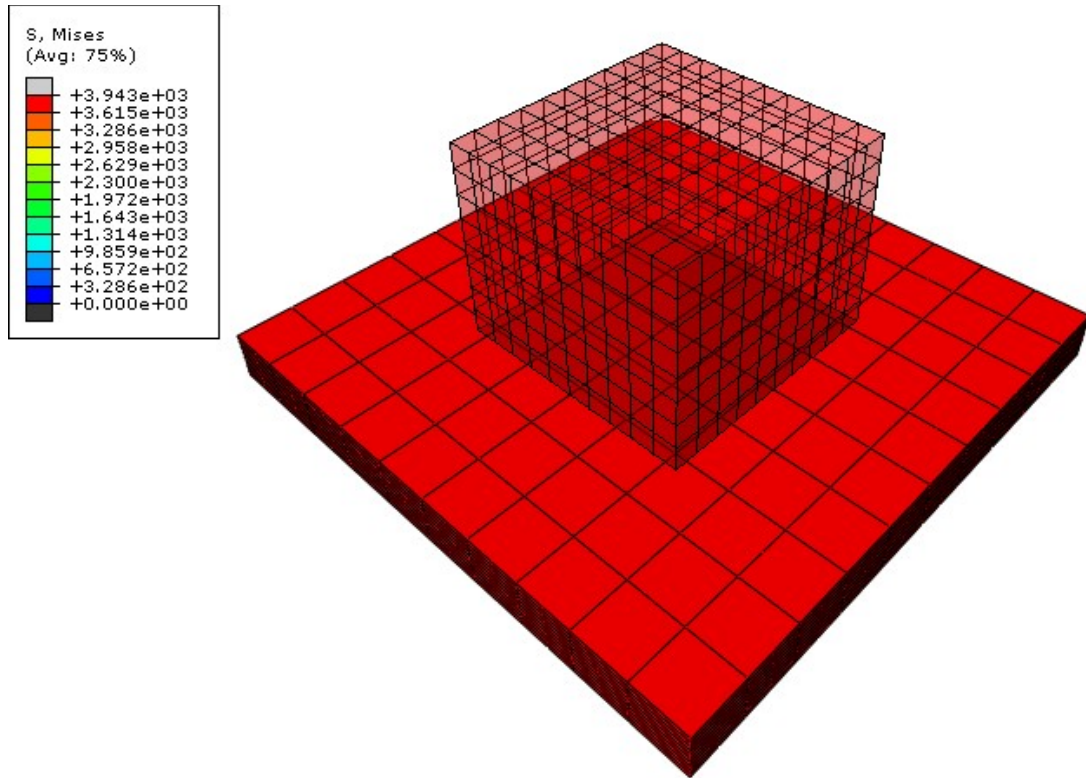


Figure 3.4 Actuated state of numerical analysis

Two cases were studied for actuated state. Based upon the analytical solution, the required Maxwell stress, also known as voltage, was found. After the pre-stretch, the first case study includes applying pressure perpendicular to the elastomer membrane. The second study was conducted by applying a stretch displacement of 2.5. The reaction force required for stretching to the cube element in the planar direction of 2.5 was measured, converted reaction force to pressure and was compared with the analytical model as well as the first case study of the actuated state. The voltage vs. stretch relationship was found using the analytical solution by applying a different voltage and finding the planar stretch of the membrane. This was conducted using ABAQUS to validate the analytical solution provided by equation 17. The analytical and numerical solution shows excellent agreement which is shown below.

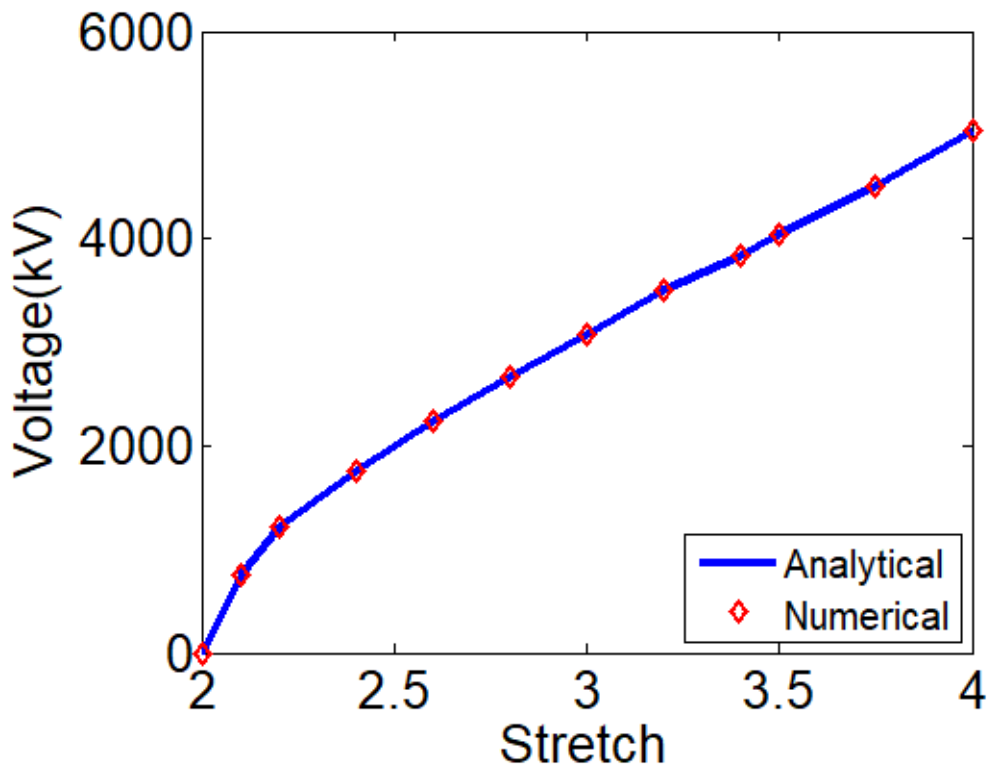
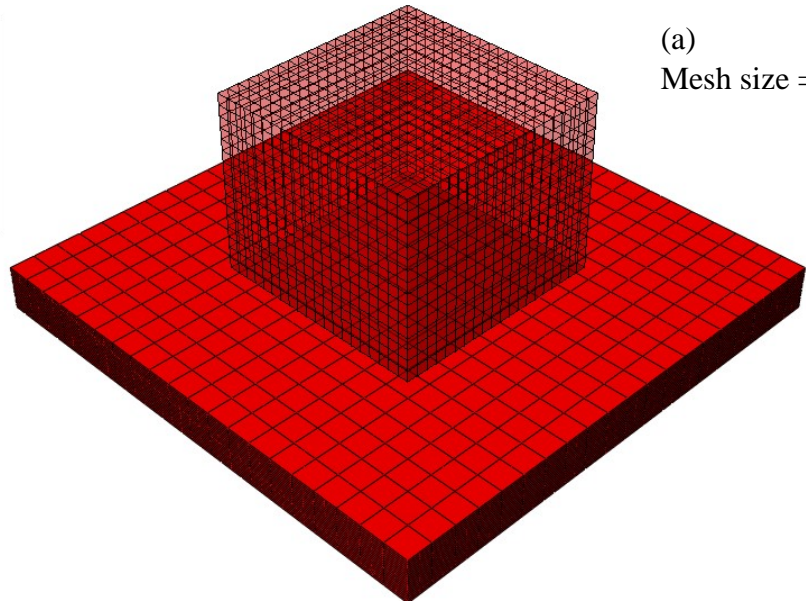
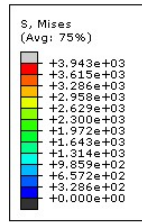


Figure 3.5 Voltage vs. strain relationship for neo-Hookean element unit based upon analytical solution. The values were validated using numerical analysis using ABAQUS.

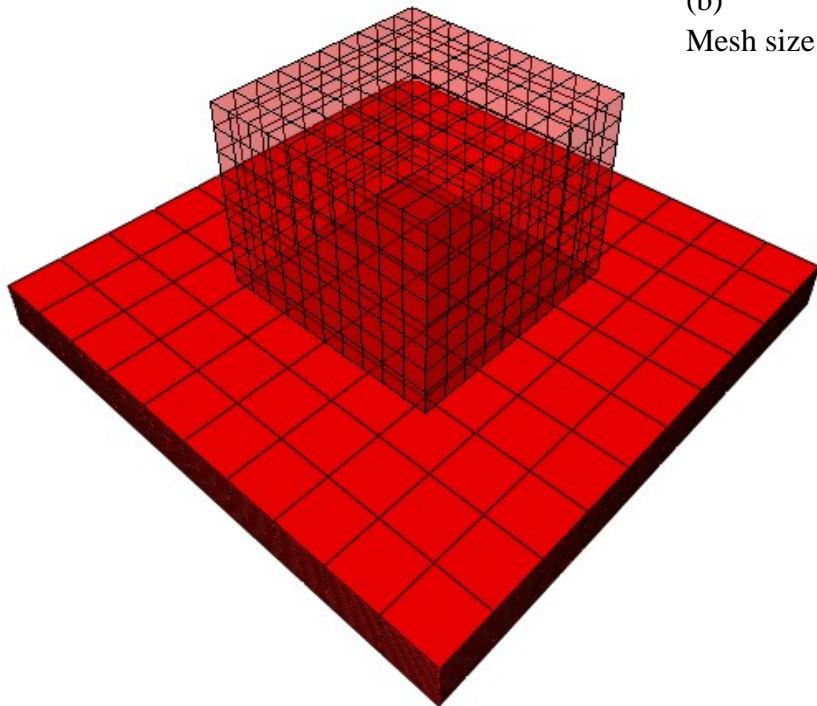
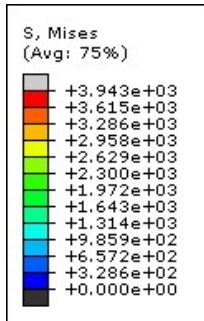
### 3.5 Mesh Refinement

Mesh refinement is a very important factor for determining an accurate solution in numerical analysis. Mesh refinement essentially divides the existing elements in half. As a result, mesh refinement operations approximately quadruple the number of area elements and increase the number of volume element by a factor of eight. Therefore mesh refinement was conducted until convergence to determine whether the solution is accurate.

Different size meshes were used to determine whether the size of the mesh was properly implemented for the analysis. Mesh size of 0.1 and 0.05 was used to determine the mesh on the cubic element was sufficient. Comparisons were made for different mesh size 0.1 and 0.05.



(a)  
Mesh size = 0.05



(b)  
Mesh size = 0.1

Figure 3.6 Mesh refinement comparison between mesh size (a) 0.05 and (b) 0.1 for stress

The comparison of stress on the unit element shows identical values between the two mesh sizes. The solutions between the two mesh refinements are identical, thus shows the two different mesh converges and the solution is accurate. Therefore, the previous

numerical solution based on the mesh size of 0.1 is accurate in comparison to the analytical solution as well as a finer mesh size of 0.05.

### **3.6 Conclusion**

Elastomers are capable of going through large deformations. To develop different applications using elastomer materials with electromechanical coupling, a better understanding of the behavior of the material is required. In this portion of the study, the numerical modeling method have been developed to make a direct comparison with analytical models involving the idea of pre-stretch and Maxwell stress using constitutive hyperelastic material behavior. Based on the comparison between the results obtained from analytical calculations and the numerical analysis performed in ABAQUS, excellent agreement of results indicate successful implementation of numerical analysis through ABAQUS.

## Chapter 4. Helical Dielectric Elastomer Actuator

### 4.1 Introduction - Hyperelastic Material

Before going into constitutive hyperelastic material models, strain and stress tensor were recalled. Then non-linear incompressible hyperelasticity will be derived. For an elastomer, it can be considered rubber-alike. We consider the deformation of an elastomer and denote  $F$  as the local gradient of the deformation. The right and left Cauchy-Green deformation tensors can be defined by the following equation.

$$C = F^t F \text{ (right)} \quad \text{and} \quad B = F F^t \text{ (left)} \quad (19)$$

The right and left Cauchy-Green deformation tensor can be noted by the three principal invariants denoted by  $I_1$ ,  $I_2$  and  $I_3$ . The three principal invariants are defined as following while  $C$  can be replaced by  $B$ ,

$$I_1 = \text{tr}(C) \quad (20)$$

$$I_2 = \frac{1}{2} [\text{tr}(C^2) - \text{tr}(C)^2] \quad (21)$$

$$I_3 = \det(C) \quad (22)$$

where ' $\text{tr}$ ' is the trace operator and ' $\det$ ' is the determinant operator. For incompressible materials  $I_3 = 1$ . The stretch ratios are defined as the square roots of the eigenvalues of  $C$  and are denoted as  $\lambda_1$ ,  $\lambda_2$  and  $\lambda_3$ . Using the stretch ratios, the three principal invariants can be reduced as the following.

$$I_1 = \lambda_1^2 + \lambda_2^2 + \lambda_3^2 \quad (23)$$

$$I_2 = \lambda_1 \lambda_2^2 + \lambda_2 \lambda_3^2 + \lambda_1 \lambda_3^2 \quad (24)$$

$$I_3 = \lambda_1^2 \lambda_2^2 \lambda_3^2 \quad (25)$$

Stress is the internal cohesion of forces within a matter. For large strain problems, two major stress tensors are considered known as true stress tensor  $\sigma$ , also known as Cauchy and the nominal stress tensor  $P$ , also known as Piola-Kirchhoff stress tensor. The two stress tensors can be described by the following relation,

$$P = \det(F) \sigma F^{-t} \quad (26)$$

in which the exponent denotes the transpose of the inverse.

Based on theory of hyperelasticity, it is assumed that stress tensors derive from strain energy function depends on the left strain tensor  $B$  and is denoted by  $W$ . As mentioned, for incompressible materials,  $I_3 = 1$ . The stress tensors depend on both strain and an arbitrary scalar parameter  $p$ , which can be determined with the following equation.

$$\sigma = 2B \frac{\partial W}{\partial B} - pI \quad (27)$$

$$P = \frac{\partial W}{\partial F} - pF^{-t} \quad (28)$$

where  $I$  is the identity tensor. Now making the assumption that the material is isotropic, the strain energy function only depends on the two first strain invariants and stress tensors can be rewritten as the following.

$$\sigma = 2 \left( \frac{\partial W}{\partial I_1} + I_1 \frac{\partial W}{\partial I_2} \right) B - 2 \frac{\partial W}{\partial I_2} B^2 - pI \quad (29)$$

$$P = 2F \left[ \left( \frac{\partial W}{\partial I_1} + I_1 \frac{\partial W}{\partial I_2} \right) I - \frac{\partial W}{\partial I_2} C \right] - pF^{-t} \quad (30)$$

These equations are further reduced in terms of principal stretch ratios,

$$\sigma = 2 \left( \lambda_i^2 \frac{\partial W}{\partial I_1} - \frac{1}{\lambda_i^2} \frac{\partial W}{\partial I_2} \right) - p \quad (31)$$



$$P = 2 \left( \lambda_i^2 \frac{\partial W}{\partial I_1} - \frac{1}{\lambda_i^3} \frac{\partial W}{\partial I_2} \right) - p \frac{1}{\lambda_i^2} \quad (32)$$

where  $I = 1, 2$  and  $3$  based on the principal stretch directions.

There have been different types of constitutive models for hyperelastic models and are classified by different formulation depending on the approach of strain energy function. Some have been using mathematical developments of free energy function  $W$  and identified material parameters. The other groups have been determining hyperelastic models through experimental data. There have been over 15 hyperelastic model theories developed since 1940. However, several models that have demonstrated phenomenal modeling. In this research, neo-Hookean, Ogden, Gent, and Mooney-Rivlin were used and will be further discussed in depth in later section [54, 56].

#### **4.2 Helical Dielectric Elastomer Actuator (HDEA)**

Helical DEA (HDEA) is one type of electronic EAP that was first proposed by Carpi [10, 12, 14] in 2005. A HDEA with its unique helical configuration does not only provide a contractile and extendable capabilities, but also can aid in attaining results for bending and torsion. The helical dielectric elastomer analyzed in Carpi's paper has one degree of freedom (DOF), but it has been investigated that multiple DOFs can be achieved by changing the patterns in the electrodes around the helix. Compared to a stacked DEA, the benefits of continuous DEA were not investigated before. The continuous DEA shows benefits where it will require less wiring and the structure itself can provide torsion and increase in stiffness. As a result, the structure of the HDEA was investigated [10, 12, 13, 50].

### **4.3 Numerical Analysis of HDEA**

#### **4.3.1 Research Objective**

A helical dielectric elastomer actuator (HDEA) with its unique configuration does not only provide the contractile and extendable capabilities, but also enables bending and torsional motions. This study focuses on the numerical analysis of HDEA with helical compliant electrodes. Numerical analysis of the designed HDEA is to be conducted to confirm the accuracy of the model to known results. Applying the material characteristics into the simulation, the functionality of HDEA for various activations can be achieved. Before applying these characteristics for HDEA to obtain results, validation of modeling was conducted for comparison purpose [10, 12, 13, 50].

#### **4.3.2 Validation Process – Disk Validation and Single Layer**

Disk-shape dielectric elastomer (DDEA) was one of the validation methods that was used to compare with HDEA. A disconnected model of DDEA is shown below. When voltage is applied, the multi-layered stack disk compresses. The supply line is where the voltage is applied. The DDEA has a diameter of 14 mm and a length of 70 mm. In Kovac's paper [4, 9], non-loaded contraction of the displayed actuator is about 30%. In addition, for a single layer DEAP, 40% contraction and 160 N/m<sup>2</sup> of actuation pressure can be achieved with a successful manufacturing procedure. The desired actuation pressure is applied to the DDEA model in ABAQUS to determine the deformation. For numerical analysis validation, instead of voltage, a force is applied on the electrode region to simulate the deformation of the DDEA. This force is converted to Maxwell's pressure to obtain results for validation.

$$P_{el} = |F|/A = |\nabla U|/A = |\nabla \left(\frac{1}{2}\right) CV^2|/A = \varepsilon_0 \varepsilon_r E^2 \quad (33)$$

Furthermore, using Maxwell's pressure, knowing the material permittivity  $\varepsilon_r$  and vacuum permittivity  $\varepsilon_0$ , the value for electric field strength ( $E$ ) is obtained.

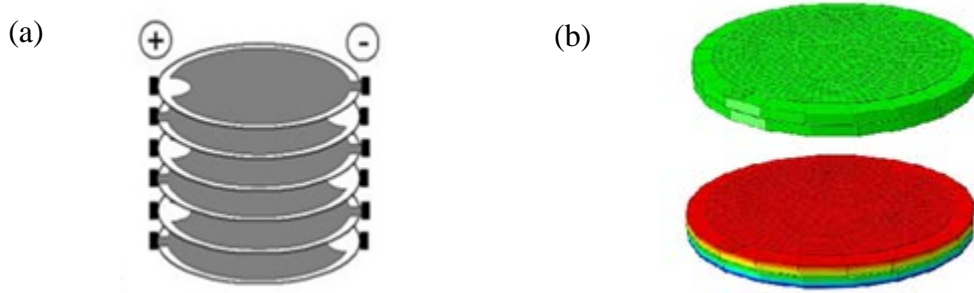


Figure 4.1 (a) Configuration of Disk Dielectric Elastomer based upon Kovac *et al.* (b) Numerical validation was performed to validate FEA modeling method. [4, 9]

In Kovac's paper, 30% strain, which is 21 mm of contraction deformation, was achieved through desired actuation pressure. Converting the actuation pressure into voltage, 10 kV was needed to achieve such deformation. In order to achieve 30% contraction deformation, a voltage of 57 kV needs to be applied as shown in the validation [9].

In Kovac's paper, it is emphasized that the dielectric film is pre-strained in planar directions, which alters the activation voltage level, as well as overall performances. However, in the simulation conducted for validation, pre-strain was not applied to the material. Therefore, it affected the desired actuation pressure as well as the actuation voltage. Although there is a difference between the voltages, the trend for contractive strains, as well as the variation in thickness of the DDEA match to that of Kovacs's paper. If pre-stretch were applied to the numerical analysis, the voltage could be significantly lower and would generate similar results shown from the paper [9].

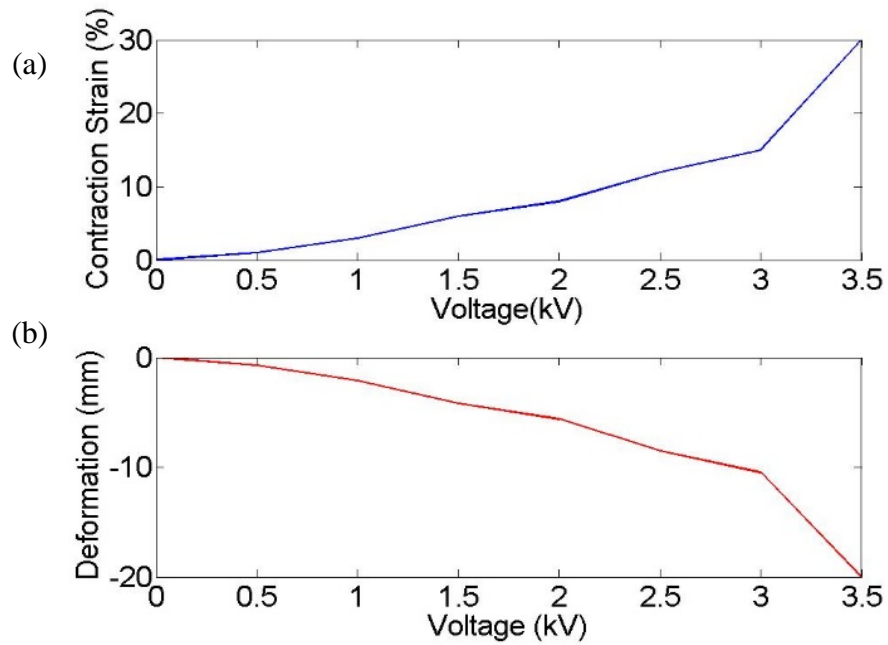


Figure 4.2 (a) Voltage vs. contraction strain (%) and (b) voltage vs. deformation data acquired from Kovacs's paper.

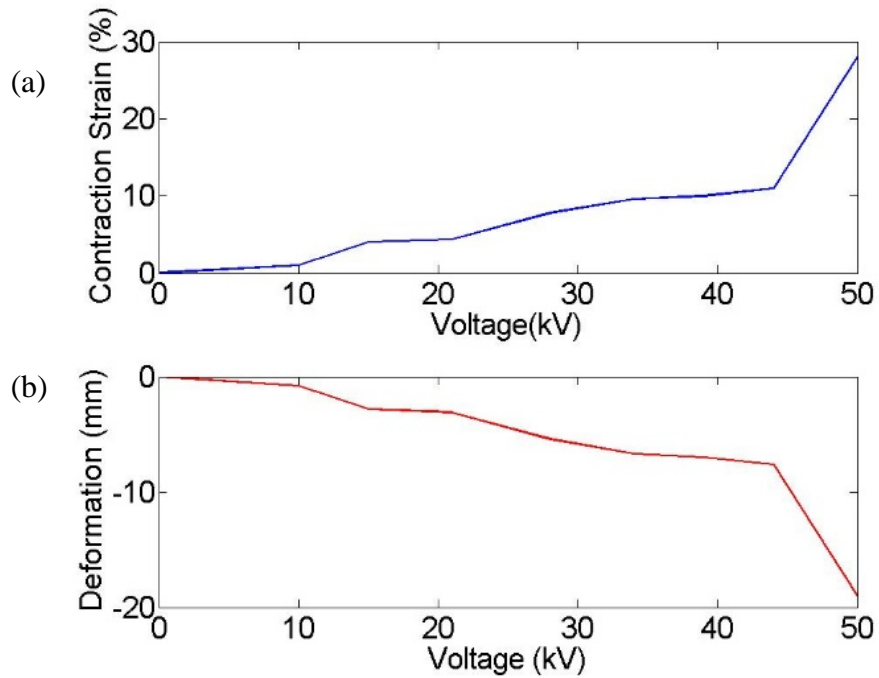


Figure 4.3 (a) Voltage vs. contraction strain (%) and (b) voltage vs. deformation validation data from ABAQUS DDEA Model.

### 4.3.3 Results

Single layer elastomer actuator (SLDEA) was also used as validation procedure for the HDEA model. As mentioned above, for a single layer elastomer actuator, 40% contraction from  $160 \text{ N/m}^2$  could be achieved theoretically. Therefore, single layer elastomer actuator squeezed between two electrodes was also used to validate for HDEA [10, 12, 13, 50].

In this simulation,  $700 \text{ N/m}^2$  actuation pressure was needed to achieve a 40% contraction, while  $160 \text{ N/m}^2$  was the desired value. This means that the actuation voltage of approximately 3 kV is needed for that pressure. This yielded a value of 12% contraction strain when  $160 \text{ N/m}^2$  pressure is applied to the specimen. As the result, there were limitations in the validation process, since pre-stretch (strain) was not applied to the simulation. In manufacturing of DEA or experimentations, pre-stretch is generally applied to the elastomer before the electrodes are added or before applying voltage. Similarly, considering that there was no pre-stretch in the simulations for DDEA and SLDEA, a high voltage requirement was seen from the validation of results. After validation has been conducted, the results obtained from simulations of HDEA are discussed below.

A single layer HDEA results were analyzed and compared to the analytical solution. Figure 3.4 shows the axial simulations obtained from ABAQUS for a single layer with 5 mm radius and 0.5 mm elastomer thickness. Different vertical displacement values were extracted by varying pressure from 4 kPa to 40 kPa and compared with the analytical model.

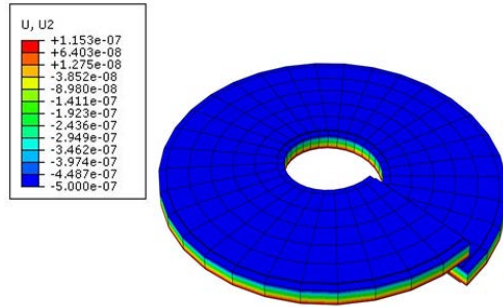


Figure 4.4 Axial deformation for single layer HDEA.

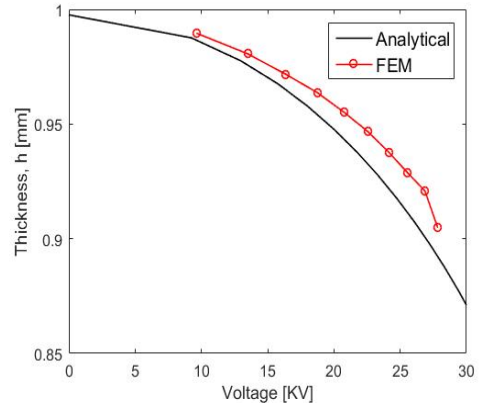


Figure 4.5 Comparison of analytical<sup>13</sup> and numerical solution.

It can be seen that the finite element method (FEM) results are comparable to the analytical model. The small difference in between the values is due to the different dimensions of the model being used. Once the numerical method was verified, analysis for the multilayer HDEA model was conducted. Further analysis was done to demonstrate the deflection of a multi-layer HDEA. The relationship between Maxwell's pressure and electric field allows to convert mechanical properties, e.g., pressure to voltage. Since the HDEA model was not pre-strained, there are some limitations to this simulation.

In the simulation, elastomer with a thickness of 0.5 mm and electrode with a thickness of 0.05 mm were used based on the hyperelastic material properties of 3M VHB 4910 tape. The elastomer of the HDEA had an outer radius of 7 mm and an inner radius of 2 mm. The electrode of the HDEA was 0.3 mm shorter from each side of the elastomers edge to avoid short circuits. Neo-Hookean model was used for modeling the analysis for the HDEA with hyperelastic behavior. Two revolutions of the HDEA were designed with a pitch of 1.1 mm. Equally distributed forces were applied along the

electrode of the HDEA. From the applied forces, actuation pressure is determined to derive actuation voltage and hence its deformation.

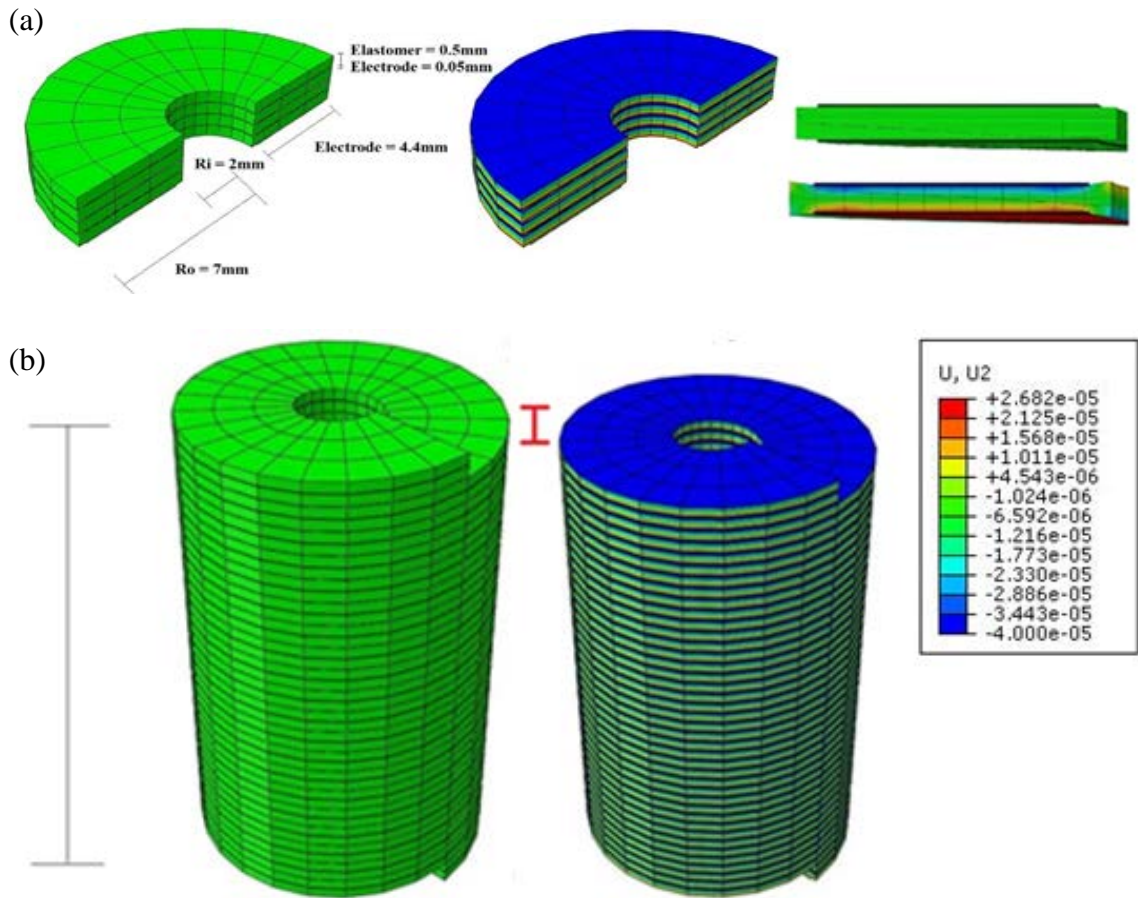


Figure 4.6 (a) Configuration of 2 layers of HDEA and (b) 10 layers of HDEA and the geometrical dimensions.

Figure 3.6, 2 layers HDEA shows the configuration of the HDEA before and after the load was applied. It can be noticed that there is compression between the electrodes when forces are applied. It shows that the elastomers are being compressed due to the actuation pressure of the electrodes. Studies for DEAP were done to compare the model as well as to validate the method used in this HDEA simulations. For 2 layers HDEA, the total height of the electrode was 3.3 mm and had 0.397 mm deformation which was about 12% total deformation. More layers were added after conducting numerical analysis for 2

layers and to show the compression in larger a specimen with a height of 16.5 mm and the remaining dimensions stay the same.

Figure 3.6, 10 layers HDEA shows the deformation gradient based on the actuation pressure. It can be seen that there is compression within the layers of elastomer and hence compressing the entire specimen of 10 layers. The total thickness of the HDEA was 16.5 mm. Forces ranging from 1000 N to 3000 N with 250 N intervals were used to determine the voltage in order to find the deformation that corresponds to the applied forces. Voltage ranging from 5.4 kV to 56.6 kV was used to identify the change in height and percent deformation as shown in Figure 3.7 below.

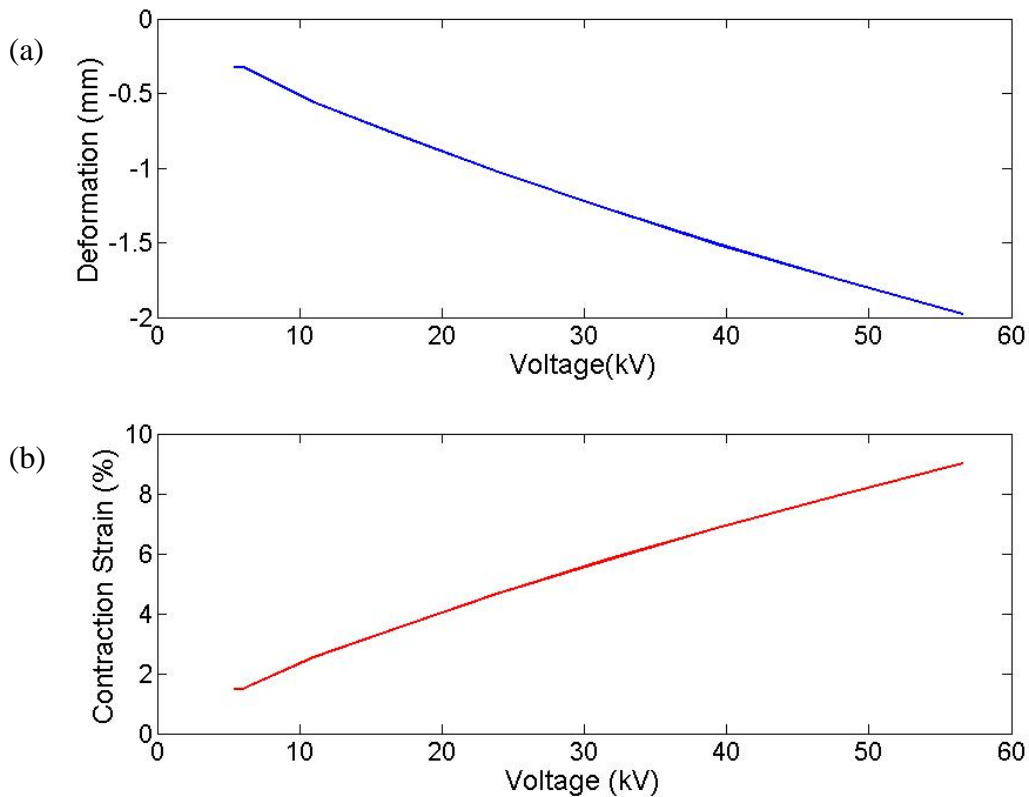


Figure 4.7 (a) Voltage vs. height and (b) voltage vs. contraction strain (%) deformation of 10 layers HDEA.



The following deformation shown in Figure 3.7 was achieved when distributed force along the electrodes was increased with an interval of 250 N. The max deformation was achieved at 56.6 kV with a 2.2 mm deformation. This is about 13.3% deformation in length of the HDEA. From the following results, it is clear that the deformation on the HDEA occurs when actuation pressure is applied to the electrodes on the HDEA. However, again the major limitation in the simulation is that there was no pre-stretch applied. Taking no pre-stretch into account, the activation voltage of actual HDEA still seems to be promising.

Different electrode placements were discussed above as a method to achieve bending actuation. The electrode was placed across while one side of the electrode was actuated, the other remained. The results of the simulation and geometrical configuration are shown below.

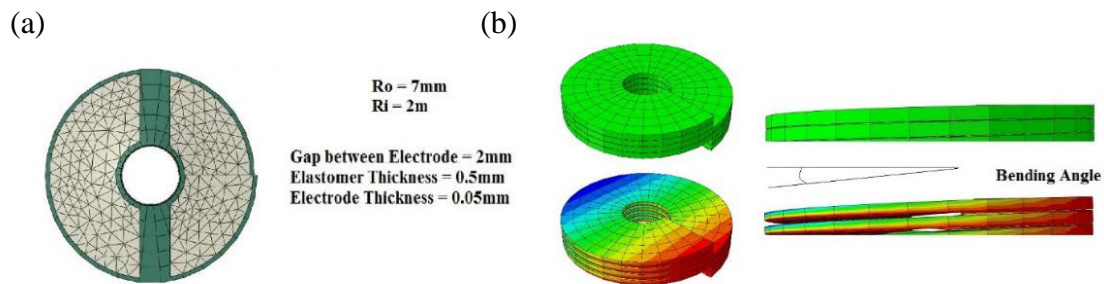


Figure 4.8 Electrode placement and geometrical parameters of HDEA. The bending of HDEA was measured.

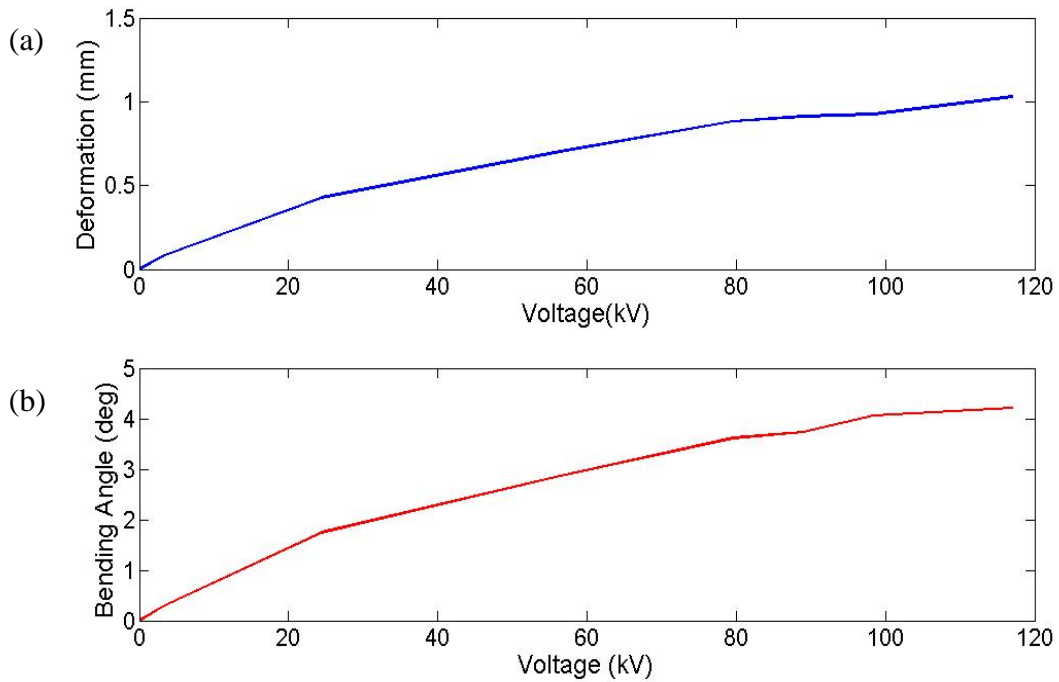


Figure 4.9 Voltage vs. contraction and voltage vs. bending angle for 2 layers of HDEA.

The above results show the fact that HDEA can be designed not only for axial deformation but also bending deformation, by activating certain electrode patterns. Also, with an increase in voltage, HDEA can be seen to generate a larger bending angle. At 117 kV, there is a total of 4.2-degree angle of bending for this 2 layers HDEA with 1 mm deformation. The bending angle was expected to be near the pitch angle which was 3 degrees. One of the major reasons for the large voltage requirement for activations is again due to the pre-stretch not being applied in the model.

#### 4.4 Optimization of Geometrical Parameters of HDEA

In the previous numerical simulation, optimizing the thickness and geometrical parameters can improve the performance of the HDEA. Therefore, geometric modeling was performed based on a helicoid. Geometric modeling of the HDEA can be studied by

analyzing the geometry of a helicoid. The complex nature of the helicoid comes from the pitch angle that makes the geometry continuous thus makes the calculation of the surface area more complex. The surface area is required in Maxwell's stress equation to formulate the electromechanical relationship of the actuator which is shown above as equation 33 [10, 12, 13, 50].

A pitch angle is very similar to what is called lead angle when it comes to machinery tools. The lead angle ( $\beta$ ) is a measure of the inclination of a screw thread from a plane that is perpendicular to the screw thread axis. This idea of lead angle can be used to find the pitch angle of the helicoid.

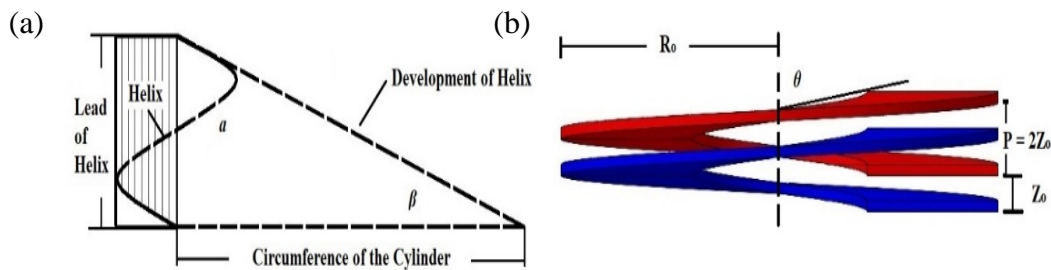


Figure 4.10 (a) Explanation of lead angle to explain the pitch angle used in helical structures and (b) other parameters that are involved in helicoid geometric calculation using parametric equations.

Based upon the definition of lead angle, the pitch angle of a helix can be described as an angle between the slanted surface and a plane perpendicular to the direction of the inclination. The pitch angle can be represented by the following expressions:

$$Pitch\ angle = \tan(\beta) = \frac{Pitch}{2\pi r_o} \quad (34)$$

where the pitch of the helicoid is  $Pitch = 2z_o$  where  $z_o$  represents the thickness of the elastomer.

In order to calculate the contact surface area, with reference to the z-axis of the Cartesian coordinate system being the axis of the HDEA, the cylindrical coordinate system can be used to describe the helicoid. Vertical displacement  $z$  of the helicoid can be described by a slant  $c$ , and an azimuth angle  $\theta$  in the cylindrical coordinate system. This equation can be written as:

$$\frac{y}{x} = \tan\left(\frac{z}{c}\right) \quad (35)$$

The following parametric equations can be derived from equation 35.

$$\phi(r, \theta) = \begin{cases} x = r \cos \theta \\ y = r \sin \theta \\ z = c\theta \end{cases} \quad (36)$$

The  $\phi$  represents the position vector and the  $r$  is the radial position of any particle within the boundaries of the helicoid. The main properties that are of interest are the inner and outer length of the helix  $L_o$  and  $L_i$ . The infinitesimal line integral over the length of the inner and the outer radius of the helicoid is calculated.

$$\frac{\partial \phi}{\partial \theta}(r, \theta) = \begin{cases} \partial x = -r \sin \theta \partial \theta \\ \partial y = r \cos \theta \partial \theta \\ \partial z = c \partial \theta \end{cases} \quad (37)$$

The infinitesimal length can be then calculated:

$$\begin{aligned} \partial L &= \sqrt{\partial x^2 + \partial y^2 + \partial z^2} = \sqrt{r^2(\sin^2 \theta + \cos^2 \theta) + c^2} \partial \theta \\ &= \sqrt{r^2 + c^2} \partial \theta \end{aligned} \quad (38)$$

The inner and outer length of the helicoid can be determined:

$$L_i, L_o = \int \partial L = \int_0^{2\pi} \sqrt{r^2 + c^2} \partial \theta = 2\pi r_{i,o} \sec \beta \quad (39)$$

By substituting  $C = \frac{P}{2\pi}$  and the pitch  $P$  to equation 39, we can find an expression for the inner and outer length of the helicoid curve. When a single period of the helicoid

is rectified, the area resembles a disk shape area enclosed by the inner and outer length of the helicoid [10, 12, 13, 50].

The rectified surface of the helicoid actuator looks identical to a disk and the area can be found by subtracting the smaller radius with the larger radius. Since the length  $L$  represented the circumference of the inclined radius  $R_{i,o}$  referred as the actual radius of the helicoid, the area of the helicoid for a single revolution can be found.

$$Area = \pi Actual R_o^2 - \pi Actual R_i^2 = \pi r_o \sec \beta^2 - \pi r_i \sec \beta^2 \quad (40)$$

#### 4.4.1 Electromechanical Modeling

The electric field  $E$  between the two layers of the electrode can be determined by applying Gauss theorem to an enclosed area of a single revolution of the helical dielectric elastomer actuator,

$$\oiint_S \vec{E} \cdot \vec{n} \partial S = \frac{Q}{\epsilon_r \epsilon_o} \quad (41)$$

where  $\vec{n}$  is the unit vector pointing toward the normal surface. The electrode layers are parallel to each other thus being identical to each other, which leads to the following equation.

$$|\vec{E}| = \frac{Q}{\epsilon_r \epsilon_o A} = \frac{Q}{(\pi r_o \sec \beta^2 - \pi r_i \sec \beta^2) \cdot (\epsilon_r \epsilon_o)} \quad (42)$$

The distance of the two parallel electrodes can be represented as the thickness of the elastomer  $t_{elastomer}$ . This leads to another expression that involves the relationship of voltage and electric field.

$$V = \int_0^t \vec{E} \cdot \partial \vec{t} = |\vec{E}| t \quad (t = t_{elastomer}) \quad (43)$$

The expression of capacitance for the two parallel electrodes can be found as the following.

$$C = \frac{Q}{V} = \frac{\epsilon_r \epsilon_o A}{t} = \frac{\epsilon_r \epsilon_o \cdot (\pi r_o \sec \beta^2 - \pi r_i \sec \beta^2)}{t} \quad (44)$$

Dielectric elastomer actuators experience changes in surface area and thickness when voltage is applied and the electrode layers are charged. The surface area increases while the thickness of the elastomers decreased due to compression. In addition, we assume that the elastomer is incompressible. In order to express this behavior, a gradient equation can be written in the expression of the differential  $U$ . Due to the assumption of the elastomer layer being incompressible, the volume is preserved. Since there is no change in volume,  $\partial(Ah) = 0$  where  $A\partial t + h\partial A = 0$ .

$$\begin{aligned} \partial U &= \partial \left( \frac{1}{2} \cdot \frac{\epsilon_r \epsilon_o A V^2}{t} \right) = \frac{\partial U}{\partial t} \partial t + \frac{\partial U}{\partial A} \partial A \\ &= \frac{1}{2} \cdot \epsilon_r \epsilon_o V^2 \cdot \left( -\frac{A}{t^2} \partial t + \frac{\partial A}{t} \right) = -\epsilon_r \epsilon_o V^2 \cdot \left( \frac{A}{t^2} \partial t \right) \end{aligned} \quad (45)$$

By substituting  $\partial U$  in to the equation 45, the following equation describes the electrostatic pressure generated by the electrodes which is similar to the equation that involves capacitance.

$$p_{el} = \frac{1}{A} \cdot \left| \frac{\partial U}{\partial t} \right| = \epsilon_r \epsilon_o E^2 = \epsilon_r \epsilon_o \frac{V^2}{t^2} \quad (46)$$

#### 4.4.2 Hyperelastic Material

The mechanical behavior of hyperelastic materials can be characterized by the strain energy functions, such as Neo-Hookean, Yeoh, Mooney-Rivlin and Ogden forms.

In Yeoh form, the strain energy function depends on  $I_1$ , the first invariant of left Cauchy-Green deformation tensor,

$$W = C_{10}(I_1 - 3) + C_{20}(I_1 - 3)^2 + C_{30}(I_1 - 3)^3 \quad (47)$$

where  $C_{10}$ ,  $C_{20}$  and  $C_{30}$  are material parameters and  $I_1$  can be determined from the eigenvalues of deformation tensor also known as stretch ratios  $\lambda_i$  (where  $i = 1, 2$  and  $3$  direction).

$$I_1 = \lambda_1^2 + \lambda_2^2 + \lambda_3^2 \quad (48)$$

While solving for the strain functions, assumptions are made that the materials (i) incompressible and (ii) isotropic in the pre-deformed configuration.

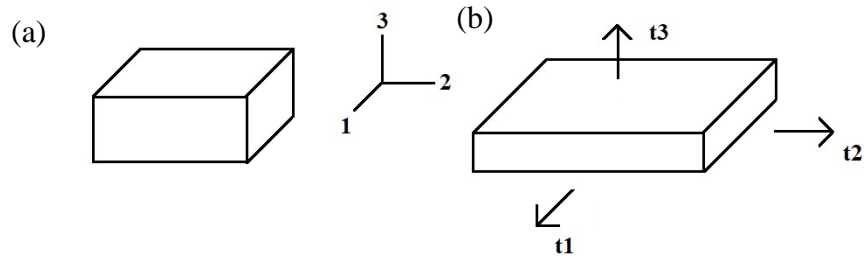


Figure 4.11 (a) Orientation of x, y, z direction shown as 1, 2, 3 and the (b) corresponding Cauchy stress.

The direction of Cauchy stress is shown above. The Cauchy stress ( $t_i$ ) can be determined where  $p$  is the hydrostatic pressure that depends on kinetic boundary conditions.

$$t_i = \lambda_i \frac{\partial W}{\partial \lambda_i} - p \quad (\text{where } i = 1, 2, 3) \quad (49)$$

Based upon the second assumption, in order to determine the kinetic boundary conditions, biaxial tension was used to find the Cauchy stresses. Equal stretches in direction 1 and 2, as well as out-of-plane contraction occurs during biaxial tension. As a

result, the stress in direction 3 is zero. Based on isochoric deformation ( $\lambda_1\lambda_2\lambda_3 = 1$ ), the principal stretch ratios can be determined.

$$\lambda_3 = \frac{1}{\lambda_1^2} = \frac{1}{\lambda_2^2} \quad (50)$$

The Cauchy stress equation can be determined by equation 51 and the kinetic boundary conditions. Cauchy stress  $t_1 = t_2$  can be calculated for the Yeoh Strain energy form,

$$t_1 = t_2 = \lambda_1 \frac{\partial W}{\partial \lambda_1} - \lambda_3 \frac{\partial W}{\partial \lambda_3} \quad (51)$$

where

$$H_i = \lambda_{i_{act}} \frac{\partial W}{\partial \lambda_{i_{act}}} \quad (52)$$

therefore, Yeoh strain energy form can be calculated as:

$$H_k = \lambda_k \frac{\partial W}{\partial \lambda_k} = 2\lambda_k [C_{10} + 2 \cdot C_{20}(I_1 - 3) + 3 \cdot C_{30}(I_1 - 3)^2] \quad (53)$$

Combining equations 52 and 53 allows Cauchy stress to be calculated for  $t_1=t_2$ .

Since the focus of this paper is based upon additive manufacturing parameters, pre-straining is not included as a part of the procedure. Therefore, there are only two configurations that will be used for analytical modeling: non-activated and activated. The activation of the dielectric elastomer actuator (DEA) results in a reduction in the thickness of the elastomer membrane. Change in the thickness due to the electrostatic force will be represented by a parameter  $k$ . Since the compressive force will be applied, parameter  $k$  can be represented by the following relation.

$$0 < k < \frac{1}{\lambda_{1 \text{ non-act}}^2} \quad (54)$$



The first assumption that the material is incompressible leads to the fact that the activated stretch ratio can be written in the function of non-activated stretch ratio  $\lambda_1$  and  $k$ .

$$\lambda_{1act} = \frac{1}{\sqrt{\lambda_{3act}}} \text{ where } \lambda_{3act} = \frac{1}{\lambda_{1non-act}^2} - k \quad (55)$$

From equation 55, activated Cauchy stress can be determined for direction 1 and 2.

$$t_{1act} = H_{1act} - p_{act} \quad (56)$$

Activated hydrostatic pressure can be determined.

$$\begin{aligned} P_{activated} &= H_{1act} - t_{1non-act} \\ &= \lambda_{1act} \frac{\partial W}{\partial \lambda_{1act}} - \lambda_{1non-act} \frac{\partial W}{\partial \lambda_{1non-act}} + \lambda_{3non-act} \frac{\partial W}{\partial \lambda_{3non-act}} \end{aligned} \quad (57)$$

Cauchy stress in direction 3 can be obtained.

$$t_{3act} = H_{3act} - p_{act} = \lambda_{3act} \frac{\partial W}{\partial \lambda_{3act}} - \lambda_{1act} \frac{\partial W}{\partial \lambda_{1act}} + t_{1non-act} \quad (58)$$

Cauchy stress in direction 3 corresponds to the contracting electrostatic pressure acting across the electrodes. Combining the Cauchy stress with the Maxwell pressure equation, the following equation can be derived.

$$p_{el} = \frac{1}{A} \cdot \left| \frac{\partial U}{\partial t} \right| = \varepsilon_r \varepsilon_o E^2 = \varepsilon_r \varepsilon_o \frac{V}{t_{elastomer-act}^2} = -t_{3act} \quad (59)$$

The thickness of the elastomer film in the activated configuration can be described and is related to the original thickness.

$$t_{elastomer_{act}} = \lambda_{3_{act}} \cdot t_{elastomer_{non-act}} = \left( \frac{1}{\lambda_1^2} - k \right) \cdot t_{elastomer_{non-act}} \quad (60)$$

Since the relationship of the geometry of the helicoid and the relationship of hyperelastic material properties were determined, design parameters and envelopes were determined. Since the objective of the research was to make a 3D printable model design parameters were set based under the consideration. The geometric structure of a helical dielectric elastomer consists two compliant electrode layers that sandwich the elastomer layers. In order to prevent short circuiting from occurring, the electrodes will be designed with a slightly shorter radius than the elastomers. Therefore, the single external and internal radius of the helicoid will be considered as a design parameter [10, 12, 13, 50].

Another geometric parameter of interest will be the thickness of the elastomer and electrode layers. Due to the fact this paper is based off additive manufacturing, the thickness of the electrode is fixed at 50 micrometers due to printer constraints of nScript's SmartPump™. The nScript's SmartPump™ equipped with nTip™ has shown significant advantages over other methods in terms of their precise control, available materials, and printed material resolutions. For instance, nTip™ can print lines as small as 15 microns, accommodating a wide range of materials from 1 cP (centipoise) to over 1 million cP. Since the electrode thickness is fixed, the elastomer thickness will be taken into account as a design parameter. Another geometric parameter that needs to be considered will be the pitch angle of the helicoid. By altering the pitch angle, the distance between the layers will be altered, thus affecting the strain of the actuator. The dielectric constant of the elastomer is a material property that will identify the behavior of electric field of the actuator which will be another design parameter. The hyperelastic material constants based on Yeoh's equation that will identify the strain using Cauchy-Green

deformation tensor and range of material properties of silicon and silicon-based elastomers [10, 12, 13, 50].

#### 4.4.3 Design Envelope

The design envelope is a condition that needs to be satisfied in order to make the design feasible.

Geometric design parameters will be given a boundary that satisfies the additive manufacturing dimensions.

The design envelope was set based on the current state of silicon-based DEA material parameters that are widely

used in the industry for experimental purposes. A thorough research was done by Madsen on different materials that can be used for DEAs. The boundaries represent the design envelopes for the design parameter made to solve this problem.

Table 4.1 Design Envelope

Design parameter	Range and units
<i>External radius</i>	2 - 5 (mm)
<i>Internal radius</i>	1 - 4 (mm)
<i>Pitch angle</i>	1 - 10 (degree)
<i>Elastomer thickness</i>	100 - 500 ( $\mu\text{m}$ )
<i>Dielectric constant</i>	2 - 10

#### 4.4.4 Optimization Method – Genetic Algorithm

As described, the objective was to optimize the geometric parameters based upon the design envelope that is suggested above. For optimization, a genetic algorithm (GA) was used. A genetic algorithm (GA) optimization process was used to minimize the actuation voltage while maximizing the actuation strain based on the design parameters and their envelopes. The GA process starts by randomly setting an initial population

which represents random sets of possible solutions within a fixed design space. Each individual can be represented as a collection of design variables which in genetics can be described by strings of genes called chromosomes. An objective function is formulated as a measure of the “fitness” of the individuals within the prescribed environment. This fitness function depends on the design parameters and is evaluated for each individual within the population. Each design parameter is constrained by lower and upper bounds allowing the optimal results to be set within a desired range. A set of algorithm parameters are defined, determined to affect the performance of the optimization process. These parameters include the population size, the probability of cross-over, the probability of mutation, and others. The process of GA is an iterative approach where each iteration represents a new generation. In order to improve the fitness of the individuals in the population in subsequent generations, selection, mating, cross-over, and mutation operators are applied over the population to form the offspring that will constitute the new generation.

The selection operator will first choose individuals based on their fitness. The mating process takes place between two selected individuals whose genetic material is combined through a cross-over of their chromosomes to produce an offspring. During this process, mutation operators are implemented to randomly affect the resulting offspring chromosome. The individual with the best fitness in a generation survives (or is cloned) into the next generation. This process continues until a predefined maximum fitness is attained or a maximum number of generations is reached.

GA can be used for single objective optimization as well as multi-objective optimization problems. The difference in the GA application for single objective and

multi-objective optimization lies within the evaluation method. For single objective functions, the fitness function is simply the inverse of the objective function. Single objective optimization leads to an optimal solution within the design space. In multi-objective optimization, the rationale consists on assigning a rank to each individual based on its dominance by the other individuals in the same generation. The non-dominated sorting approach can be also applied to ranking fronts of individuals instead of single individuals where the rank of each front is determined based on its dominance by other fronts.

$$Fitness(i) = \frac{Number\ of\ individuals - rank(i) + 1}{\sum_{j=1}^{Number\ of\ individuals} (Number\ of\ individuals - rank(j) + 1)} \quad (61)$$

Equation 61 demonstrates the multi-objective optimization fitness value expression for an individual  $i$  at a given generation consisting the set number of individuals. Eventually, the optimization will lead to a frontier of individuals in the optimization space that represents the lowest combination of objective function values. This frontier is known as the Pareto front and the values along the Pareto front will have a rank of 1. The positive aspect of Pareto front is that it allows to choose among a series of optimal solutions based on the feasibility of their optimization parameters and also allows compromise between the different objectives. The non-dominated sorting genetic algorithm (NSGA) approach for individuals will be used to solve for the bi-objective optimization function problem in this paper. With two objective functions involving 5 different optimization parameters, the goal of this optimization is to maximize the strain while minimizing the voltage.

The key concept behind NSGA is a non-dominated sorting of the population and a crowding distance. This algorithm uses the elite preserving operator, which grants an

opportunity for the elitist of a population to be directly carried over to the next generation. The algorithm for NSGA is shown below [28, 29, 50].

- A fitness function is chosen to represent the problems, selection operator, a crossover operator and a mutation operator.
- Population size, crossover probability, and mutation probability are selected.
- Random population of strings is initialized for the first generation ( $t_{\text{initial}}=0$ ).
- Evaluate each string in the population.
- If  $t > t_{\text{max}}$  or other termination criteria is satisfied, then terminate.
- Pre-perform reproduction on the population.
- Perform crossover on random pairs of strings.
- Perform mutation on every string.
- Evaluate strings in the new population. Set  $t = t_{\text{initial}} + 1$  and repeat process from step 5.

In the present work, objectives are to minimize the voltage and to maximize the strain. Since objective functions are contradictory in nature and genetic algorithm leads the minimizing behavior, some modification is needed for the strain objective function. The voltage objective function will remain as is while the strain objective function will be inverted and minimized simultaneously. The fitness functions for each NSGA are determined. These functions are maximized simultaneously using the combined fitness in NSGA-II. Pareto front, the most optimal response at different optimal settings were determined. The parametric equation 62 is shown as a combination of these objectives with a weight  $w$ . The first function describes the voltage while the second function describes the strain.

$$\begin{aligned}
 &f(x_1, x_2, x_3, x_4, x_5) \\
 &= wf_1(x_1, x_2, x_3, x_4, x_5) + (1 - w)f_2(x_1, x_2, x_3, x_4, x_5) \quad (62)
 \end{aligned}$$

#### 4.4.5 Results

The objective of optimization is to minimize the actuation voltage while maximizing the actuation strain of the HDEA. Variation of actuation voltage and actuation strain is plotted as shown in Figure 3.12. This figure shows the Pareto front for the optimal response at different optimal design parameter settings. Since optimal design parameter settings for optimization was selected according to the material properties of silicon-based DEAs that have been previously investigated, it is crucial to select optimal design parameter for available solutions in Pareto front.

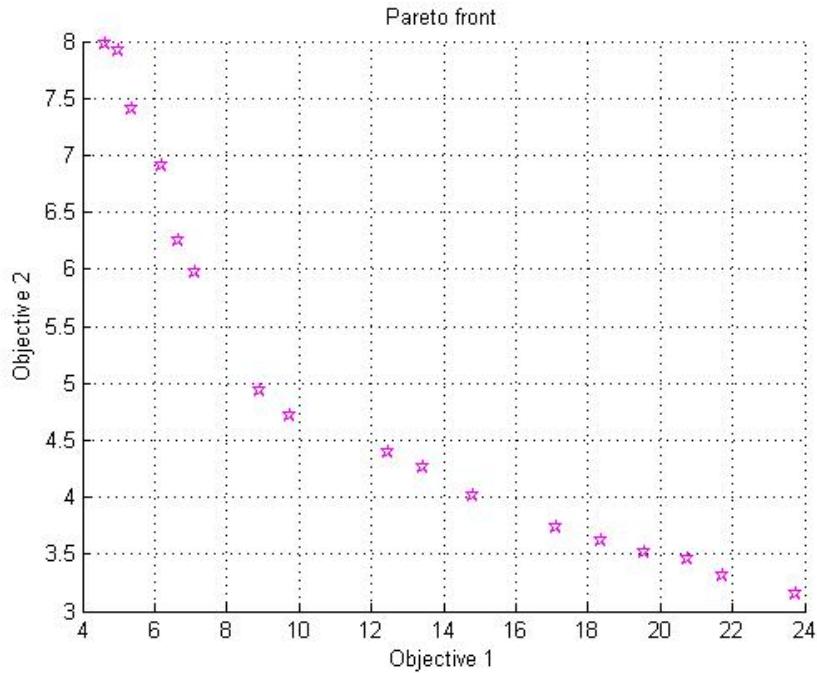


Figure 4.12 The Pareto Front for the multi-objective function. Objective 1 is voltage while objective 2 is the inverse of strain.

Table 4.2 Optimal combination of parameters in HDEA.

Voltage (kV)	Contracted displacement ( $\mu\text{m}$ )	Thickness ( $\mu\text{m}$ )	$\epsilon_r$	$R_o$ (mm)	$R_i$ (mm)
8.902528	20.2	139.3	6.954	3.450	2.210

Table 3.2 shows the optimized voltage and displacement values along with the corresponding optimal combination of parameters. From optimization, the minimum value of 8.9 kV actuation voltage corresponded to 14.5% strain where the thickness of the elastomer, dielectric constant, external radius and internal radius were 139  $\mu\text{m}$ , 6.9, 345  $\mu\text{m}$ , and 221  $\mu\text{m}$ . Poulin's paper on 3D printed DEA with an actuation voltage of 300 V provides a good indication of how these parameters falls within the region of optimization. Based on Figure 3.13 of Poulin's paper [18] on circular DEA where different membrane thickness circular DEAs were 3D printed, the breakdown voltage and the percent strain per actuation voltage depended on the thickness of elastomer.

As the thickness of the elastomer increased the voltage increased so as the dielectric breakdown. From the following information, with elastomer thickness of 139  $\mu\text{m}$ , actuation voltage of 8.9 kV seems to be reasonable and the dielectric breakdown satisfies the operational range. This shows that if the elastomer thickness can be reduced, the actuation voltage can be greatly reduced while compromising the amount of strain. Based on the optimized parameters as well as Poulin's paper, a numerical model of HDEA was made on Abaqus to test the performance of the HDEA and to see whether the deformation parameters were similar to the actuation that is stated above. In previous work, numerical studies were done based on Neo-Hookean material properties as well as



different geometric boundaries and VHB 4910 as its material. In this numerical analysis, a new model was created based on the optimized parameters.

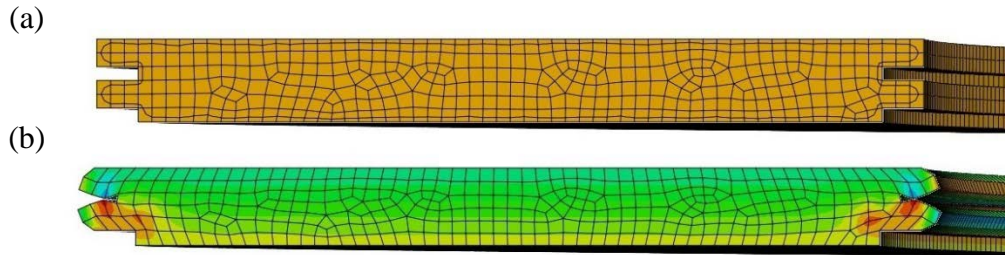


Figure 4.13 Optimized HDEA before (a) and after (b) actuation. The bottom electrode was fixed and the pressure was applied on the electrode section based on the positive and negative charge direction to implement compression of the elastomer layers.

Based on the simulation, the amount of actuation achieved by the corresponding parameters was identical. In ABAQUS simulation, the values were based on mm scale rather than meter scale. As a result, 24.9  $\mu\text{m}$  of deformation occurred while in the optimized calculation 20.2  $\mu\text{m}$  was achieved. There is an approximately 15% error between numerical approximations compared to the analytical solution derived from optimized parameters.

#### 4.5 Feasibility to 3D print HDEA and alternative methods

Since the optimization was based upon consideration of 3D printing, studies on different types of materials and 3D printing method were investigated. Typical DEAs have an elastomer membrane that is 20 ~ 100  $\mu\text{m}$  since the fabrication of elastomer membrane that is thinner than the values is challenging to fabricate and the membrane quality and uniformity degrades. The actuation voltage of DEAs can typically be reduced by optimizing the material parameters of the elastomer membrane or by reducing the thickness. The material properties of hyperelasticity and dielectric constant can be

engineered by addition of different types of silicon fillers. Recently some good materials with high dielectric constants have been developed which makes this option more feasible.

Due to the complex geometry of the helicoid, the 3D printing process of the helical dielectric elastomer was investigated and different approaches to 3D print the HDEA was thought. 3D printing DEA itself faces multiple challenges thus 3D printing a complex helical shape provides more challenges. While investigating different options to 3D print helical structures, the concept of spiral pleat was introduced. There has been a long study on how to effectively fold a helicoid in origami and it is called spiral pleat origami. By adopting the concept of how the spiral pleat works, a helicoid can be divided into multiple right angle triangles. The single layer helicoid can be divided into small grid elements. The methodology to print the HDEA is to print each element of the grid one at a time before advancing to the other. Unlike printing the structure layer by layer depending on the elastomer or electrode, HDEA will be printed based on each grid, printing the elastomer and the electrode layer at the same time. For HDEA, the trapezoidal shape grid along the helicoid axis will be used as a grid element for the manufacturing process.

This brought in a new perspective of designing an actuator that is capable of meeting the requirements of artificial muscle. The helical DEA fabrication came down as an obstacle so new geometrical configuration was to be investigated. Since the shape of the spiral pleat provided an inspiration for active origami structures, helically arranges origami structures were studied.

## **Chapter 5. Origami Dielectric Elastomer Actuator**

### **5.1 Origin of Origami**

Origami originated from the term of Japanese art of folding paper, “ori-kami”. Traditional origami utilizes a single sheet of planar paper with no cuts, no gluing, and no tearing that is then manipulated and folded into certain shapes. Over the past couple of decades, studies on geometrical aspects of origami and development of practical application, as well as new structures and devices inspired by origami, have greatly progressed due to the growing interest of mathematicians and engineers. As the majority of the sheet materials used in engineering applications has been relatively rigid in comparison to paper, most studies have been drawn to rigid active origami where pre-determined creases allow continuous motion between the folding elements. Also, the mechanical model of a flat sheet of paper can be generally related to the sheet material membrane, with the characteristics of no bending stiffness and a high stretching stiffness where the transformations rely on minimal energy movement for bending. The folding linkage is called the ‘crease’ and is considered as a hinge in the model that was studied. The rigid region between the creases is restricted from bending or deformation while folding. The crease, which is a fold, can either be a convex or a concave shape. In origami, we describe the convex fold as a mountain and concave fold as a valley. A crease pattern is made by altering different combinations of crease.

Since helical shapes of origami were being studied, buckled origami pattern that was continuous was brought up. Among different crease patterns and tessellations, Kresling pattern was a continuous pattern of zigzag trapezoids that was able to form a structure capable of large deformation and strain.

## 5.2 Kresling Pattern Origami Spiral Box Pleat Actuator

The Kresling pattern, named after Biruta Kresling, describes a specific buckled pattern under torsional load. Kresling proposed that the essence of buckling is not a failure of material but a model from nature that can be understood and designed for engineering applications. A pleat is one of the most common, versatile and easy to use folding techniques [32, 33, 34]. There are multiple types of pleats; accordion, knife, incremental, box and spiral pleat. Combining the spiral pleat with the Kresling pattern can result in box spirals. The pattern can be drawn in one continuous zigzag line, where the strips of trapeziums are divided by equally spaced mountain folds then sloping parallel valley folds placed diagonally between the mountain folds to connect them.

In this paper, the Kresling pattern is used to form a box spiral. The box spiral creates overlapping of plane, which visually resembles an hourglass. The angle of the sloping valley fold is crucial in determining the shape of the box spiral. By making the angle large, the box will be tall; if the angle is small, the box will be flat. The Kresling pattern spiral box pleat is designed using Autodesk Fusion 360. The model is made under the assumption that it can be 3D printed. In order to allow folds, a living hinge is implemented within the design of the Kresling pattern spiral box pleat. A living hinge is a flexible hinge made from the same materials as the rigid piece that is connected to. These living hinges are cut or thinned to allow the bending of the rigid pieces like a hinge system. The idea of the living hinge is inspired by the idea of kerf cutting for wood in carpeting. To bend the wood, carpenters use kerf cuts to bend wood to create an arced wooden structure. For our application, we will have thick and thin regions along with the

inactive layer, which will determine the range of folding. Combining the Kresling pattern spiral box pleat with the living hinge allows sheet materials to fold in a similar behavior of a paper [32, 33, 34].

In order to actively fold the Kresling pattern spiral box pleat, the use of smart materials is investigated as a method to fold and unfold the origami structure. Among all smart materials, dielectric elastomer (DE) is investigated and used as an actuator to fold and unfold the origami structure. DEs are compliant materials that are very promising due to high actuation strain and high energy density. The working principle of dielectric elastomer actuator (DEA) is a compliant capacitor where soft elastomer film is sandwiched between the two compliant electrode layers of opposite charge. By applying voltage, the electrode layers of opposite charge contracts due to the electrostatic forces and the DE experience reduction in the thickness direction while expanding along the planar direction due to incompressibility. The electrostatic pressure across the electrode is given by the Maxwell stress. The Maxwell stress acting on the elastomer can be calculated when given applied voltage, film thickness, and dielectric constant of the material by equation 33. Contraction of DE in the thickness direction is the fundamental principle mechanism for in plane motion, which can be used for actuation purpose for different actuator configurations. As a numerical study, we focused on using the conventional VHB 4910/4905 tape that is widely used as dielectric elastomer substrates. There have been different configurations of DEAs that have been developed, such as stacked DEA, helical DEA, folded DEA, disk DEA, and other configurations. In the origami structure, stacked DEA will be used since it is best suited for this application involving sheet alike structures.

Prior to numerical analysis, geometrical modeling of spiral box pleat using Kresling pattern was investigated. Kresling pattern is a naturally occurring pattern that a thin walled sheet is wrapped around two coaxial mandrels while leaving a gap between the two. When the mandrels buckle under torsion as well as axial compression, a folding pattern appears that is known as the Kresling pattern. Since the folding pattern was developed by the use of force under natural circumstances, pure physics is able to unfold within the Kresling pattern system with minimum energy [32, 33, 34].

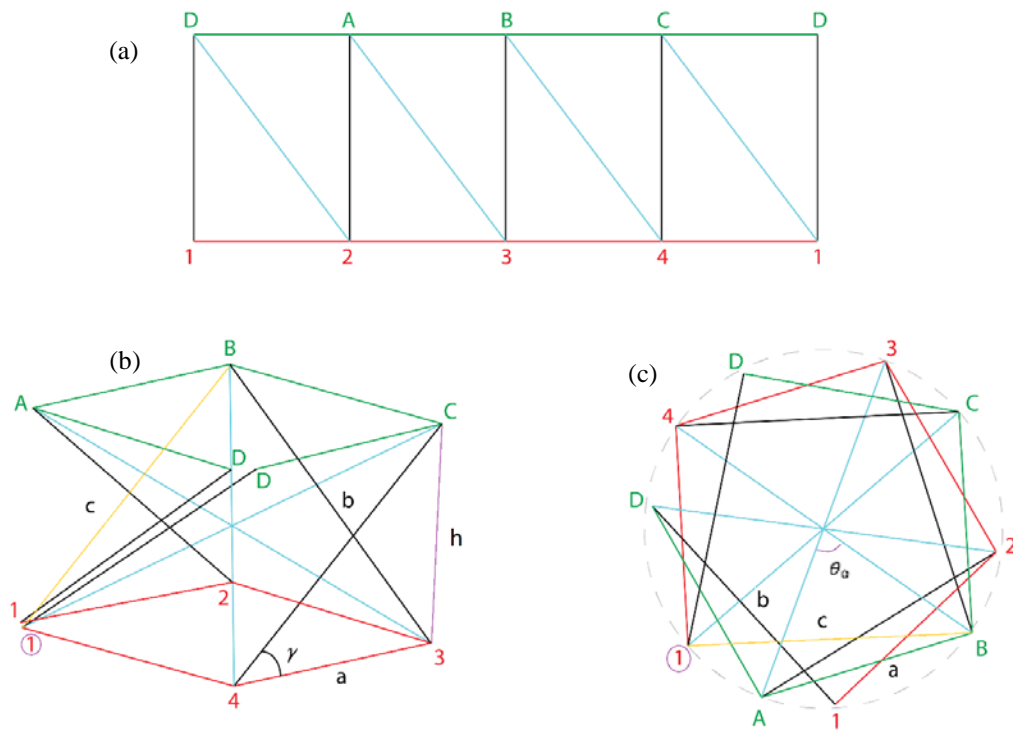


Figure 5.1 (a) Crease pattern of spiral box pleat, (b) fully folded configuration, (c) fully deployed configuration.

Kresling pattern is a pattern made from trapeziums that are divided by equally spaced crease patterns of mountain folds and sloping parallel valley folds placed diagonally between the mountain folds connecting them, see Figure 4.1 (a). Folding

Kresling pattern generates two types of deformations that are known as crease bending and facet bending. In this paper, we design a mathematical model of the structure by studying the crease lines of the origami pattern in which the crease lines are folded by using dielectric elastomer actuators. The alternating mountain folds and valley folds provide the Kresling origami cells to behave like springs, transforming its shape from a hexagon-alike shape into a square shape as it deforms along the height direction. Based on the crease folds, potential energy under external force and torque can be derived [11, 15, 18, 19]. Then by using the principle of minimum potential energy, we can obtain the relationships of external force with displacement along the height.

### 5.2.1 Establishing Geometrical Relationship of Spiral Pleat Box

In order to express the motion of the Kresling spiral box pleat, axial motion and rotational motion are expressed using the height of the spiral box pleat  $h$  and the relative twist (offset) angle  $\theta$ . The height  $h$  is defined as the distance between the top surface ABCD and surface 1234 in Figure 3.14 (b). The relative twist angle is defined as the angle  $\theta$  between the center point of 12 and point C,

$$h = h_0 - \Delta h ; \theta = \theta_0 - \Delta\theta \quad (63)$$

where  $h_0$  and  $\theta_0$  are initial height and initial relative twist angle and  $\Delta h$  and  $\Delta\theta$  are axial and rotational displacements. From the length of elements of b and c in Figure 3.14 (b), we derive the equations to express b and c in terms of displacement  $\Delta h$  and rotational angle  $\Delta\theta$  in order to calculate the elastic energy with respect to deformation. From Figure 3.14 (b), we can develop the following equations,

$$\overline{1D}^2 + h^2 = b^2 = R \sin\left(\theta - \frac{\pi}{4}\right) ; \overline{1B}^2 + h^2 = c^2 = R \sin\left(\theta + \frac{\pi}{4}\right) \quad (64)$$

where  $\overline{1D}$  and  $\overline{1B}$  are line elements between point 1 and point D, and point 1 and point B.

Based on the geometry from Figure 3.14 (b),  $\overline{1D}$  and  $\overline{1B}$  can be shown by the following equation.  $R$  is the radius of the circumscribing circle that fits the spiral box pleat structure. From equation 64, we can derive the following.

$$b^2 = h^2 + \left[ R \sin\left(\theta - \frac{\pi}{4}\right) \right]^2 ; c^2 = h^2 + \left[ R \sin\left(\theta + \frac{\pi}{4}\right) \right]^2 \quad (65)$$

However, we can identify that the length  $a$  and  $b$  do not change as deformation occurs. Therefore, term  $c$  is being used to model the relationship of the spiral box pleat. By substituting equation 64 to equation 65,

$$c = \sqrt{(h_0 - \Delta h)^2 + \left[ R \sin\left((\theta_0 - \Delta\theta) + \frac{\pi}{4}\right) \right]^2} \quad (66)$$

The following equation demonstrates the deformation of the Kresling spiral box pleat structure that involves changes in axial and rotational motion. The linear elastic strain can be investigated by the following equation.

$$\varepsilon = \frac{c - c_0}{c_0} \quad (67)$$

Then we can find the dimensionless strain energy of the unit length as,

$$w = \frac{W}{E} = \frac{1}{2} \varepsilon^2 \quad (68)$$

where  $E$  is Young's Modulus of the material of the active layer (silicone: 0.001 GPa).

In order to examine the entire behavior of the spiral box pleat, minimum potential energy is used to determine the axial force, torque, deformation in axial and rotational motion. In previous literature studies on water bomb origami configurations that inhibit



bi-stable behavior, they have used the material spring constant  $k$  to couple the behavior of the origami structure. Based on the equation of bi-stable origami structure, the potential energy is calculated by the difference between elastic energy along element  $c$  and work done by the external force and the torque. Elastic energy and work can be defined as the following,

$$U = \frac{1}{2}k(c - c_0)^2 ; W = F\Delta h + T\Delta\theta \quad (69)$$

where  $k$  is the spring constant of element  $c$  where  $c_0$  is the initial length of  $c$ . By combining the equation 69, potential energy can be determined,

$$P.E = U - W = \frac{1}{2}k(c - c_0)^2 - F\Delta h - T\Delta\theta \quad (70)$$

The minimum potential energy can be described by the following equation:

$$\Delta(U - W) = \Delta P.E = 0 \quad (71)$$

The function of potential energy is a function of  $\Delta h$  and  $\Delta\theta$ , by substituting equations 69, 70, and 71, the equation can be rewritten as the following,

$$\begin{aligned} \frac{\partial P.E}{\partial \Delta h} &= -k(h_0 - \Delta h) \left(1 - \frac{c_0}{c}\right) - F = 0 \\ \frac{\partial P.E}{\partial \Delta\theta} &= R^2k \left(\frac{\pi}{4} + \theta_0 + \Delta\theta\right) \left(1 - \frac{c_0}{c}\right) - T = 0 \end{aligned} \quad (72)$$

By solving the two equations above, we can obtain the relationship between the axial and torsional motion. FEA was conducted to verify the results of analytical solutions. One side of the spiral box pleat inhibits an over and under configuration, which allows the spiral box to act as a spring. This allows the origami structure to behave like a

spring when force is exerted. Therefore, the last cell that is the 4th cell of a single layer spiral box pleat inhibits a complex geometry. For this reason, the last cell is treated the same as the other three cells that are used for static analysis. In addition, the assumption of spring constant  $k$  of silicone rubber ( $k=17$ ) was used for the static analysis.

Table 5.1 Parameters for static analysis

Parameters	value	Parameters	value
Initial height $h_0$ (inch)	1.65	Cell height (inch)	2.75
Initial angle $\theta_0$	45	Thickness (inch)	0.02
Cell width $a$ (inch)	2.125	Spring constant $k$	17

Based on the parameters shown in Table 4.1 the results in Figure 4.2 were obtained.

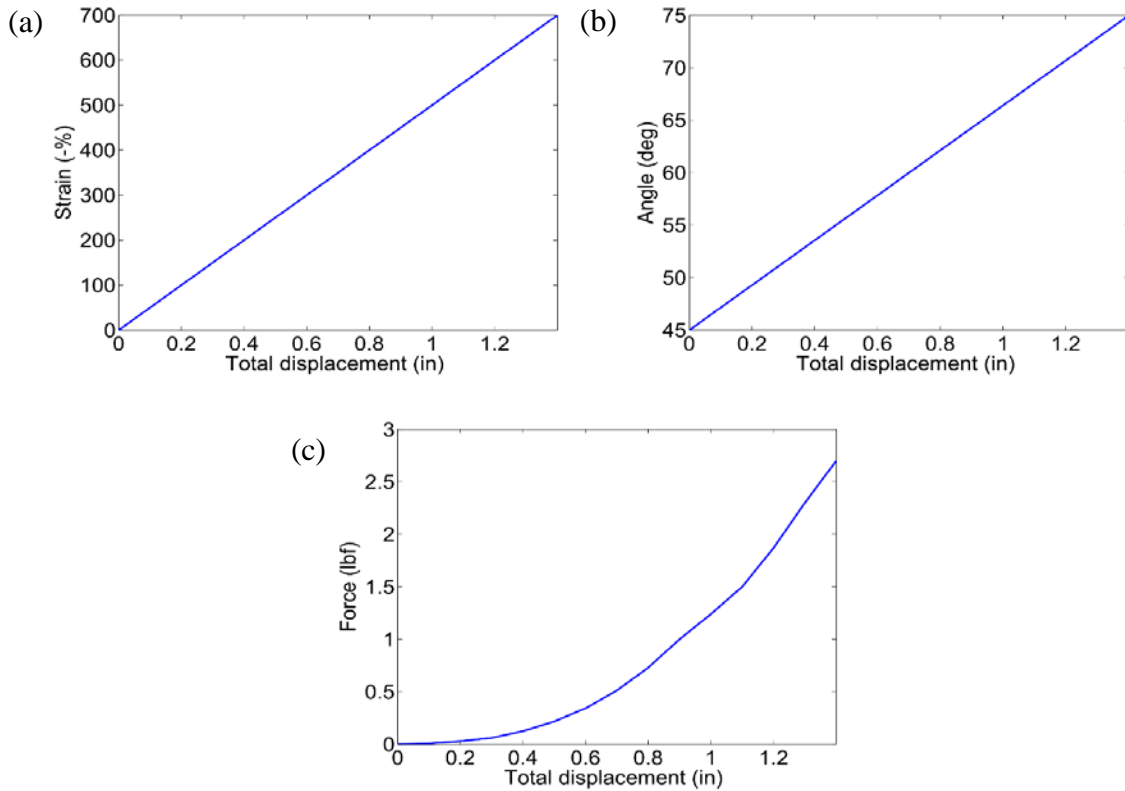


Figure 5.2 (a) Strain displacement graph, (b) angle displacement graph, and (c) force displacement graph

As shown in Figure 4.2 (a), due to the nature of the origami structure of the Kresling spiral pleat, deformation achievable by the structure is approximately 700%. The structure undergoes about 30 degrees' deformation while collapsing to its non-deployed state. The amount of force that was required to collapse the structure from its deployed state to non-deployed state is shown in Figure 4.2 (c). Based on the amount of force required to collapse the structure, we can identify the strength that is required by the dielectric elastomer actuator (DEA) to fold the origami structure.

### 5.2.2 Stacked Dielectric Elastomer Actuators for Folding

Dielectric elastomer actuators (DEAs) are elastomeric mechanical transducers that are capable of converting electrical energy to mechanical energy. By applying a high DC voltage on the compliant electrodes that sandwich the dielectric elastomer membranes, the dielectric elastomer collapses in thickness direction while expanding along the planar direction. Based on the assumption of constant volume Maxwell tensor or electrostatic pressure, we can obtain the following equation, where  $\epsilon_0$  is the permittivity of free space,  $\epsilon_r$  is the permittivity of the dielectric material,  $V$  is the voltage applied and  $d$  is the gap between the electrodes or thickness of the elastomer membrane.

$$U = \frac{1}{2} \epsilon_0 \epsilon_r \frac{V^2}{d^2} \quad (73)$$

As mentioned above high voltage requirement is a major challenge that is associated with DEA applications. In recent studies, researches were conducted to reduce the gap between the compliant electrodes. By reducing the thickness of the elastomer membrane, voltage requirements can be significantly decreased. Based on recent studies,

researchers fabricated  $3\mu\text{m}$  dielectric film and lowered the actuation voltage to 300 V. By stacking thin layers of dielectric films, large deformation along with lower actuation voltage can be obtained. For the Kresling spiral box pleat, the shape works best when the thickness of the structure is minimal. Dielectric elastomer has been investigated as a viable option for active material application due to lightweight, the capability of large strains, high specific energy density, and flexibility. Most commonly studied DEs are VHB 4910 and VHB 4905 that are produced by 3M, however, recent studies show that silicone can be used as well for DE fabrication.

As mentioned, the objective is to validate the force required to actuate the folded/bending region of the Kresling spiral box pleat using dielectric elastomer actuator. Therefore, the stacked bending dielectric elastomer actuator is used to achieve the folding behavior for the origami structure. The dielectric elastomer actuator that is used for the study is identical to that of bending actuators. However, in order to fold, the inactive (passive) layers of the DEA serves a different purpose. By having a combination of the thick layer (blue arrow) and the thin layer (red dot arrow) passive layer shown in Figure 4.3 (a), results can allow the bending curvature to increase. Where the passive layer is the thinnest, larger bending will occur. Figure 4.3 (a) and 4.3 (b) demonstrates the structure of the inactive layer and the active layers at rest and when voltage is applied.

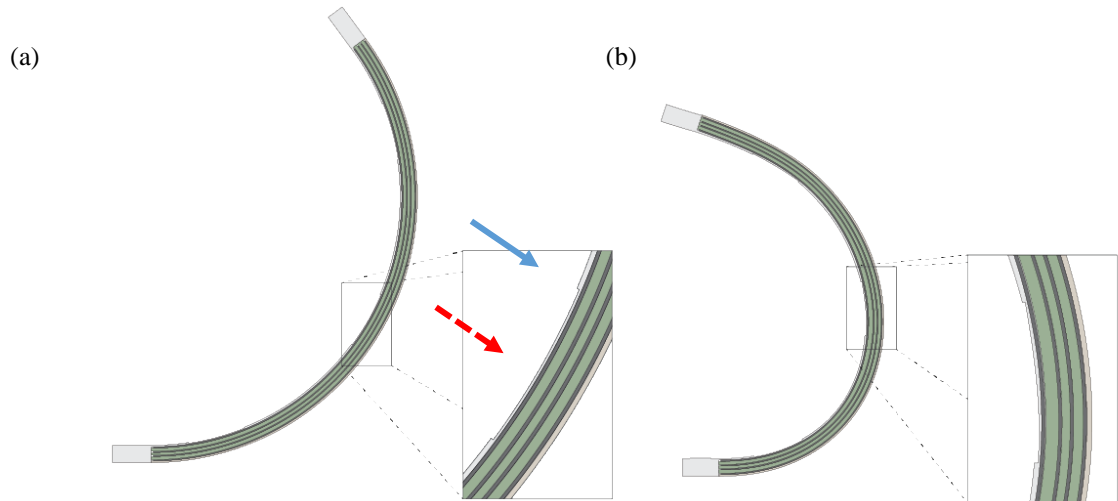


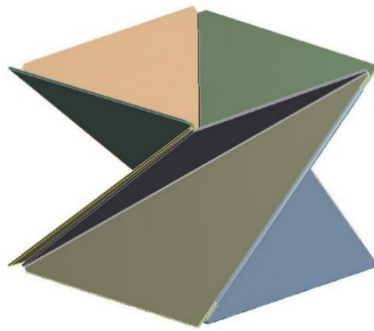
Figure 5.3 Structure of the stacked folding DEA along the folding region. (a) PETG thick and thin layer are used as inactive layer to maximize the folding motion and (b) voltage is applied and folding happens in the thin inactive layer regions.

Finite element analysis (FEA) on the dielectric elastomer actuator is conducted to validate the performance of the actuator and the origami structure. The FEA on the DEA allows us to determine the actuation voltage to achieve ideal bending. This also allows us to determine how much force is required to actuate the origami structure. The finite element analysis on the origami structure enables the determination of how much force is required to collapse the structure. For this analysis static FEA was conducted with probes on ANSYS to measure the actuation force of the spiral box pleat.

A single cell of Kresling pattern, shown in Figure 4.4 (a), is modeled and analyzed first to compare the behavior of single and multi-cell structures as well as to investigate the effects of boundary conditions. The same geometry and material properties are used for the analytical solution; however, the hinges are modeled as solid silicone bodies to reduce mesh size and computational time. This simplification is appropriate, as the main goal is to numerically estimate the required actuation force. While a vertical displacement of 1.4 inches is applied to four top edges of the single cell

Kresling pattern and the bottom edges are constrained along the same direction, the required actuation force is measured with reaction probe tool. The folded origami structure and its actuation force profile are shown in Figure 4.4 (b) and Figure 4.5, respectively. In Figure 4.4 (b), the top and bottom faces with boundary conditions applied on are marked in red.

(a)



(b)

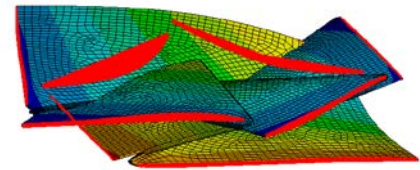


Figure 5.4 Single cell Kresling pattern model in (a) non-deformed and (b) deformed states.

As can be seen in Figure 4.5 the numerically obtained actuation force profile exhibits linear behavior and is very similar to the analytical result without the spring constant  $k$ . Firstly, it validates the mathematical model used in the simulation, particularly the boundary conditions chosen for the bottom edges of the pattern. Secondly, the linear trend of the numerical result is also expected as there are no non-linearity sources, e.g. material properties or geometry, and it can be verified that the mathematical model is solved correctly.

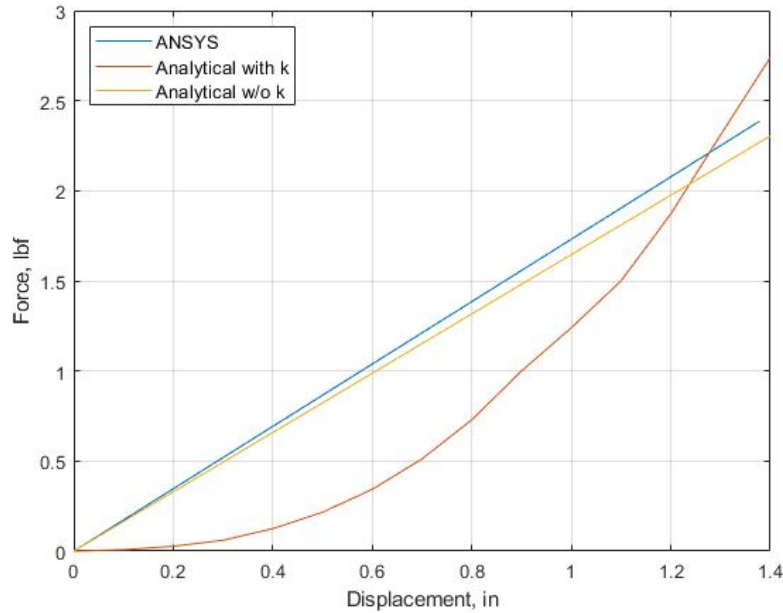


Figure 5.5 Actuation force profiles of the single cell Kresling pattern.

It is worth noting that the deformation of the Kresling pattern happens primarily due to the rotation of plates about flexible hinges. When modulus of elasticity of the hinge materials is lowered half, from 100 MPa to 50 MPa, the stiffness of the structure reduces about 30%. Thus, material mechanical properties for the hinge and its design are crucial for the overall origami actuator performance.

In order to obtain a more realistic simulation of Kresling pattern mechanics, i.e. closer to the analytical solution with spring constant  $k$ , such features should be considered: “Large deflection” option to account for geometry non-linearity, contact between plates to prevent penetration, and possibly further improvement of boundary conditions.

### 5.3 Results

The stacked dielectric elastomer hinge is shown in Figure 4.6. Three layers of dielectric elastomer were stacked as the active layers along with the compliant electrode.

The thickness of the elastomer membranes that were used for FEA is 50  $\mu\text{m}$ . The electrode layers were assumed to be 10  $\mu\text{m}$ . An additional elastomer layer was added as the outer most layer (15  $\mu\text{m}$ ). An inactive layer of PETG was added as the innermost layer. The thickness used for PETG membrane is categorized by the thin region with a thickness of 10  $\mu\text{m}$  and thick region with a thickness of 15  $\mu\text{m}$ . The entire thickness of the stacked dielectric hinge would be 220  $\mu\text{m}$ . The following parameters were converted to inches for FEA analysis. Figure 4.6 shows the composition of stack dielectric elastomer hinge for before and after activation with 4 kV source.

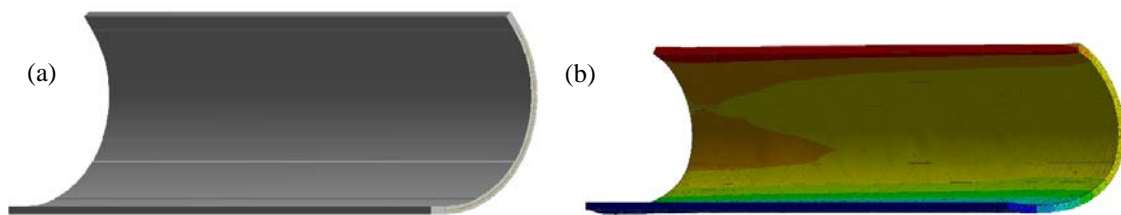


Figure 5.6 Stacked dielectric elastomer hinge (a) before deformation (0 kV) and (b) after deformation (4 kV); Isometric view of deformation along the length of the stacked DEA hinge.

For the FEA analysis, the material properties of 3M VHB 4910 were used where the values for the DEA material are shown in Table 4.2. The model was given a load of two uniform pressure having their magnitude equivalent to Maxwell stress present in equation 33. The pressure was applied to the electrode layers of the stacked DEA structure.



Table 5.2 DEA material parameters for VHB 4910 (Neo-Hookean)

Properties	values
$\epsilon_r$	4.7
$c_{10}$	2.5 e+5
$D_1$	8.0 e-7
G(MPa)	0.0737
K (MPa)	7.37

From Figure 4.7, the angle  $\gamma$  demonstrates the angle of the Kresling spiral box pleat structure at its initial state. As the origami structure collapse, the height of the structure reduces, thus the angle  $\gamma$  reduces in a linear relationship. When the Kresling spiral box pleat is upright without any actuation voltage, the angle  $\gamma$  is 54 degrees. When 4 kV is applied to the structure, the angle  $\gamma$  is reduced to 31 degrees. The initial height of the structure is 1.65 inches. Based on the change in gamma, approximately 0.7 inches of deformation in height was achieved. This provides that the Kresling spiral box pleat structure is capable of providing approximately 400% deformation.

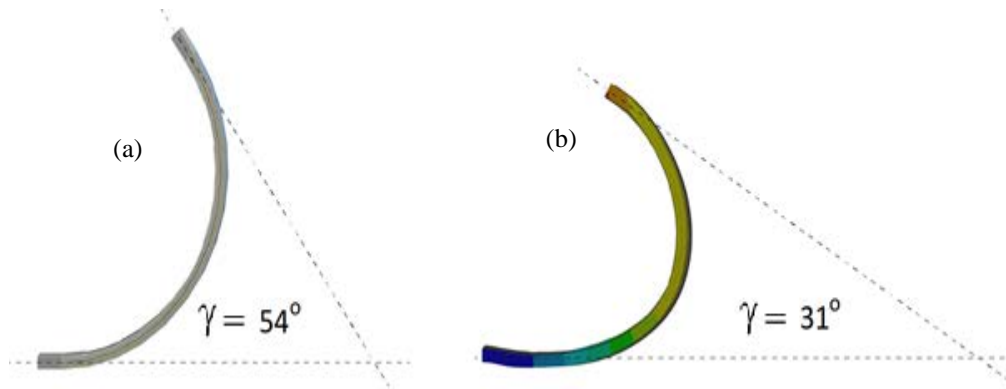


Figure 5.7 Angle gamma  $\gamma$  based on (a) before actuation and (b) after actuation voltage has been applied.

Another thing to consider is the block force applied to the PETG membranes. Despite the fact DEA is actuated by Maxwell's stress, the entire structure of the Kresling spiral box pleat is made from PETG sheets while the DEA operates the folding mechanism. As mentioned before PDMS (silicone) is used to bond them together since they create strong bonding. Based on the expansion of the DEA when the voltage is applied, block force was measured through FEA analysis. Applying 4 kV to the DEA active layer, a block force of 4.175 lbf was obtained. The force required to compress the structure falls in the range of 2-2.5 lbf. This result indicates that actuation through DEA active layers is capable for the Kresling spiral box pleat.

Figure 4.8 shows the direction of the expansion of the stacked DEAs. In Figure 4.8 (a), the stacked DEA is located behind the living hinge structure that is made with thin and thick layers as described in Figure 4.4. In Figure 4.8 (b), voltage is applied to the stacked DEA layers, this caused the expansion along the planar direction of the DEA. The PETG living hinge, which is the inactive layer makes the DEA bend along the desired direction. As the DEA expands along the planar direction to bend, it exerts force to the PETG inactive layer membrane. Figure 4.8 (c), the block force exerted to the PETG layer by the stacked DEA is measured using ANSYS.

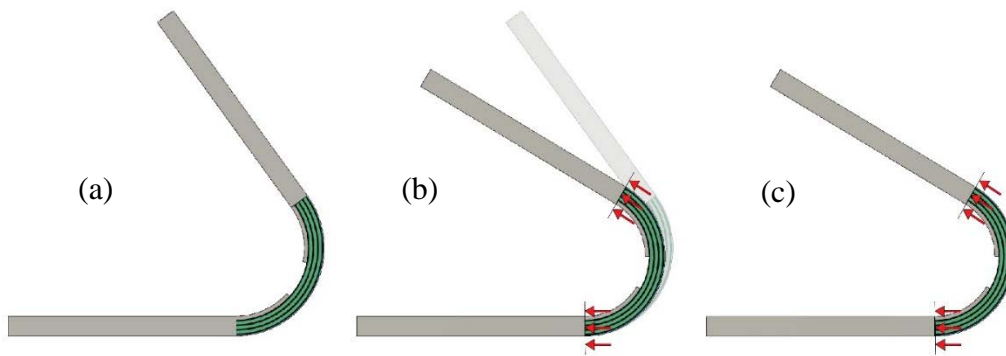


Figure 5.8 (a) The elastomer hinge and the (b) direction of DEAs expansion along the hinge with (c) block force.

Further analysis was done on lower voltages for 1 kV, 2 kV as well as 4 kV. At lower voltages, the amount of displacement can be shown in Figure 4.9 (a). Figure 4.9 (b) shows the change in angle depending on the applied voltage. Figure 4.9 (c) shows the block force that was exerted by the PETG membrane. Figure 4.10 shows the deformation of the stacked dielectric elastomer hinge at actuation voltage of 0 kV, 2 kV and 4 kV. Table 4.3 shows the amount of deformation in height, angle of the stacked DEA and the block force to the corresponding voltage.

Table 5.3 Deformation, angle and block force to the corresponding voltage

Voltage (kV)	0 kV	1 kV	2 kV	4 kV
Deformation (inches)	0	0.122	0.275	0.7027
Angle (degree)	54	50	45	31
Block force (lbf)	0	0.35	1.26	4.175

Based on the applied voltage, deformation, change in angle and block force changes exponentially as the voltage is applied. The results were produced by 3 layers of stacked DEA layers. By increasing the number of the stack of the DEA layers, larger deformation and block force can be obtained. Based on Kofod's paper, a single layer

DEA had a block force of 6 N. For 3 layers of stacked DEA, converting 4.175 lbf to Newtons, approximately 18 N of block force was achieved. Therefore, an optimization of the stacked DEA while allowing the origami structure to successfully fold should be studied in order to maximize the deformation while increasing the block force.

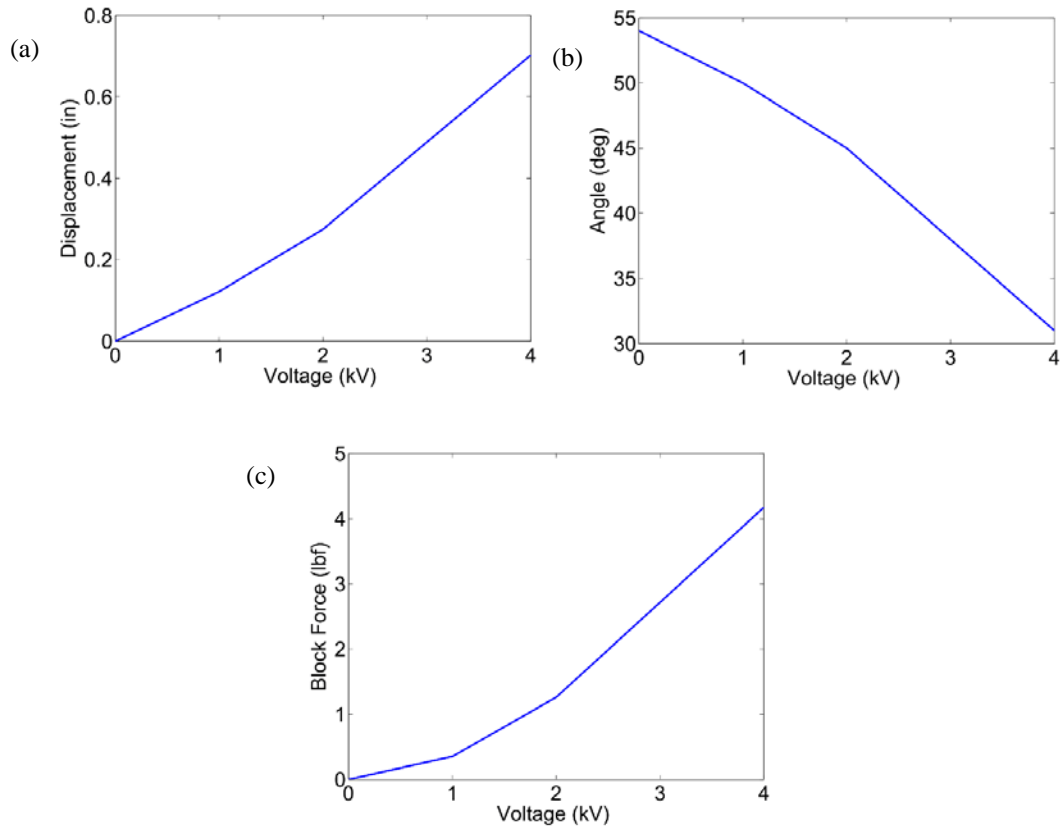


Figure 5.9 (a) Deformation of height, (b) change in angle, and (c) block force of the stack dielectric elastomer on the Kresling spiral box pleat.

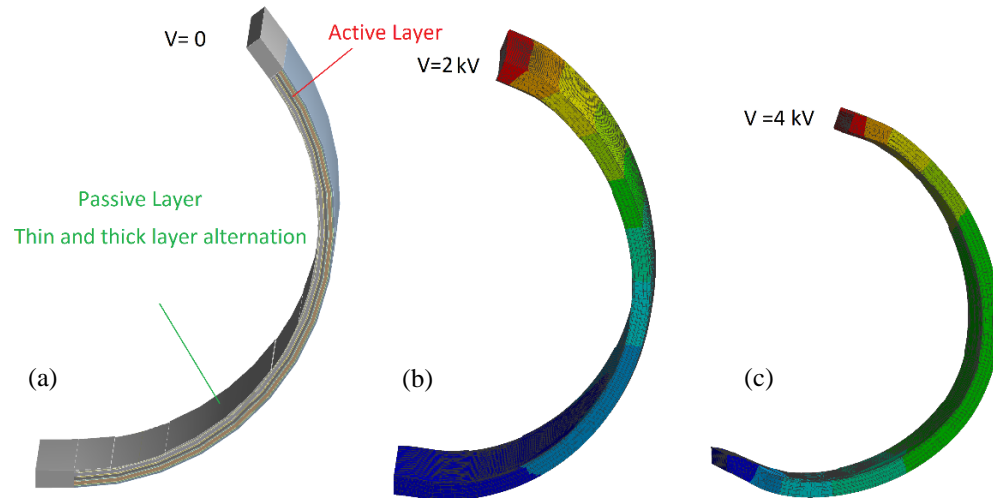


Figure 5.10 Deformation of the dielectric elastomer hinge with actuation voltage of (a)  $V = 0$  kV, (b)  $V = 2$  kV, (c)  $V = 4$  kV.

The results obtained from the finite element analysis (FEA) on the stack dielectric elastomer hinge shows the importance of having different thicknesses along the inactive layer. The stacked DEAs' primary deformation occurs on the region where the inactive layer is the thinnest. Therefore, the majority of the force is concentrated in this thin region. FEA shows that the location of the inactive layer effects the region of concentrated force and the force affects the behavior of the stacked DEA hinge. The DEA hinge shows that it can be actuated to grant the Kresling spiral box pleat and actuation strain of 400% considering the collapsed model being its initial thickness. The thickness of the collapsed model in our case would be the thickness of the layered structure. This demonstrated that with a small amount of actuation within the DEA allowed big deformation when accompanied with the origami structure.

## 5.4 Validation of Dielectric Elastomer for Origami Spiral Box Pleat Actuator

### 5.4.1 Hyperelastic Modeling

Before going in depth about the modeling for kinematic of origami folds and the dielectric origami actuator, several constitutive hyperelastic theories will be addressed. In order to validate the feasibility, Mooney-Rivlin, neo-Hookean, Ogden and Gent model were studied. The oldest model, the Mooney-Rivlin model was published in 1940 which contained two material parameters. In 1943, the neo-Hookean model was published with a single material parameter. The Ogden model was published in 1972 with 6 material parameters and the Gent model was developed in 1996 with 2 material parameters. These material properties were developed over time to improve and accurately portray the behavior of hyperelastic materials, more or so rubber.

The Mooney-Rivlin model was originally observed by Mooney that rubber response is linear under simple shear load. He considered  $W$ , strain energy function, as the following,

$$W = C_1(I_1 - 3) + C_2(I_2 - 3) \quad (74)$$

where  $C_1$  and  $C_2$  are material parameters. This model is widely used for rubber parts with less than 200% strain.

The neo-Hookean is the simplest form of constitutive equation for rubbers. It matches the Mooney-Rivlin model with only one parameter but was derived from molecular polymer chain network with statistics consideration which makes it a more physically based model. For the development of the strain energy function, Treloar used a Gaussian statistical distribution,

$$W = \frac{1}{2}nkT(I_1 - 3) = \frac{E}{6}(I_1 - 3) = C_1(I_1 - 3) = \frac{\mu}{2}(I_1 - 3) \quad (75)$$

where  $n$  is the chain density per unit of volume,  $k$  is Boltzmann constant and  $T$  is the absolute temperature. For a carbon black-filled natural rubber, which is similar to the case of DEA, Treloar obtained the three constants being 0.2 MPa. Two other forms were also developed where  $E$  is the Young's Modulus  $C_1$  being material constant and  $\mu$  being shear modulus. The neo-Hookean model is used for strain 50% or less.

The Ogden model derives the strain energy function through a series of real powers of the stretch ratio in their principal directions. The author proposes a 6 parameter model which shows excellent results for simple tension and equi-biaxial stretches. This model is used for large strain problems and is one of the most widely used methods despite the 6 parameter determination. The equation of the Ogden model is shown below.

$$W = \sum_{n=1}^N \frac{\mu_n}{\alpha_n} (\lambda_1^{\alpha_n} + \lambda_2^{\alpha_n} + \lambda_3^{\alpha_n} - 3) \quad (76)$$

The Gent model was proposed considering the general form of the Rivlin model based on empirical strain energy function that involves two material properties. However, the Gent model developed a concept of limiting the chain extensibility to consider that  $I_1$  should admit a maximum value  $I_m$  and proposed the following equation,

$$W = \frac{E}{6}(I_m - 3) \ln \left( 1 - \frac{I_1 - 3}{I_m - 3} \right) \quad (77)$$

where  $E$  and  $I_m$  are two material parameters. In addition, the approach of the model is compared with a physically based model of the Arruda and Boyce model, also known as 8 chain model, which shows a close resemblance.

These constitutive models have been developed over time and since some of the models have been developed more recent compared to the others, expectation of the newest model to demonstrate accurate curve fitting was assumed. Therefore, investigations on the performance of the different models were investigated through literature reviews. The results of the investigations were surprisingly not in the order of when the models were discovered. Based on the four constitutive hyperelastic models presented above, the Ogden model with 6 material parameters shown the best curve fitting performance. The Gent model showed the next best overall performance with 2 material parameters followed by the Mooney Rivlin model with 2 material parameters, and followed by the neo-Hookean model with 1 material parameter. Besides the models that were discussed above, the extended tube model with 4 material parameters has shown better performance than Ogden with 6 material parameters. In this paper, the four hyperelastic modeling methods were used to determine the theoretical and analytical results. This was compared to the numerical model, where the material parameters were obtained through experimental results that were obtained by other researchers. A comparison will be made among the 4 values and will be compared with the Gent model which only requires 2 parameters yet shows great performance in curve fitting based upon literature studies to determine how other hyperelastic method behaves.

#### **5.4.2 Ideal Dielectric Elastomer**

An ideal dielectric elastomer is a three-dimensional network of polymer chains that the true electric field relates to the true electric displacement. Material is considered



incompressible and the equation is justified by the terms of Maxwell stress [51, 54, 55, 56, 57].

The theory of dielectric elastomer by Suo [54] has been studied to develop an analytical model for this study. In this study, one side of the geometry would be constrained while the other side of geometry would be stretched to the desired length based upon the origami geometry. As mentioned in equation 33, DEA deforms according to the subjected electrostatic force.

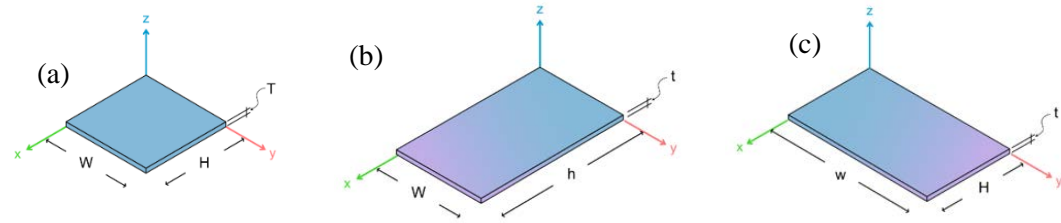


Figure 5.11 (a) Initial state of dielectric elastomer before actuation and (b, c) after actuation with deformed dimension. (b) is when  $W$  is constrained and (c) is when  $H$  is constrained.

In the initial state, where no pressure is applied, we have an initial length of elastomer width  $W$  and height  $H$  with initial thickness  $T$ , as shown in Figure 5.11 (a). In the deformed state, new elastomer dimension width  $w$  and height  $h$  are determined based on the fixed side  $W$  or  $H$  along with the thickness  $t$ . When  $H$  remains the same the  $W$  will be  $w$  and vice versa. Pressure  $P_w$  or  $P_h$  is applied based upon the direction of the stretch. Based upon the geometrical parameters, an equation of ideal dielectric elastomers determined by Suo [54] can be written as below,

$$\sigma_i + \varepsilon E^2 = \lambda_i \frac{\partial W_{stretch}(\lambda_1, \lambda_2)}{\partial \lambda_i} \quad (\text{where } i = 1, 2) \quad (78)$$

where  $\partial W_{stretch}(\lambda_1, \lambda_2)$  is Helmholtz free energy being expressed in terms of stretch ratio  $(\lambda_{1,2})$ . By combining applied stress  $\sigma_1$  and  $\sigma_2$  along with electrostatic stress  $\varepsilon E^2$ , also known as Maxwell stress, demonstrates the equation of elasticity of the elastomer.

Table 5.4 Hyperelastic model equations for the 4 different models

<b>Model</b>	<b>Equations</b>
<b>Mooney-Rivlin</b>	$C_{10}(I_1 - 3) + C_{01}(I_2 - 3) = \frac{\mu}{2}(I_1 - 3) - \frac{\mu}{2}(I_1 - 3)$
<b>Neo-Hookean</b>	$\frac{E}{6}(I_1 - 3) = C_1(I_1 - 3) = \frac{\mu}{2}(I_1 - 3)$
<b>Ogden</b>	$\sum_{p=1}^N \frac{\mu_p}{\alpha_p} (\lambda_1^{\alpha_p} + \lambda_2^{\alpha_p} + \lambda_1^{\alpha_p} \lambda_2^{\alpha_p} - 3) \rightarrow \sigma_1$ $= \sum_{p=1}^N \mu_p \left( \lambda^{\alpha_p} - \lambda^{-\frac{1}{2}\alpha_p} \right)$
<b>Gent</b>	$-\frac{E}{6} J_m \ln \left[ 1 - \frac{I_1 - 3}{J_m} \right]$ $= -\frac{\mu}{2} J_m \log \left( 1 - \frac{\lambda_1^2 + \lambda_2^2 + \lambda_1^{-2} \lambda_2^{-2} - 3}{J_m} \right)$

Different hyperelastic models were used for comparison to determine the ideal modeling method for DEAs incorporated with stiffeners that are stretched in one direction and fixed on the other. Among developed hyperelastic models, Mooney Rivlin, Neo-Hookean, and Ogden model are used for the analytical and numerical purposes in this study. However, Suo [54] stated about how effective the Gent model portrays the

results compared to the experimental results. Thus, the analytical result of Gent model is also added in comparison with the other models.

In order to determine the ideal dielectric elastomer equation, the Gent model equation is taken into account to solve the analytical process. The same procedure can be applied to the other three models. By combining the strain energy function of Gent with the ideal dielectric elastomer equation, we can derive the following equation.

$$\sigma_i + \varepsilon E^2 = \frac{\mu(\lambda_i^2 - \lambda_1^{-2}\lambda_2^{-2})}{1 - (\lambda_1^2 + \lambda_2^2 + \lambda_1^{-2}\lambda_2^{-2} - 3)} \frac{1}{J_m} \quad (\text{where } i = 1,2) \quad (79)$$

Considering a case where one side is constrained and the other is stretched, i.e. uniaxial stretch, it leads to a situation similar to DEA being subjected to voltage through the thickness  $T$  and the stretch  $\lambda_{1,2}$  are both present. However, the stress in the fixed direction remains zero while the stretch direction stress is present. Based on these factors, the equation 78 and 79 can be rewritten as below,

$$\varepsilon E^2 = \varepsilon \left( \lambda_2 \lambda_2 \frac{V}{T} \right)^2 = \frac{\mu(\lambda_1^2 - \lambda_1^{-2}\lambda_2^{-2})}{1 - (\lambda_1^2 + \lambda_2^2 + \lambda_1^{-2}\lambda_2^{-2} - 3)} \frac{1}{J_m} \quad (\text{Fixed Side}) \quad (80)$$

$$\sigma_1 + \varepsilon E^2 = \lambda_1 \frac{P_x}{WT} + \varepsilon \left( \lambda_1 \lambda_2 \frac{V}{T} \right)^2 = \frac{\mu(\lambda_2^2 - \lambda_1^{-2}\lambda_2^{-2})}{1 - (\lambda_1^2 + \lambda_2^2 + \lambda_1^{-2}\lambda_2^{-2} - 3)} \frac{1}{J_m} \quad (81)$$

$$\sigma_2 + \varepsilon E^2 = \lambda_2 \frac{P_y}{HT} + \varepsilon \left( \lambda_1 \lambda_2 \frac{V}{T} \right)^2 = \frac{\mu(\lambda_2^2 - \lambda_1^{-2}\lambda_2^{-2})}{1 - (\lambda_1^2 + \lambda_2^2 + \lambda_1^{-2}\lambda_2^{-2} - 3)} \frac{1}{J_m} \quad (82)$$

where  $V$  represents the voltage through the thickness direction and  $P_x$  and  $P_y$  demonstrate the pressure applied on the free stretch direction. Depending on whether the  $\sigma_2 = 0$  or  $\sigma_1 = 0$  the equation of either 81 or 82 can be used.

To successfully fold a spiral box pleat, certain length and ratio of the width  $W$  and height  $H$  should be satisfied by the Kresling pattern. The width and height ratio to successfully fold a spiral box pleat using Kresling patterns lies between the 3:4 ratio which is equivalent to 2.125 inches and 2.75 inches. The width and length are derived from a single cell of a letter size paper where the width and the length are folded 4 times along each direction. The initial length of the VHB 4905/4910 is 1 inch. As discussed above, either the width  $W$  or the height  $H$  will be fixed. When the width is fixed, the elastomer will be stretched along the height direction and when the height is fixed, the elastomer will be stretched along the width.

Based upon the geometrical parameters of the Kresling pattern shape, material parameters for different hyperelastic modeling methods are shown below.

Table 5.5 Material properties and geometrical parameters used for modeling [9, 23, 24]

Hyperelastic Theory		Material Constants		
Stretch Ratio		$\lambda_{2.125}$	$\lambda_{2.75}$	$\lambda_{3.5}$
<b>Neo-Hookean</b>	$\mu =$	50kPa	55kPa	62kPa
<b>Ogden</b>	$\mu_p =$	28.9kPa	43.56kPa	92.29kPa
	$\alpha_p =$	1.13	1.445	1.95
<b>Mooney Rivlin</b>	$C_{10} =$	190kPa	220kPa	290kPa
	$C_{01} =$	40kPa	46kPa	55kPa
<b>Gent</b>	$J_m =$		120	
	$\mu =$	50kPa	55kPa	62kPa

Using the following material constants and stretch ratios, the following theoretical curves were obtained.

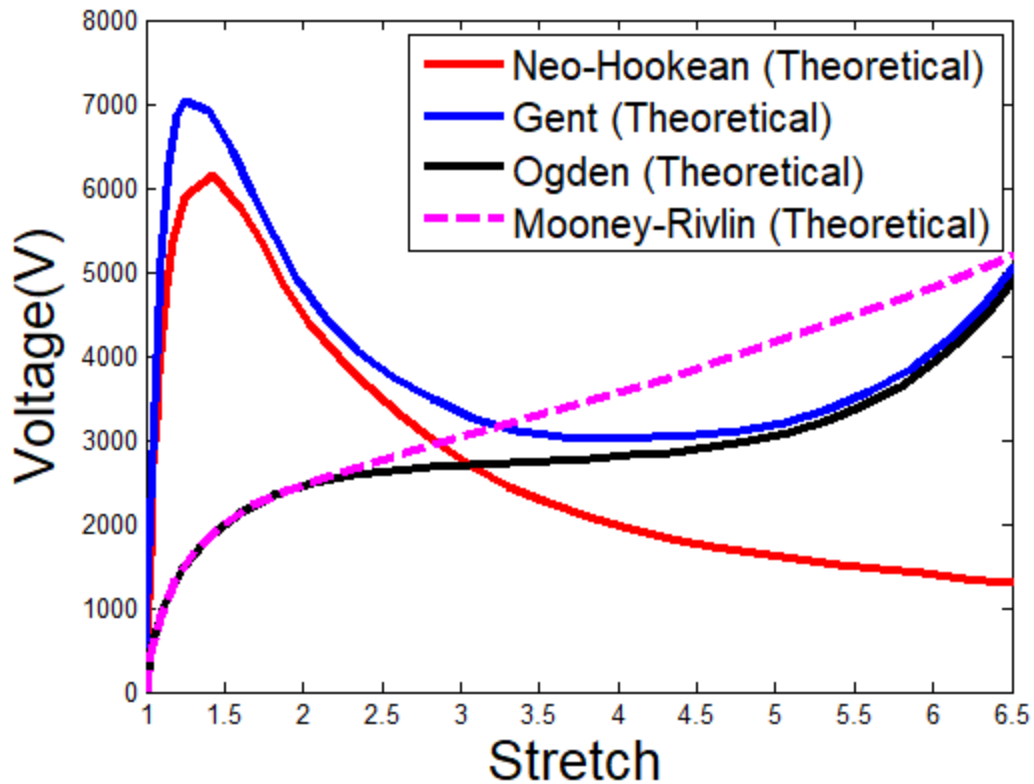


Figure 5.12 Theoretical curves when no pre-stretch was applied.

Figure 5.12 demonstrates the results based on the stretch deformation vs. voltage when no pre-stretch was applied.

### 5.4.3 Geometrical Modeling of Kresling Pattern

Geometrical modeling of the origami DEA is based on the Kresling pattern. Since the Kresling pattern is a rectangular shape, the Kresling pattern shows two different lengths in width and height. For our model, the width is 2.125 inches and the height is 2.75 inches. The initial length of the DEA before pre-stretching in width and height is 1 inch in both directions. By folding the dimension of the pre-stretched rectangular shape, the Kresling pattern is achieved. By combining 4 iterations of the Kresling pattern, it

allows us to create a unique origami shape also known as spiral box pleat that looks like an hourglass. This can be shown in previous work on origami DEA using the Kresling pattern. The figure involving thickness for spiral box pleat is shown below.

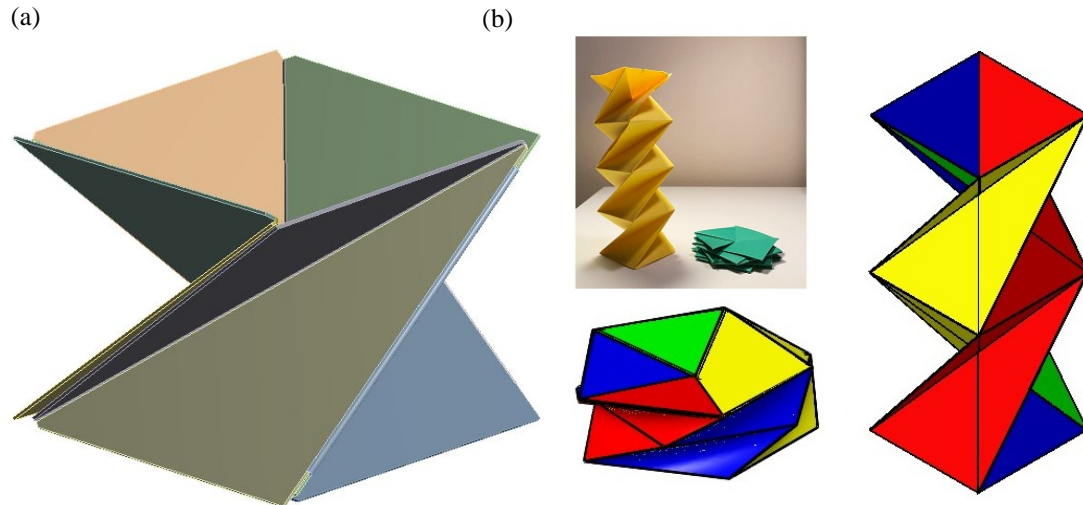
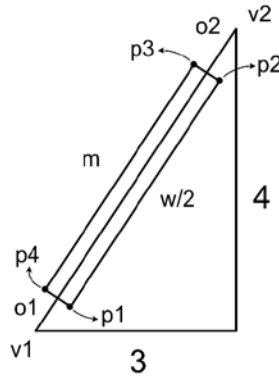


Figure 5.13 (a) FEA model of spiral box pleat and (b) folded model of spiral box pleat using paper. The FEA model show thickness and smooth folding whereas the paper fold neglect to thickness and the smooth fold due to the thickness of paper being negligible. A single cell of the spiral box pleat was evaluated for the numerical analysis below for single layer as well as three combined layers. [27]

Unlike a sheet of paper, where the thickness is nearly negligible, the dielectric elastomer inhibits thickness which makes the folded regions inaccurate. Paper folded creases are precisely folded to perfection whereas sheet materials with thickness are either bent or folded with excess materials bulging out from the folded region. This happens since the bent or folded sheet materials have a higher order of continuity than paper and are often referenced as the smooth folds. Where paper can be folded when a crease is present, materials with thickness need a smooth surface between the two rigid faces. This is governed by the folding width and the folding width increases depending on the angle that is required to be folded. The fold ratio of the Kresling pattern can be

simplified to width and height being 3:4. That being said, we can tell that the length of hypotenuse is 5. Using these ratios, we can find the required length of the smooth fold. The dimensions of the smooth fold can be determined as a rectangle with four corners. By finding the four corners, the dimension required for the smooth fold can be obtained. The schematics for determining the four corners are shown in Figure 5.14.

We determine in Figure 4.14 the width ratio of the smooth fold to be 0.05 mm (distance between  $p1$  to  $p4$ ) and the Kresling pattern width ratio



$$\begin{aligned}
 p1 &= v1 - \frac{w}{2} \left( e3 \times \frac{m}{||m||} \right) + o1 \left( \frac{m}{||m||} \right) \\
 p2 &= v2 - \frac{w}{2} \left( e3 \times \frac{m}{||m||} \right) - o2 \left( \frac{m}{||m||} \right) \\
 p3 &= v2 + \frac{w}{2} \left( e3 \times \frac{m}{||m||} \right) - o2 \left( \frac{m}{||m||} \right) \\
 p4 &= v1 + \frac{w}{2} \left( e3 \times \frac{m}{||m||} \right) + o1 \left( \frac{m}{||m||} \right)
 \end{aligned}$$

Figure 5.14 Geometry of smooth fold and the four points that determines the boundary of the smooth fold for Kresling pattern.

is 3 and the height ratio is 4. The distance between point  $v1$  to the smooth fold width ( $p1$  and  $p4$ ) is the offset and that distance is  $o1$  and  $o2$  in both directions. The length of the vector of the hypotenuse is  $m$ , which is placed between point  $v1$  and  $v2$  where the valley fold occurs. We pre-determine that  $w = 0.05$ ,  $o1$  and  $o2$  to be 0.6,  $v1 = [0 \ 0 \ 0]^T$  for the model. It can be determined that vector  $m$  and  $v2$  can be given as  $m = [3;4;0]$  and  $v2 = [3;4;0]$ . Therefore we can find  $m/||m|| = [3/5;4/5;0]$  and  $e3 \times m/||m|| = [-4/5;3/5;0]$ , which leads us to finding point  $p1$ ,  $p2$ ,  $p3$ , and  $p4$ .

This equation allows us to find the four points of the smooth fold, which enables us to determine the width of the smooth fold where it falls within the shape of the

geometry provided. The stiffener will be placed where the four points of the smooth fold are located to provide stiffness to the area while making the DEA structure to bend. In a previous paper by Shian *et al.* [60], it was indicated that different fiber placements along the DEA were placed to aid bending of the DEA structure. This allows the stiffener to be bulkier to withstand more weight as well as the structure to bend at the desired locations. By combining the geometrical model along with the hyperelastic model of the DEA, geometry for numerical analysis was created.

#### 5.4.4 Analytical Modeling without Fixed End

Geometrical modeling of the Kresling pattern introduces a new modeling method using different stretch ratios. Based on the geometry of the Kresling pattern, it was identified previously that the right angle triangle can be formed based upon the three different ratios of 3:4:5. Based on these sets of ratios, the length of the ratio 5 can be determined. The length is 3.5 inches where we use this as the stretch ratio of 3.5. Since the stretch is conducted diagonally along the hypotenuse, this refers to an equi-biaxial stretch. Now we consider that the model has been stretched in equi-biaxial ratio of 3.5 compared to its initial length. The following equation can be determined,

$$\sigma_{1,2} + \varepsilon E^2 = \lambda \frac{P}{DT} + \varepsilon \left( \lambda^2 \frac{V}{T} \right)^2 = \frac{\mu(\lambda^2 - \lambda^{-4})}{1 - (2\lambda^2 - \lambda^{-4} - 3)} \frac{1}{J_m} \quad (83)$$

where  $D$  stands for the diagonal length translated to the x and y axis. This will be used to determine how the hyperelastic model behaves under equi-biaxial stretch when stiffeners are applied.



## 5.5 Numerical Analysis of Kresling Pattern

Numerical analysis was conducted by using different material parameters obtained by different hyperelastic models. The material parameter constants were derived from multiple literature studies based upon 3M VHB 4905/4910 material testing [9, 23, 24, 30]. Material properties for thin polyester film and sheets were obtained from Mylar with modulus of elasticity of 710,000 psi and density of 1.39 [27]. Numerical analysis on Mooney-Rivlin, Neo-Hookean, and Ogden was conducted in comparison to the analytical results as well as the Gent model. In this paper, three different stretch ratios were used for analysis based on the dimensions of the Kresling pattern. The Kresling patterns can be cut diagonally forming a trapezoid with the 3 length ratios of 3:4:5. This can be converted to stretch ratios based on the three length of the Kresling pattern which results in 2.125, 2.75 and 3.5 respectively.

Four failure modes for DEA were mentioned in Suo's paper [54]. Electrical breakdown, electromechanical instability, loss of tension and reaching the stretch limit. From the analytical solution, the local maximum displays the points where the loss of tension or electrical breakdown may occur [11]. Using the local maximum as a reference, numerical analysis was performed. For numerical analysis, different material parameters were determined through literature studies for different stretch ratios. Since the exact material parameters for the different stretch ratios used for the current study couldn't be obtained, slight variation of material parameters were collected. For  $\lambda_1 = 2.125$ , material parameters for  $\lambda_1 = 2$  was used. For  $\lambda_2 = 2.75$ , material parameter for  $\lambda_2 = 2.5$  was used. For equi-biaxial stretch  $\lambda = 3.5$ , material parameters for  $\lambda = 3$  was used [9, 23, 24, 30].

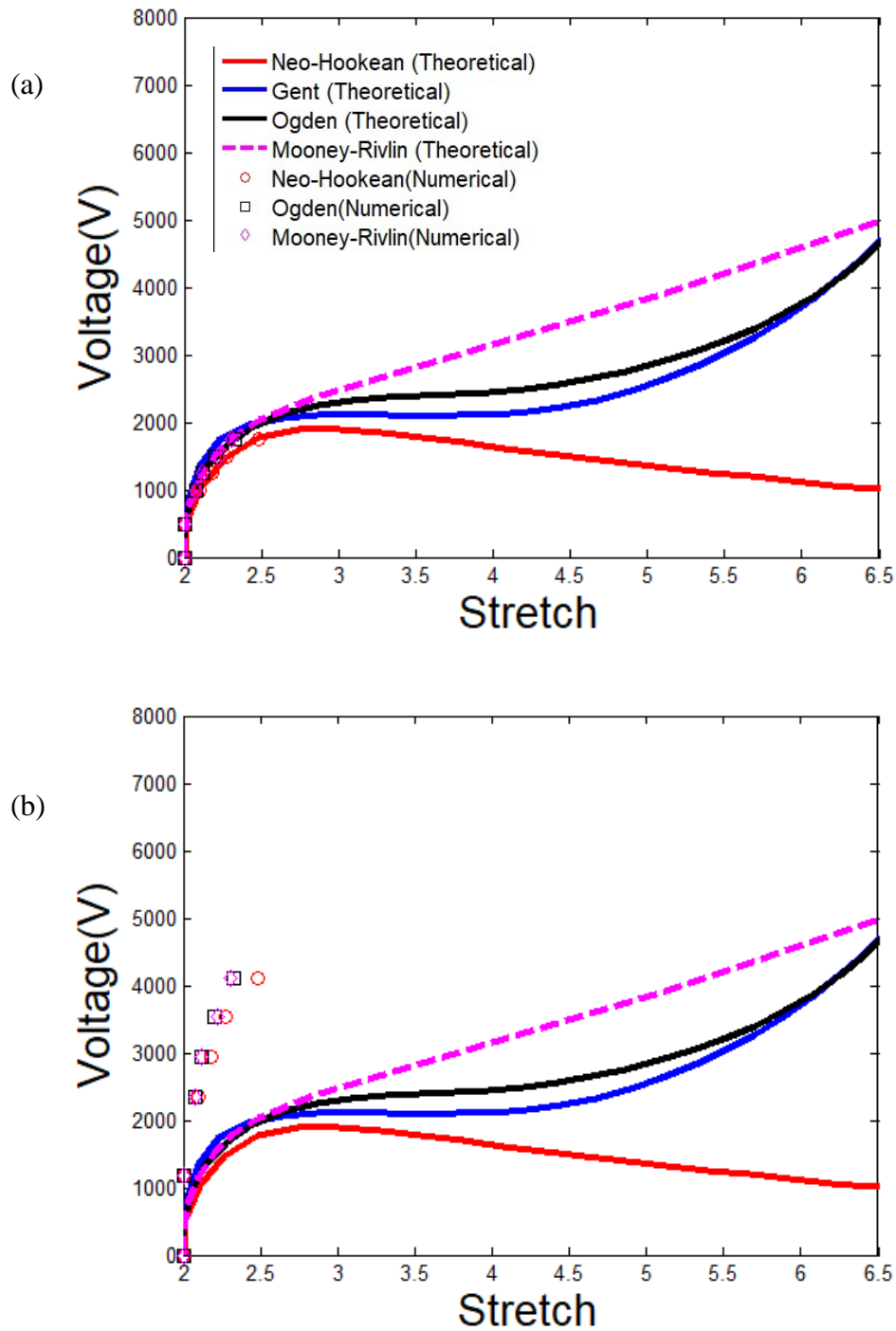


Figure 5.15 (a) Theoretical curves for  $\lambda_1=2.125$  are represented in both plot along with the data points acquired from numerical analysis. The circular, square and diamond dots represent the numerical results without the stiffener. (b) Numerical results with the stiffener were obtained and are demonstrated as circular, square and diamond dots. Theoretical curves without the stiffener were plotted for reference.

The continuous solid and dotted lines indicate the theoretical curves of the four different hyperelastic models, Gent, Neo-Hookean, Mooney-Rivlin, and Ogden. The blue solid line indicates the theoretical Gent model. The numerical analysis results are displayed as points of circle, square and triangle based upon the three different hyperelastic models. From the Figure 4.15 (a), the peak of the theoretical curve can be observed. The voltage increases as the DEA experiences decrease in thickness direction. However, after the DEA reaches a certain point, which is the peak of the theoretical curve, the DEA experiences loss of tension or electromechanical instability [11]. From figure 4.15(b), more voltage is required due to the addition of the stiffener to the DEA structure.

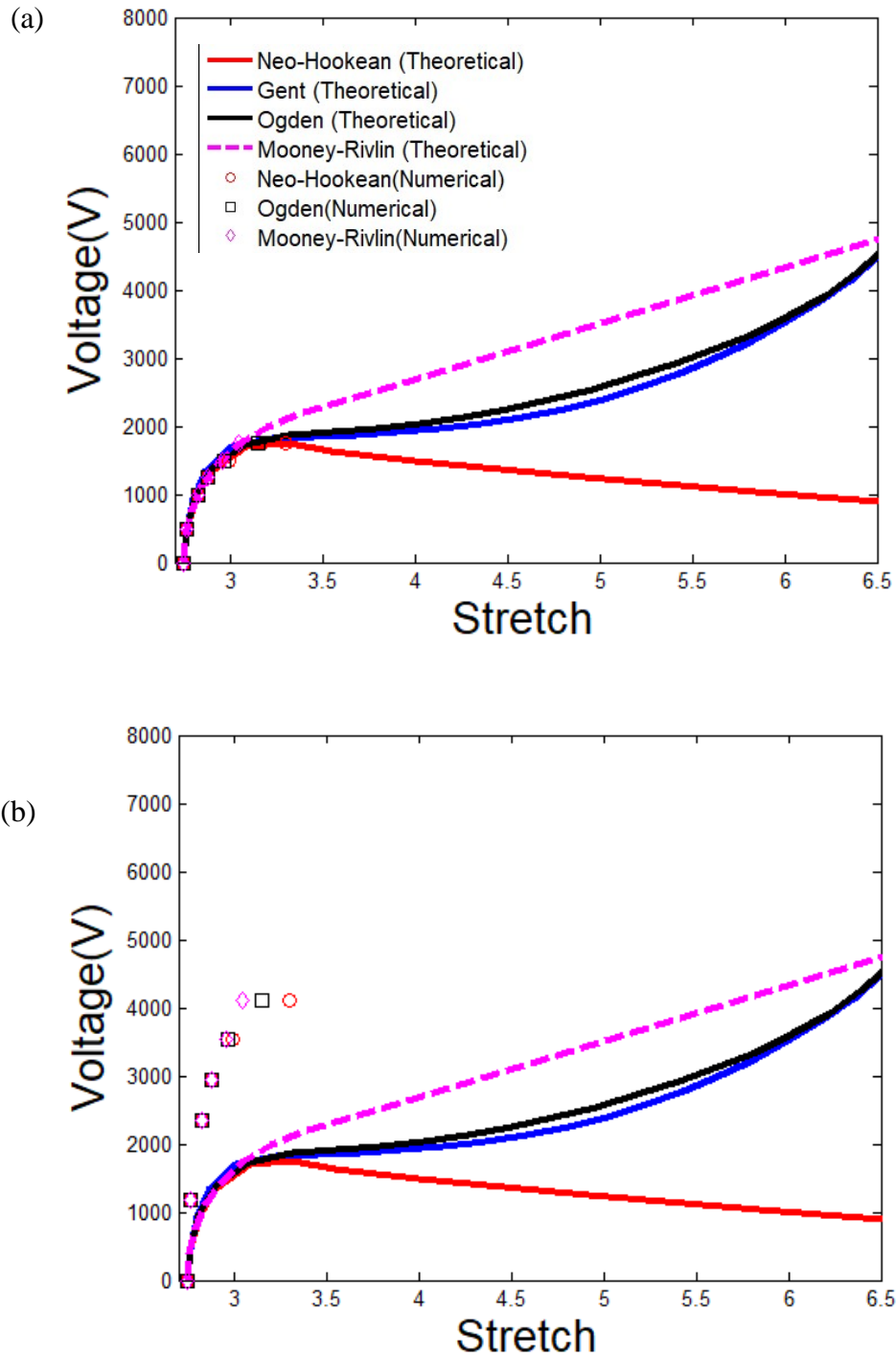


Figure 5.16 (a) Theoretical curves for  $\lambda_1 = 2.75$  are represented in solid lines. The circular, square and diamond dots represent the numerical results without the stiffener. (b) Numerical results with the stiffener were obtained and are demonstrated as circular, square and diamond dots. Theoretical curves without the stiffener were plotted for reference.

There is a constant increase in voltage whereas the theoretical curves experience a increase in voltage, reaches a short plateau, and then increase or decrease in voltage based upon different constitutive models. From Figure 4.15(b) and 4.16(b), the effect of stiffener can be observed. The addition of stiffener has caused increases in actuation pressure which resulted in increases in actuation voltage.

Previously, equi-biaxial model using the stretch ratio of 3.5, which was obtained from the hypotenuse of the triangle illustrated in Figure 4.14 was discussed. Stiffener was added to the DEA model in order to determine the influence of the stiffeners to the overall structure with respect to the strain and actuation voltage. For larger stretch ratios, a monotonic behavior is expected where displacement increases steadily along with the increase in voltage.

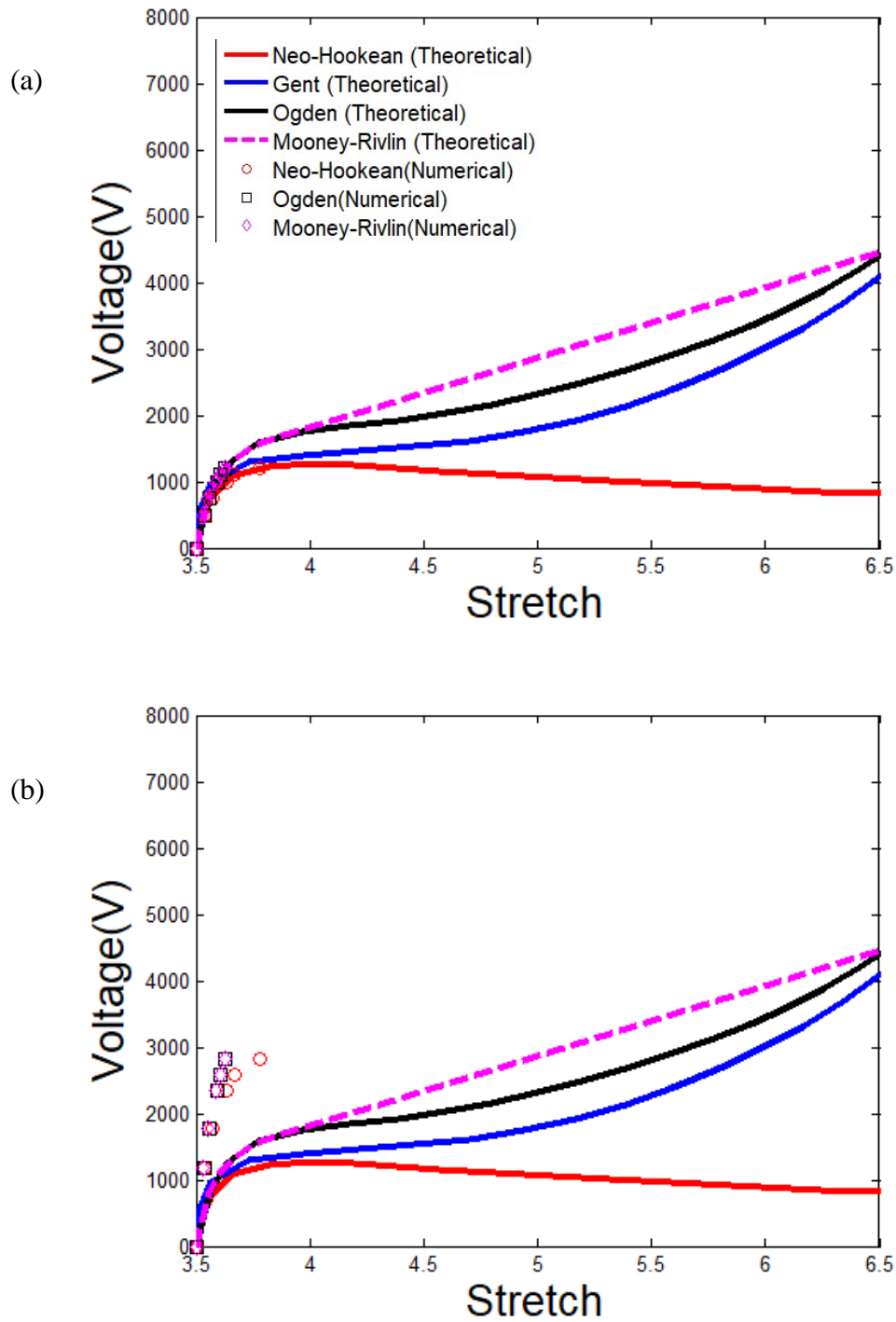


Figure 5.17 (a) Theoretical curves for  $\lambda_1 = 3.5$  are represented in solid lines. The circular, square and diamond dots represent the numerical results without the stiffener. (b) Numerical results with the stiffener were obtained and are demonstrated as circular, square and diamond dots. Theoretical curves without the stiffener were plotted for reference.

The result of finite element method (FEM) model by using ABAQUS can be seen below. FEA was conducted with and without stiffener to observe the behavior of actuation voltage, displacement and bending or folding of the actuator caused due to the stiffener. The following figure demonstrates a result obtained without the stiffener when the width was constrained and subjected to pressure equivalent to 12 kV.

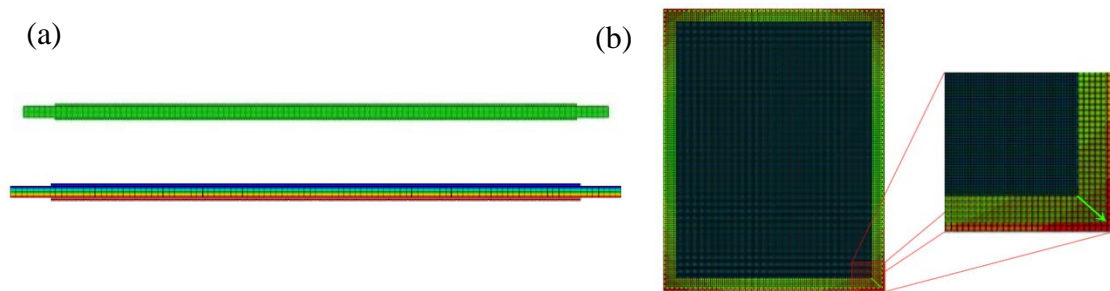


Figure 5.18 (a) FEA result without stiffeners when subjected to 12 kV along the thickness direction and the planar direction for stretch ratio along the vertical direction. (b) Approximately 10% strain was obtained.

From numerical analysis, deformation strain was determined. The deformation strain was determined by comparing the initial length of the elastomer to the maximum displacement corresponding to actuation voltage. By determining the maximum displacement in the planar direction and assuming the DEA is incompressible, we can determine the overall deformation vs. voltage relationship.

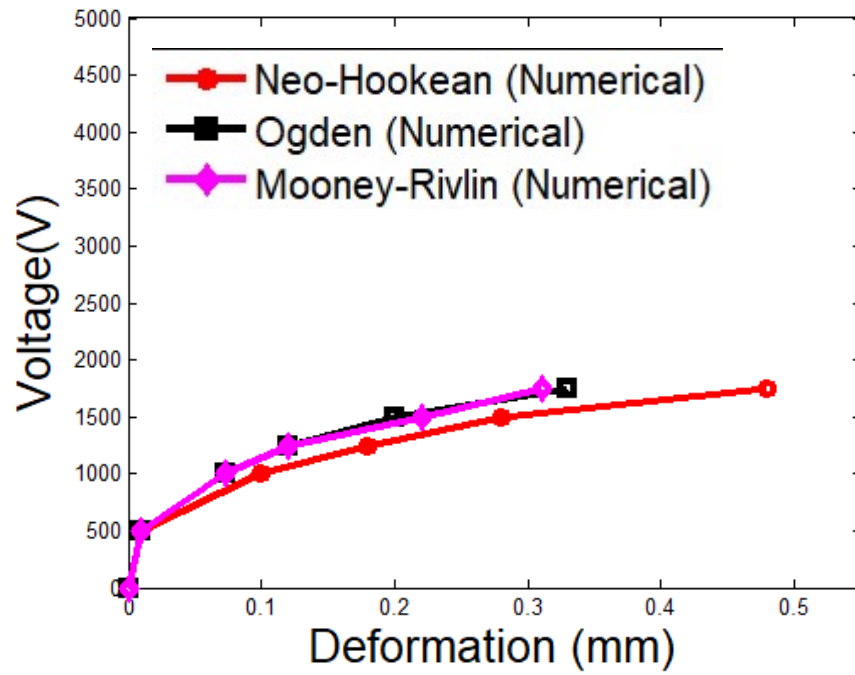


Figure 5.19  $\lambda_1 = 2.125$  Deformation vs. Voltage without stiffener.

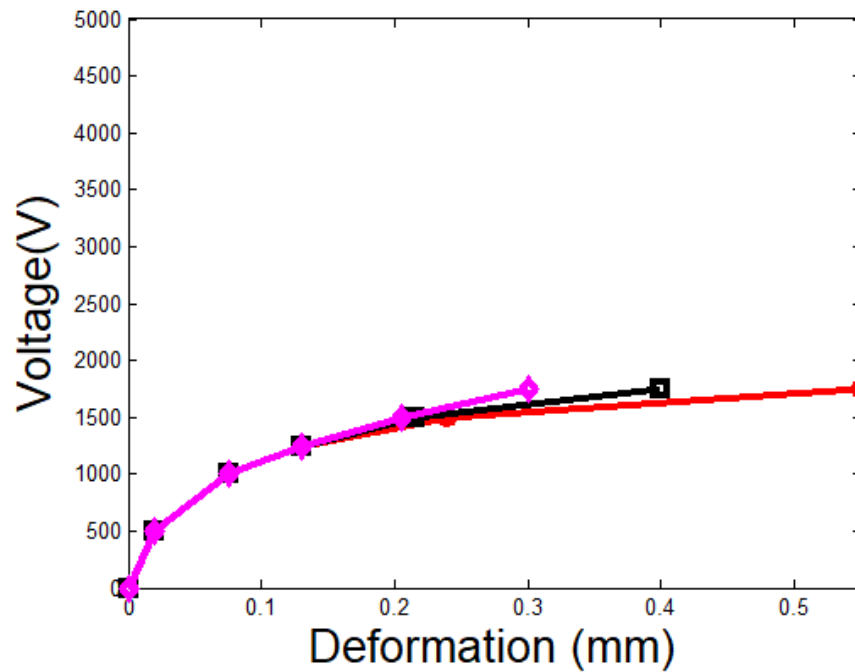


Figure 5.20  $\lambda_1 = 2.75$  Deformation vs. Voltage without stiffener. The legend can be seen in Figure 5.19.



Due to the fact that voltage is constantly increased, we can determine the peak of the theoretical slopes. Based upon applying actuation voltage of 1500V, amount of deformation was compared through numerical analysis. The DEA experienced 15% strain for  $\lambda_1 = 2.125$  and 18% strain for  $\lambda_2 = 2.75$  in average based upon different constitutive models.

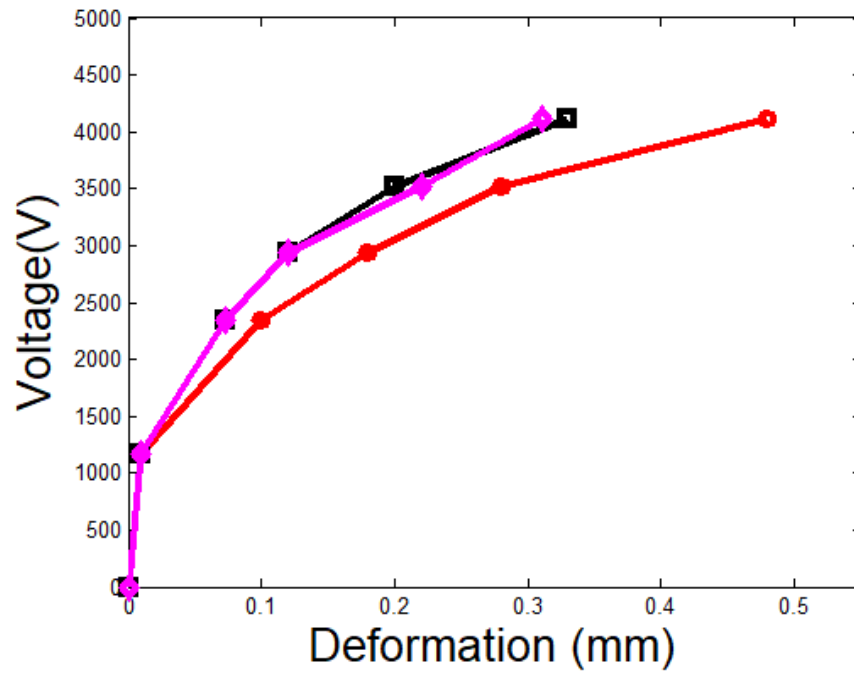


Figure 5.21  $\lambda_1 = 2.125$  Deformation vs. Voltage with stiffener. The legend can be seen in Figure 5.19.

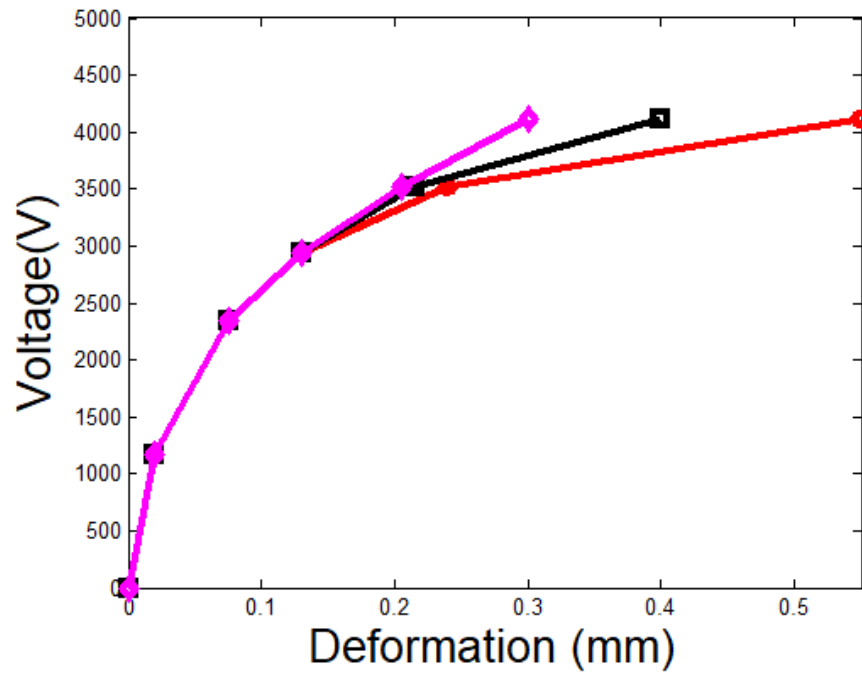


Figure 5.22  $\lambda_1 = 2.75$  Deformation vs. Voltage with stiffener. The legend can be seen in Figure 5.19.

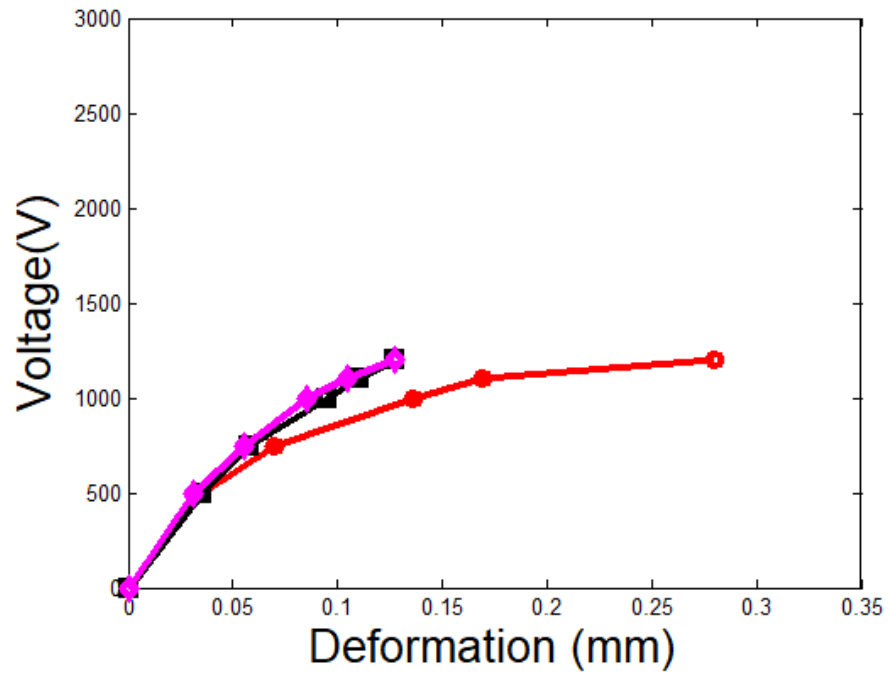


Figure 5.23  $\lambda_1 = 3.5$  Deformation vs. Voltage without stiffener. The legend can be seen in Figure 5.19.

The theoretical curve displayed a monotonic behavior where the displacement increased along with the actuation voltage. The value obtained from numerical analysis, have been showing a monotonic behavior. This shows that at higher stretch ratio, electromechanical instability can be eliminated as well as the loss in tension.

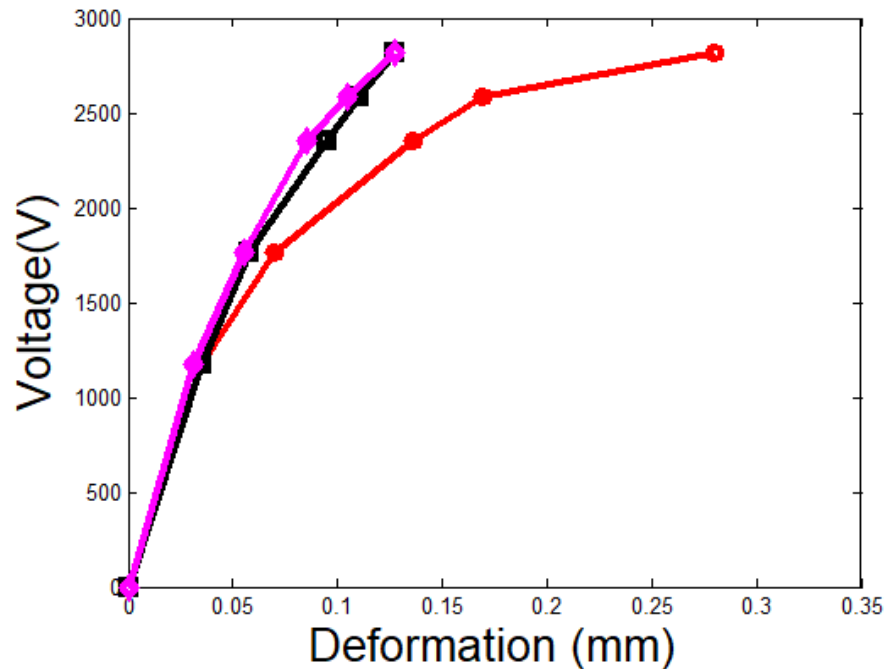


Figure 5.24  $\lambda_1 = 3.5$  Deformation vs. Voltage with stiffener. The legend can be seen in Figure 5.19.

The failure modes are no longer present with high stretch ratio. The theoretical curve demonstrates a monotonic behavior where large strain can be observed as well as lower actuation voltage. Despite the fact addition of stiffener adds actuation voltage, at higher stretch ratio, the required actuation voltage was a lot less compared to the other two stretch ratios.

## 5.6 Results

The spiral box pleat is made from repetition of Kresling pattern along the horizontal direction. In order to simplify the problem, 3 layers of DEA will be simplified into one rectangular geometry with the equivalent thickness of a 3 layered DEA. Bending of the stacked DEA was analyzed based upon the simplified geometry.

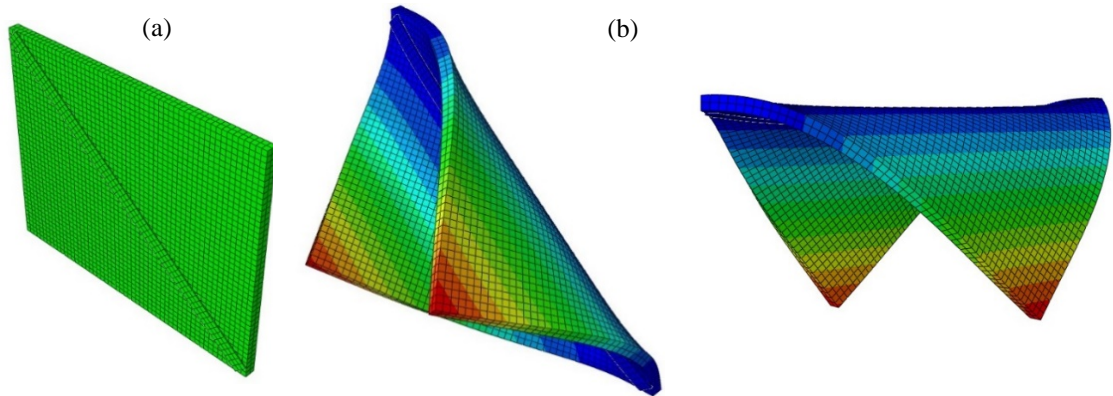


Figure 5.25 (a) Location of the 4 points of stiffener based on the analytical solution of geometrical modeling of the stiffeners for the smooth folding surface. (b) The stiffener required more voltage for actuation however, the bending of the DEA occurred along the stiffeners.

The bending of the DEA with stiffener is crucial to determine the performance of the Kresling spiral box pleat. Based upon the theoretical curves, the Ogden model best represented the theoretical curve of the Gent model. Bending angles were obtained based upon Ogden model by applying different voltages with the corresponding strain. In order to demonstrate how bending angle was obtained, actuation pressure equivalent to 6 kV was applied. By using ABAQUS Query, the angle of each element along the neutral axis of the Kresling DEA was determined. There are 32 elements along the width of the Kresling pattern and change in angle for each of the elements were obtained. By plotting the change in angle of each element, the bending from the stiffener to the tip of the DEA was obtained. Each element was plotted corresponding to the change in angle between

the nodes in the element. This is shown in Figure 4.26 (b) in different colors. In Figure 4.26 (c) the bending geometry can be seen. The blue line represents the initial position of the DEA before actuation and the black line represents the change in angle which is interpreted as the bending of overall structure.

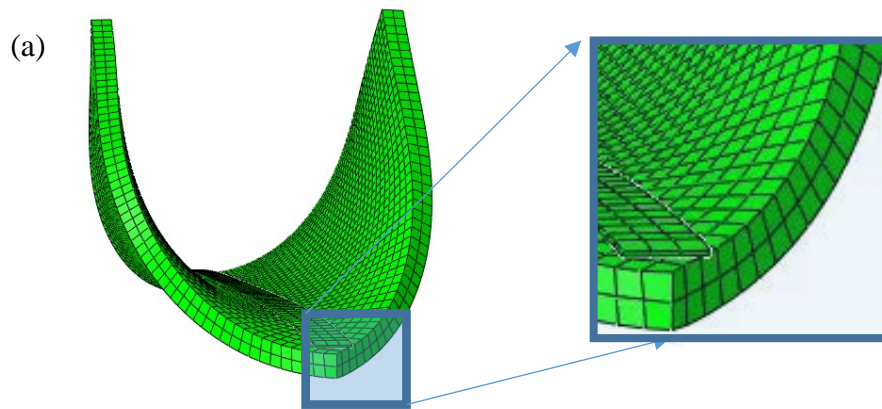


Figure 5.26 (a) The bending angle of the origami DEA. The neutral axis is pointed by the extruded line. The bending angles were measured based on change in each element.

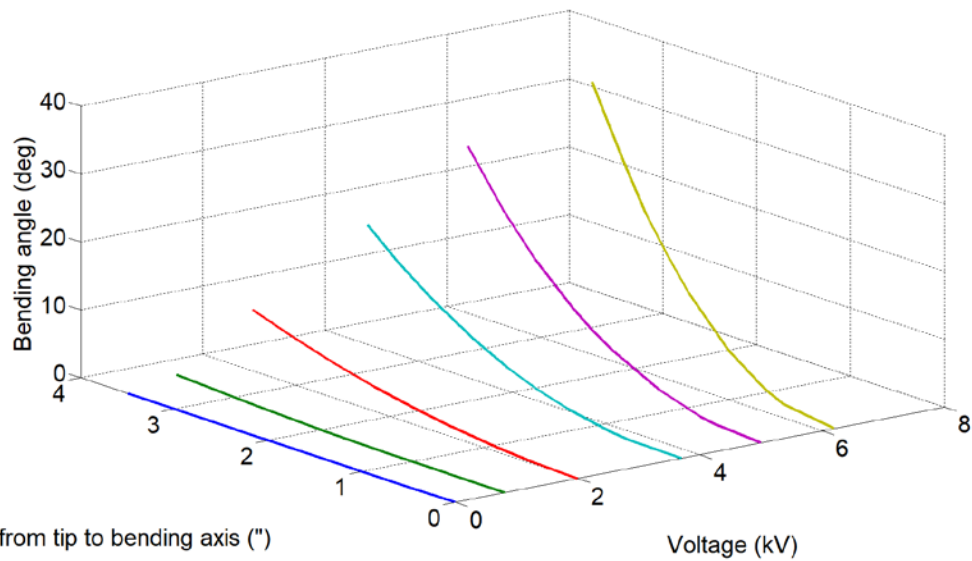


Figure 5.27 Bending angle vs. voltage vs. tip displacement. The higher voltage, the more bending was observed.

The capability of dielectric elastomer actuators for bending actuation was studied through the kinematics of origami folds and the hyperelastic material modeling. Ideal

material parameter for origami DEA application was obtained by studying the stretch-voltage relationship based on theoretical curve of different hyperelastic models. Numerical analysis was performed to determine the actuation voltage as well as the strain caused by the DEA. Later, stiffener was added to the DEA to determine the bending angle. The bending angle was obtained by applying different voltages. The bending occurred on each element of the DEA was examined to determine the overall bending angle of the DEA structure. The bending angle obtained by the numerical results was approximately 39.2 degrees when 6 kV was applied. The DEA is suitable for bending or folding actuations where the DEA is applied to perform low to medium range of bending actuation. Thus, the numerical results support the idea that the DEA is capable of actuating active origami structures.

## **Chapter 6. Conclusion and Future Work**

Different structural DEAs were investigated in this study. The continuous HDEA structure poses multiple benefits but yet it has numerous obstacles when it comes to manufacturing. The procedures for manufacturing the complex shape of HDEA were tested but were unable to achieve a successful prototype. By far, the best method to manufacture a HDEA would be through 3-D printing. However, this also poses a lot of obstacles, and the current method requires different approaches to solve the problem of manufacturing. However, this research demonstrated that HDEA manufactured using silicone DEA would be feasible since no pre-stretching would be needed. As some literature reviews suggested, the amount of strain might be limited compared to acrylic DEA.

Since large strain was one of the main objectives in this research, acrylic material VHB 4910 was investigated based on the massive amount of research conducted around this material for DEA applications. The literature review demonstrated 500% strain for DEA. DEA can be effective actuators for certain applications and the application that was focused on was origami structures. Origami structures can be deployed and packed in a confined area which modern robotic structures pose obstacles performing those tasks. Combining origami structures with soft materials that actuate the entire structure would be a novel design in robotics community.

A continuous robotic structure was investigated and thus spiral box pleat origami structure was used along with DEAs. The first paper based on origami introduced the DEA just being a live system alike a living hinge. The next paper demonstrated the origami DEA where the entire structure was designed with elastomeric material with

stiffeners to maintain the shape of the elastomers after pre-stretch. Since there were multiple hyperelastic modeling methods, different types of modeling methods were investigated. Different modeling methods demonstrated varying results but the results of overall strain exerted by the elastomer were small (<50%). Different modeling methods inhibit the benefits of curve fitting based on small to large strains and since the strain of the model was small, different hyperelastic model possesses a small difference between each other.

However, the spiral box pleat can move based on a small amount of strain to obtain up to 700% actuation. Based on the simulation result, the spiral box pleat can obtain up to 400% actuation, when compared to its non-deployed state of the overall structure. Therefore, the investigation of different structures with modern engineering principles can provide mutual benefits to successfully overcome obstacles possessed in the field.

As future work, more origami and bio-inspired structures will be investigated as well as the optimization of spiral box pleat fiber locations. This can increase the overall performance of the actuator. Fabrication of the spiral box pleat is currently being worked on by introducing polyester film as the frame for DEA to be mounted upon.



## Chapter 7. References

- [1] Shintake, J., Rosset, S., Schubert, B., Floreano, D., and Shea, H., “Versatile Soft Grippers with Intrinsic Electroadhesion Based on Multifunctional Polymer Actuators,” *Advanced Materials*, 28, 231–238 (2016).
- [2] Shankar, R., Ghosh, T. K., and Spontak, R. J., “Dielectric elastomers as next-generation polymeric actuators,” *Soft Matter*, 3, 1116 (2007).
- [3] Madden J.D.W, Vandesteeg N.A, A. P. ., Madden, J. D. W., Vandesteeg, N. a., Anquetil, P. a., Madden, P. G. a, Takshi, A., Pytel, R. Z., Lafontaine, S. R., Wieringa, P. a., and Hunter, I. W., “Artificial muscle technology:Physical principles and Naval prospects,” *IEEE J. Oceanic Eng*, 29 (3), 7006-28 (2004).
- [4] Kovacs, G., “Arm Wrestling Robot Driven by Dielectric Elastomer Actuators,” *IEEE Biomedical Robotics and Biomechatronics*, Pisa, Italy (2006).
- [5] Brochu, P., and Pei, Q., “Advances in dielectric elastomers for actuators and artificial muscles,” *Macromolecular Rapid Communications*, 31, 10–36 (2010).
- [6] Jordi, C., Dürager, C., and Michel, S., “Dielectric-elastomer-driven airship uses fish-like propulsion,” *SPIE Newsroom*, (2010)
- [7] Koh, S. J. A., Li, T., Zhou, J., Zhao, X., Hong, W., Zhu, J., & Suo, Z., “Mechanisms of large actuation strain in dielectric elastomers,” *Journal of Polymer Science, Part B: Polymer Physics*, 49(7), 504–515 (2011).
- [8] Plante, J. S., and Dubowsky, S., “Large-scale failure modes of dielectric elastomer actuators,” *International Journal of Solids and Structures*, 43, 7727–7751 (2006).

- [9] Kovacs, G., Düring, L., Michel, S., and Terrasi, G., “Stacked dielectric elastomer actuator for tensile force transmission,” *Sensors and Actuators, A: Physical*, 155, 299–307 (2009).
- [10] Carpi, F., and De Rossi, D., “Contractile Folded Dielectric Elastomer Actuators,” *Proceedings of the SPIE, Electroactive Polymer Actuators and Devices (EAPAD), Smart Structures and Materials*, 6524 (2007).
- [11] Benslimane, M. Y., Kiil, H. E., and Tryson, M. J., “Dielectric electro-active polymer push actuators: Performance and challenges,” *Polymer International*, 59, 415–421 (2010).
- [12] Carpi, F., Migliore, A., Serra, G., and De Rossi, D., “Helical Dielectric Elastomer Actuators,” *Smart Materials and Structures*, 14(6), 1-7 (2005).
- [13] Gbaguidi, A., Konduru, V. K., Kim, D., “Analytical Approach on the Performance of Helical Dielectric Elastomer Actuator,” *Proc. SPIE 9798, Electroactive Polymer Actuators and Devices (EAPAD)*, 979814, 1–14 (2016).
- [14] Carpi, F., and De Rossi, D., “Small-strain modeling of helical dielectric elastomer actuators,” *IEEE/ASME Transactions on Mechatronics*, vol. 17, 318–325 (2012).
- [15] Yun Y., “Control in the reliable region of a statistical model,” *IEEE Transactions on Robotics*, vol 32, 1017-1025 (2016).
- [16] Pelrine R., Kornbluh, R., Joseph, J., Heydt, R., Pei, Q., and Chiba, S., “High-field deformation of elastomeric dielectrics for actuators,” *Materials Science and Engineering: C*, 11(2), 89-100 (2000).

- [17] Altameem, T. A, Nikolić, V., Shamshirband, S., Petković, D., Javidnia, H., Mat Kiah M. L., and Cani, A., “Potential of support vector regression for optimization of lens system,” *Computer-Aided Design*, 62, 57-63 (2015).
- [18] Poulin, A., Rosset, S., and Shea, H., “Fully printed 3 microns thick dielectric elastomer actuator,” *Proc. of SPIE*, 9798, (2016).
- [19] Hinton, T.J., Hudson, A., Pusch, K., Lee, A., Feinberg, A.W., “3D printing PDMS elastomer in a hydrophilic support bath via freeform reversible embedding,” *ACS Biomater Sci. Eng.*, 2(10), 1781-6 (2016).
- [20] Lee, Y., Oh, S., and Choi, D. H., “Design optimization using support vector regression,” *Journal of Mechanical Science and Technology*. 22(2), 213-20 (2008).
- [21] Wissler, M. and Mazza, E., “Modeling of a pre-strained circular actuator made of dielectric elastomers,” *Sensors and Actuators A: Physical*. 120(1), 184-92 (2005).
- [22] Boyraz, Pinar, et al. “An Overview of Novel Actuators for Soft Robotics.” *Actuators*, vol. 7, no. 3, 2018
- [23] Oberg, E., [Machinery's handbook], 28th ed, Industrial Press, New York, (2008).
- [24] Madsen, F. B., Daugaard, A. E., Hvilsted, S. and Skov, A. L., “The current state of silicone-based dielectric elastomertransducers. ” *Macromolecular Rapid Communications* 37,378–413 (2016).
- [25] Park, J. H., Nair, S. and Kim, D., “Numerical analysis of helical dielectric elastomer actuator,” *Proc. of SPIE*, 10163 (2017).
- [26] Zahab, Z. E., Divo, E., and Kassab, A. “Minimisation of the wall shear stress gradients in bypass grafts anastomoses using meshless CFD and genetic algorithms

optimization,” *Computer Methods in Biomechanics and Biomedical Engineering*, 13(1), 35-47 (2010).

[27] Jiang, L., Zhou, Y., Chen, S., Ma, J., Betts, A. and Jerrams, S., “Electromechanical instability in silicone- and acrylate-based dielectric elastomers,” *Journal of Applied Polymer Science*, 135(9), 1-6 (2017).

[28] Ojeda, D., Divo, E., Kassab, A., and Cerrolaza, M., “Cavity detection in biomechanics by an inverse evolutionary point load BEM technique,” *Inverse Problems in Science and Engineering*, 16(8), 981-993 (2008).

[29] Divo, E., Kassab, A. J., and Rodriguez, F., “An efficient singular superposition technique for cavity detection and shape optimization,” *Numerical Heat Transfer, Part B: Fundamentals*, 46(1), 1-30 (2004).

[30] Castro, J., Rojas, E., Weller, T., and Wang, J., “Engineered nanocomposites for additive manufacturing of microwave electronics,” *International Symposium on Microelectronics*, vol. 2015, no. 1, 189-196 (2015).

[31] Tiwari, A., Mandal, A., and Kumar, K., “Multi-objective optimization of electro-chemical machining by non-dominated sorting genetic algorithm,” *Materials Today: Proceedings*, vol.2, no. 5, 2569-2575 (2015)

[32] B. Kresling, "Natural Twist Buckling in Shells: From the Hawkmoth's Bellows to the Deployable Kresling-Pattern and Cylindrical Miura-ori," *Proceedings of the 6th International Conference on Computation of Shell and Spatial Structures IASS-IACM: "Spanning Nano to Mega"*, (2008).

[33] W. D. Reynolds, and T. W. Murphey, [Elastic Spiral Folding for Flat Membrane Apertures] *American Institute of Aeronautics and Astronautics*, (2014).

- [34] C. Jianguo, D. Xiaowei, Z. Ya, F. Jian, and T. Yongming, "Bistable Behavior of the Cylindrical Origami Structure With Kresling Pattern," *Journal of Mechanical Design*, 137(6), (2015).
- [35] M. Sakovsky, S. Pellegrino, and H. M. Y. C. Mallikarachchi, [Folding and Deployment of Closed Cross-Section Dual-Matrix Composite Booms] *American Institute of Aeronautics and Astronautics*, (2016).
- [36] B. Gopalarethinam, and J. Yang, [Origami-based Tunable Structures with Simultaneously Foldable and Stiff Behavior] *American Institute of Aeronautics and Astronautics*, (2018).
- [37] A. Senba, and T. Hasegawa, [A Concept of Self-Shape Generation of Membrane Structures Using Shape Memory Polymer Patches] *American Institute of Aeronautics and Astronautics*, (2019).
- [38] S. Ahmed, C. Lauff, A. Crivaro, K. McGough, R. Sheridan, M. Frecker, P. Von Lockette, Z. Ounaies, T. Simpson, J.-M. Lien, and R. Strzelec, "Multi-field responsive origami structures: Preliminary modeling and experiments," *ASME 2013 International Design Engineering Technical Conferences and Computers and Information in Engineering Conference*, 6 B, (2013).
- [39] S. A. Zirbel, R. J. Lang, M. W. Thomson, D. A. Sigel, P. E. Walkemeyer, B. P. Trease, S. P. Magleby, and L. L. Howell, "Accommodating Thickness in Origami-Based Deployable Arrays," *Journal of Mechanical Design*, 135(11), 111005-111005-11 (2013).
- [40] S. Ahmed, K. McGough, Z. Ounaies, and M. Frecker, "Origami-Inspired Folding and Unfolding of Structures: Fundamental Investigations of Dielectric Elastomer-Based Active Materials," (56031), V001T01A029 (2013).

- [41] B. H. Hanna, [Modeling and Testing of Bistable Waterbomb Base Configurations] Brigham Young University, (2014).
- [42] M. Wissler, and E. Mazza, "Modeling of a pre-strained circular actuator made of dielectric elastomers," *Sensors and Actuators, A: Physical*, 120(1), 184-192 (2005).
- [43] F. B. Madsen, A. E. Daugaard, S. Hvilsted, and A. L. Skov, "The Current State of Silicone-Based Dielectric Elastomer Transducers," *Macromolecular Rapid Communications*, (2016).
- [44] H. Yasuda, and J. Yang, "Reentrant Origami-Based Metamaterials with Negative Poisson's Ratio and Bistability," *Physical Review Letters*, 114(18), 185502 (2015).
- [45] M. Lee, [Tunable Bistability of Origami-based Mechanical Metamaterials] American Institute of Aeronautics and Astronautics, (2017).
- [46] L. Jiang, Y. Zhou, S. Chen, J. Ma, A. Betts, and S. Jerrams, "Electromechanical instability in silicone- and acrylate-based dielectric elastomers," *Journal of Applied Polymer Science*, 135(9), 45733 (2018).
- [47] B. O'Brien, E. ECalius, S. Xie, and I. Anderson, "An experimentally validated model of a dielectric elastomer bending actuator," *SPIE Electroactive Polymers Actuators and Devices Conference, EAPAD*, 6927, (2008).
- [48] T. J. Hinton, A. Hudson, K. Pusch, A. Lee, and A. W. Feinberg, "3D Printing PDMS Elastomer in a Hydrophilic Support Bath via Freeform Reversible Embedding," *ACS Biomaterials Science & Engineering*, 2(10), 1781-1786 (2016).
- [49] X. Li, and Y. Zhou, [Microfluidic Devices for Biomedical Applications] Woodhead Publishing, (2013).

- [50] J. H. Park, A. El Atrache, D. Kim, and E. Divo, "Optimization of Helical Dielectric Elastomer Actuator with Additive Manufacturing," *SPIE Smart Structures/NDE*, (2018).
- [51] Kofod, Guggi, Peter Sommer-Larsen, Roy Kornbluh, and Ron Pelrine, 'Actuation Response of Polyacrylate Dielectric Elastomers', *Journal of Intelligent Material Systems and Structures*, 14: 787-93 (2016).
- [52] Park, J.H, Stanislav,S, D.Kim, E.Divo, and R.Martinez. Numerical Studies on Origami Dielectric Elastomer Actuator Using Kresling Pattern. *Spie Smart Structures + Nondestructive Evaluation*. Vol. 10966: SPIE, (2019).
- [53] Puglisi, Giuseppe, and Giuseppe Saccomandi. "The Gent Model for Rubber-Like Materials: An Appraisal for an Ingenious and Simple Idea." *International Journal of Non-Linear Mechanics* 68 (2015).
- [54] Suo, Zhigang. "Theory of Dielectric Elastomers." *Acta Mechanica Solida Sinica* 23, no. 6 (2010).
- [55] Horgan, Cornelius O. "The Remarkable Gent Constitutive Model for Hyperelastic Materials." *International Journal of Non-Linear Mechanics* 68 (2015).
- [56] Goh, Y. F., S. Akbari, T. V. Khanh Vo, and S. J. A. Koh. "Electrically-Induced Actuation of Acrylic-Based Dielectric Elastomers in Excess of 500% Strain." *Soft Robot* (2018).
- [57] Lu, Tongqing, Jiangshui Huang, Christa Jordi, Gabor Kovacs, Rui Huang, David R. Clarke, and Zhigang Suo. "Dielectric Elastomer Actuators under Equal-Biaxial Forces, Uniaxial Forces, and Uniaxial Constraint of Stiff Fibers." *Soft Matter* 8, no. 22 (2012).

- [58] He, Liwen, Jia Lou, Jianke Du, and Ji Wang. "Finite Bending of a Dielectric Elastomer Actuator and Pre-Stretch Effects." *International Journal of Mechanical Sciences* 122 (2017).
- [59] Bar-Cohen, Yoseph, William Lai, Ashraf F. Bastawros, and Wei Hong. "Out-of-Plane Motion of a Planar Dielectric Elastomer Actuator with Distributed Stiffeners." In *Electroactive Polymer Actuators and Devices, EAPAD* (2012).
- [60] Shian, S., K. Bertoldi, and D. R. Clarke. "Dielectric Elastomer Based "Grippers" for Soft Robotics." *Adv Mater* 27, no. 43 (2015)

### Figure References

- [61] Editors, BD. "Skeletal Muscle." *Biology Dictionary*, 26 Mar. 2019, [biologydictionary.net/skeletal-muscle/](http://biologydictionary.net/skeletal-muscle/).
- [62] "Featured Education - SlideShare." *Www.slideshare.net*, [www.slideshare.net/featured/category/education](http://www.slideshare.net/featured/category/education).
- [63] Perkins, Sid. "A New Twist on Artificial Muscles." *Scientific American*, 11 July 2019, [www.scientificamerican.com/article/a-new-twist-on-artificial-muscles/](http://www.scientificamerican.com/article/a-new-twist-on-artificial-muscles/).
- [64] Damme, Michael Van. "Vrije Universiteit Brussel." *Pneumatic Artificial Muscles (PAMs)*, [mech.vub.ac.be/multibody/topics/pam\\_sub.htm](http://mech.vub.ac.be/multibody/topics/pam_sub.htm).
- [65] Science X. "Soft Robotics: Self-Contained Soft Actuator Three Times Stronger than Natural Muscle, without the Need of Externals." *Phys.org*, Phys.org, 19 Sept. 2017, [phys.org/news/2017-09-soft-robotics-self-contained-actuator-stronger.html](http://phys.org/news/2017-09-soft-robotics-self-contained-actuator-stronger.html).
- [66] Tondu, Bertrand. "Artificial Muscles for Humanoid Robots." *Humanoid Robots, Human-like Machines*, 2007
- [67] "Linear Hydraulic Actuators - Si-Plan Electronics Research." *Si*, [si-plan.com/product/linear-hydraulic-actuators/](http://si-plan.com/product/linear-hydraulic-actuators/).